QUANTITATIVE PREDICTION OF SEGREGATION AT PROCESS SCALE

by

Siying Liu

Bachelor of Science, University of Virginia, 2014

Submitted to the Graduate Faculty of
Swanson School of Engineering in partial fulfillment
of the requirements for the degree of
Doctor of Philosophy

University of Pittsburgh

2018

UNIVERSITY OF PITTSBURGH

SWANSON SCHOOL OF ENGINEERING

This dissertation was presented

by

Siying Liu

It was defended on

November 16, 2018

and approved by

Tagbo Niepa, Ph.D., Assistant Professor,

Department of Chemical and Petroleum Engineering

Sachin Velankar, Ph.D., Professor,

Department of Chemical and Petroleum Engineering

Anne Robertson, Ph.D., Professor,

Department of Mechanical Engineering and Materials Science

Dissertation Director: Joseph J McCarthy, Ph.D., Professor,

Department of Chemical and Petroleum Engineering

QUANTITATIVE PREDICTION OF SEGREGATION AT PROCESS SCALE

Siying Liu, PhD

University of Pittsburgh, 2018

Segregation, or the separation/stratification of particles with differing properties, can lead to significant handling problems, product non-uniformity, and even complete batches being discarded at huge financial loss in multiple industries. Thus, one could argue that segregation is one of the most important factors in industrial processing of granular materials. There has been a tremendous focus in recent years on granular segregation problems and much has been learned about the mechanisms driving those phenomena. Segregation model development holds promise for translation of academic research into industrial practice; however, experimental validation of dynamic models is extremely difficult and typical segregation models are not inherently built with scale-up in mind. One unique aspect of our work is that we overcome these experimental limitations by exploiting a novel framework for segregation testing based on establishing an "equilibrium" between mixing and segregation in free surface granular flows in order to alter the steady-state distribution of particles. By achieving this balance between the rate of segregation and the perturbation rate, we combine the model expressions that we are interested in testing with dramatically simplified experiments to ultimately deduce the segregation rate and validate the expressions. Moreover, by exploring a novel view of the interplay between granular rheology and segregation, we have introduced a new way of structuring segregation rate models that make them inherently more scalable and accurate for industrial use than any models previously reported.

Types of segregation properties studied in this research include density, size, wet and shape. Our results suggest that one can prescribe (or design) industrial operating conditions that will lead to dramatically lower segregation extents.

TABLE OF CONTENTS

LIST OF TABLES

LIST OF FIGURES

1.0 INTRODUCTION

A granular material is an assembly of a large number of discrete solid components. They are ubiquitous in day-to-day life and are second only to water as the world's most handled industrial material [1]. In the chemical industry, more than 30% of products are formed as granular particles [2]. Segregation, or un-mixing, of granular particles is a commonly observed, but usually undesired phenomenon in a variety of industry processes. When particles differ in almost any mechanical property (size, shape, density & angle of repose etc.), segregate can happen; which can manifest as pattern formation, layering or complete separation of the materials[3–6]. This non-homogeneity can cause dramatic revenue loss and product failure in industries such as pharmaceuticals, ceramics, and agriculture, to name but a few. Segregation is unique to solid material and has no direct analogy in fluids. And contrary to fluid mixing, a higher agitation rate may cause more severe segregation rather than better mixing. However, despite been routinely observed, there is little fundamental understanding of the processes/parameters that impact segregation.

Two issues that make the study of segregation daunting are (1) the difficulty in measuring segregation rate in an experimental or industry setting and (2) the lack of validated scale-up capable models. Furthermore, the particle bulk properties e.g., stress, strain, voidage etc. (all of those are necessary in a theoretical description of a granular flow) are extremely difficult to measure. While there have been advances in non-invasive experimental methods[7] which allow measuring valuable information such as particle positions, velocity profiles and particle orientation, those methods are typically expensive and have a big uncertainty involved. In contrast with the mixing of fluids, there is no accepted set of governing equations for solids mixing. This lack of a universal mathematical description is a big hindrance to the understanding of solid mixing/segregation. On the contrary, significant inroads have been made recently in uncovering an understanding of granular rheology with the so-called μ(I) model [8,9]. One goal of this research is to develop unique insight into particle segregation problems and build dramatically more accurate as well as inherently scalable models that are valid for industrial use by exploiting the connection between segregation and flow rheology.

While a global theory of segregation is lacking, the interactions of individual particles are well understood, both experimentally and theoretically. Thus, the discrete element method (DEM) is a popular choice used to study particle segregation. DEM captures the motion of every particle in a large system using the techniques of molecular dynamics simulation and Newton's law of motion. In DEM simulation, particle properties such as size, density and shape can be directly specified, thus make segregation easier to study. Details such as particle velocity, position and concentration profiles for each component in a mixture can be obtained at each time step. Compared with experiments, DEM simulation allows more information to be more easily extracted and the subsequent data tends to be easier to analyze. Therefore, a large part of the work presented in the following chapters is carried out using DEM while validating experiments are performed when possible.

The object of the present work is to examine the segregation phenomena and investigate ways to control it with the main focus on density and size segregation while shape and cohesive segregation are touched. By using intruder-based studies, we developed theories to predict and control segregation rates.

Half of the work focuses on a tumbler and the other half focuses on a shearing cell. Tumblers are hollow devices which are partially filled with granular material and rotated. This class of device is widely used in industry for mixing of materials as well as other applications such as coating and drying. Shearing cells are not typically used in industry but provide one of the cleanest ways to build theory-based models because all of the operational parameters are controllable and their effects are easy to separate. In simulation, a shearing cell is constructed by two periodic plates while in experiments, an annular cell is used to mimic the simulated environment.

The dissertation is organized as follows. Chapter 2 reviews relevant background materials. Previous works in granular mixing, particle rheology and a review of segregating and segregation mechanisms are presented. Finally, a discussion of the simulation methodology, namely the particle dynamics (DEM) technique are included. Chapter 3 covers results of our proposed framework which we show can be used to validate different size/density segregation models. Chapter 4 presents a new rheology-based density segregation model which uncovered a dramatic, never-before-reported regime transition in the rate of density-based segregation that could have a profound impact on the processing of granular materials in industrial practice. Chapter 5 validate the proposed model using experiments. Chapter 6 deals with size segregation and shows our effort to connect rheology with size segregation mechanics. Chapter 7 extends our proposed density segregation model to cohesive particles and shows that cohesive particles also obey the save rheology-segregation relations. Chapter 8 proposes a characteristic size ratio which is able to convert cylindrical particles into spherical particles and thus deal shape segregation using the same manner as size segregation

2.0 BACKGROUND

Granular materials are widely used in industries such as cement, fertilizers, pharmaceuticals, construction, mining and agricultural. These materials are often multi-component and exhibit difference in size, density, shape, and roughness. In fact, even “pure” materials almost invariable exhibit a non-trivial size distribution. As a result, these materials typically segregate, or de-mix during the processing process. Moreover, even previously well-mixed particles will segregation as they are transported from one place to another through methods like chute or conveyor. Segregation is also a nature phenomenon, commonly studied in geological flows or snow avalanche. In the industry material processing phase, many equipment; such as vibrators[10], heaps[11,12], and rotating drums[13,14] can all cause segregation and thus revenue loss.

Granular segregation problems have been a popular topic for a while. The focus includes density-driven [15–17] to size -dependent [18–21] and even multi-model segregation[22–25]. Although much have been learned about the mechanisms driving these phenomena, there has been little to no effort devoted toward scaling those models with respect to flow regime. In this section, we review previous work on segregation modeling and experimentation that is relevant to the proposed work. We begin with a discussion of the modeling of segregation dynamics based on differences in density and size, including a generic framework for how this type of model is often built. A critical point to make in this section is that no previous study has observed a behavior change in segregation rate with changing granular flow rheology. Next, we discuss the computational tool that will be used for a large portion of this work, the Discrete Element Method (DEM).

2.1 SEGREGATION: DENSITY AND SIZE

The vast majority of existing studies of segregation rates have focused on binary combinations of particles that differ in either density or size (or both). In general, these studies take a continuum viewpoint of the flowing granular material and aim to write theoretical expressions that can be solved for either the steady state or dynamic concentration of one of the species in the mixture.

As an example, if we define a certain type particle in a flow as Ψ and its fraction of the total particles as c, the variation of Ψ in a quasi 2D flowing layer is then governed by a convective diffusion equation as:

$$\frac{\partial \Psi}{\partial t}+v_x\frac{\partial \Psi}{\partial x}+v_y\frac{\partial \Psi}{\partial y}=\frac{\partial}{\partial y}\left(D\Psi_{tot}\frac{\partial c}{\partial y}-J_s\right) \tag{2-1}$$

where the diffusion and segregation are neglected in the flow direction x. The first term on the right-hand side is the diffusion flux with D being the diffusion coefficient, while J_s represents the segregation flux. This approach allows us to choose the segregation flux model and after coupling with existing theories, we can solve for a concentration profile of particles across the flowing layer. In the following paragraphs, we discuss existing models of segregation velocity V_s which is commonly used to calculate segregation flux as $J_s=V_s\Psi_{tol}c$.

2.1.1 Density-driven Segregation

Density segregation is often thought to arise due to an effective “buoyant force” experienced by the particles [16,17]. In the buoyance approach, particles maybe considered as immersed in a medium of surrounding particles; thus, heavier particles “sink” down while lighter particles “float” up. An early model proposed the segregation velocity took the form

$$Vs = -K(\rho_1 - < \rho >) = -K_s(1 - \overline{\rho}) \tag{2-2}$$

where $<\rho>$ is the averaged particle density, ρ_1 is the density of the light particles, $\overline{\rho}$ is the density ratio between light and heavy particles and K are constants

2.1.2 Size-driven Segregation

In contrast to the density segregation, which has a commonly accepted theory, size segregation has adapted a more diverse range of approaches with many depending on the flow “regime” – i.e., dense verses dilute. One common approach for dilute flow adopt the kinetic theory-based approach [26]. They suggested that size segregation is due to granular thermal diffusion. However, recent work by Fan and Hill [27] showed that kinetic theory based on binary collisions predicted the opposite segregation direction from experimentally observed trends in dense phase flow.

In works mainly focus on dense phase, several papers have proposed models using percolation argument [18,28,29]. In short, percolation (Figure 2.1) can be explained by the fact that small particles consistently have a higher chance to drop in a void than bigger particles. Thus, small particles move downward by dropping into the voids, and consequently, the large particles travel upwards. While the details of size segregation models differ, a typical model can be written as [30]

$$Vs = [K_i + (1 - c)K_c](1 - c)(1 - \overline{d}) \tag{2-3}$$

Where K are concentration-dependent components that can be complex functions depends on parameters such as granular temperature, local void fraction, coefficient of restitution etc. To make model fitting easier, Ks are usually considered as a constant. c is particle ratio as mentioned before and $\overline{d}$ is the particle size ratio.

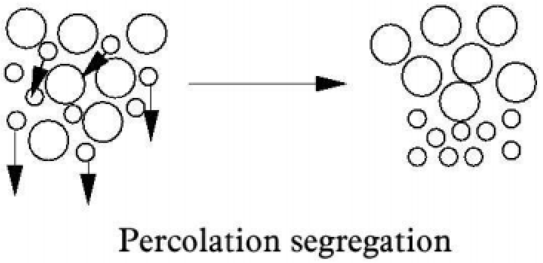

Figure 2.1: Size segregation mechanism: percolation

2.2 GRANULAR SYSTEM RHOLOGY

When particles are large enough (d > 250 μm), particles interactions are dominated by contacting with neighbors while molecular level forces can be neglected. Still, dry granular material flows are not easy to describe. Granular materials can behave like a solid (in a sand pile), a liquid (poured from a silo) or a gas (when strongly agitated) depending on the flow velocity[31]. It is a common practice to divide the flow into three regimes[8]. First, a quasi-static regime where particles have long duration contacts with their neighbors and can be described using soil plasticity models. Secondly, a gaseous regime where particles are far apart one from another and can be considered as in analogy to kinetic theory of gases. In between those two regimes is the dense flow regime which up to recently no constitutive equations or framework can describe. MiDi [8] is the first using a single dimensionless number I to describe granular system rheology. The inertia number I describes the relative importance of inertia and confining stresses and is defined as

$$I = \frac{\gamma d}{\sqrt{P / \rho}} \tag{2-4}$$

The inertia number can also be interpreted in terms of the relevant time scales controlling particle motion as shown in **Error! Reference source not found.**. Considering the motion of one particle during a simple shear, the particle first follows the medium deformation and the mean time it needs to move from one stable position to the next is $t_s = \gamma^{-1}$. During the movement, the particle eventually reaches an unstable position when passing though the crest over particles just below. Due to the confining pressure acts upon the particle, it is pushed down in the crest. The time of falling (t_f) of a particle with density ρ and dimeter d can be estimated by free falling equation as $t_f = d / \sqrt{P / \rho}$. The inertia number I is the ratio between t_f and t_s. In the quasi-static regime, I is seen as $\rightarrow 0$ and in the kinetic regime, I is on the other extreme. The dense regime lays in the range of I in between.

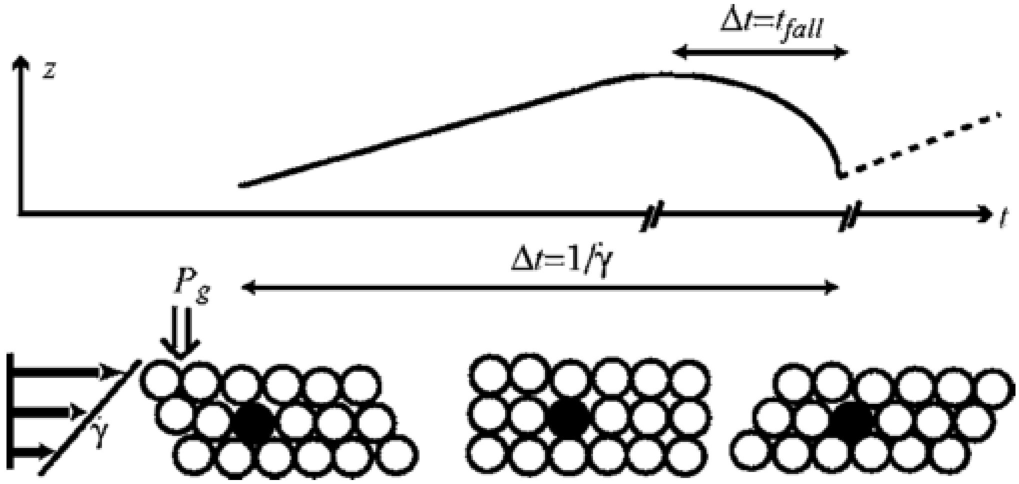

Figure 2.2: Sketch of the motion of a particle during a simple shear under a confining pressure[32]

Inertia number can be used to provide a relevant framework to describe dense granular flows. In Figure 2.3. (a) shows the ratio of shear stress over normal stress as a function of I, (b) shows the volume fraction as a function of I and (c) shows the shape of friction law used in rheology theory as a function of I. Those relations between inertia number and granular rheology provide a constitutive law that could be useful to describe and character complex granulation configurations.

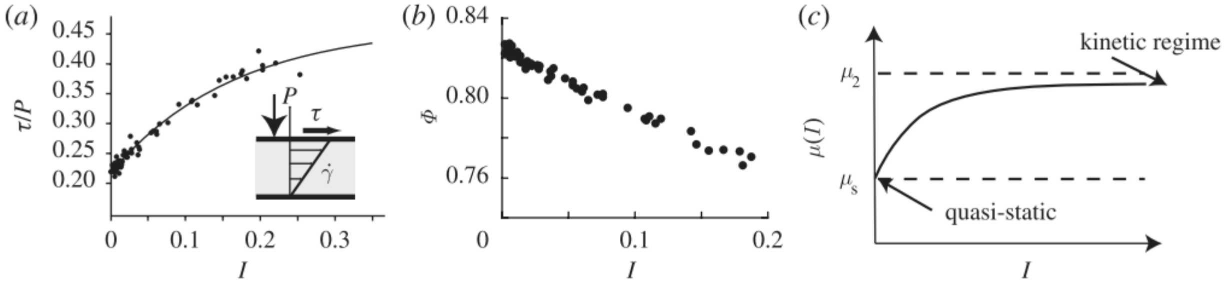

Figure 2.3: Inertia number relations with granular flow rheology[33]

2.3 SIMULATIONS

The computational tool that will be used for this work is the Particle Dynamics Method. In this technique, the bulk flow of the material is captured via simultaneous integration of the interaction forces between individual pairs of particles [34,35]. While these forces typically include only contact forces and gravity, additional particle interaction force (such as surface adhesion[36] and liquid-bridge[37]) can be easily added [38]. In this section, we review some technical particle-level theory of this method.

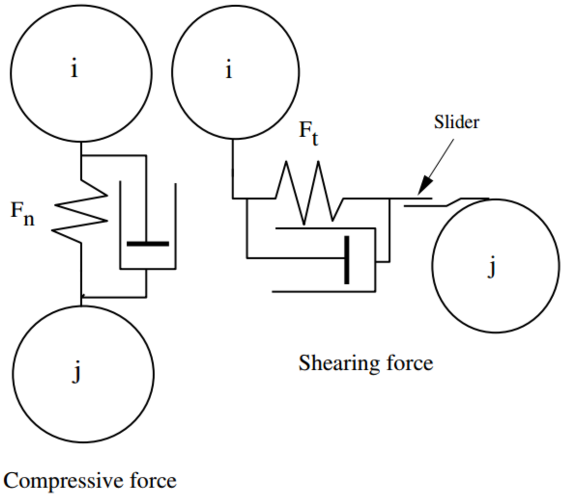

Figure 2.4: Schematic of a simple DEM force model

2.3.1 Equations of Motion

In DEM simulation, bulk flow of the granular materials is captured via simultaneous integration of the interaction collision forces. Newton's equations of motion (Eq. (2-5) & (2-6)) are used to calculate each particle's trajectory.

Linear Motion:

$$m\frac{dv}{dt} = -mg + F_n + F_t \tag{2-5}$$

Angular Motion:

$$I\frac{dw}{dt} = \vec{F}_t \times \vec{R} \tag{2-6}$$

where m, v, t, I, w, R, F_t and F_n are the particle mass, velocity, time step, moment of inertia, angular velocity, particle radius, normal force and tangential force acting on a particle.

2.3.2 Force Models

The force models are integral to DEM simulation. Forces acted upon particles include external forces (gravity, compress pressure) and contact forces – normal repulsion and tangential friction. Figure 2.4 shows a simple force model accounting for the contact mechanics which includes a spring, a dashpot and a slider configuration [34].

2.3.2.1 Normal Forces

The normal force is modeled as an elastic-plastic material after the work of Thornton [39]. The deformation of the particles α is computed as the "overlap" so that $\alpha = v_n dt$, where v_n is the velocity on the normal direction and dt is the time-step. The value of α is positive during loading and negative during unloading. At the initial stages of the loading, the normal force, F_n is purely elastic and is given by

$$F_n{}^N = F_n{}^{N-1} + k_n \alpha \tag{2-7}$$

where k_n, which equals to 2aE*, is the normal force constant based on the Hertz theory. E* is the representative Young's Modulus and a is the radius of the contact area. In Eq.(2-7), N and N-1 are current and previous time-step respectively.

Once the normal force exceeds a yield force, F_y, a modified version of the contact force-displacement relationship based on Wu[40] is used. The normal force constant k_n of further loading is given by $\pi Y R^*$ where Y is the yield stress and R* is the effective particle radius and the deformation of the particle α equals to $\pi^2 Y^2 R / 4E^{*2}$.

If cohesive force is taken into consider, once particles are contacted, both the capillary force F_c and the viscosity force on the normal direction F_{vn} are calculated using equations below:

$$F_c = -\pi\gamma R * (exp(AS + B) + C) \quad (2\text{-}8)$$

$$F_{vn} = -6\pi R\mu v_n R/S \quad (2\text{-}9)$$

In the equations, S is the separation distance between the pair of particles, A, B and C are constants depend on the liquid bridge's volume. μ is the interstitial fluid's viscosity, R is the particle radius and v_n is the relative normal velocity of the pair of spheres.

2.3.2.2 Tangential Forces

We used tangential forces derived by Walton and Braun[41]. For each time-step, the new tangential force acting at the particle-particle contact point, F_t is given as:

$$F_t{}^N = F_t{}^{N-1} - k_t \Delta s \quad (2\text{-}10)$$

where F_t^{N-1} is the old tangential force and $k_t\Delta s$ is the incremental change in the tangential force during the present time-step due to relative particle motion[42]. When F_t is smaller than friction force caused by F_n, based on Thornton[43], the frictional stiffness k_t will equal to 8G*a, where G* is the shear modulus and a is the radius of the contact area.

In case of cohesive, a viscosity force (F_{vt}) on the tangential direction is added as seen in Eq.(2-11).

$$F_{vt} = -(\frac{8}{15} ln \frac{R}{S} + 0.9588) 6\pi R\mu v_t \quad (2\text{-}11)$$

All the notations are same as in the normal force section except v_t which is the relative tangential velocity of the pair of spheres

3.0 VALIDATING SEGREGATION RATE MODELS

The content of this chapter is taken from Liu, S. and McCarthy, J. J. (2017), Validating granular segregation rate models. AIChE J., 63: 3756-3763. doi:10.1002/aic.15770

3.1 INTRODUCTION

It is well known that when processing two different types of particles in a solid handling device, segregation often arises due to differences in particle properties [44] and that, in practice, even an ostensibly “pure" material may segregate because of non-trivial size distribution [30]. In a horizontal drum - a proptype mixing device - the segregation based on density differences will force the less dense particles to the periphery and the denser particles to the inner core, while the segregation based on size differences will (typically) move larger particles to the periphery and smaller particles to in inner core [45] (although the opposite trend can be obtained under certain conditions [46]). In some industries, segregation phenomena can create problems in maintaining uniform product quality and ultimately cause revenue loss.

A partially filled rotating tumbler is one common way of mixing particles. In a tumbler, the major component of the velocity is parallel to the surface and there is a boundary between the continuous flow regime (liquid-like flowing particles) and the fixed bed regimes (solid like) [47]. Makse [48] stated that it is plausible to describe a rotating tumbler system by only its surface properties, thus, only the properties of the particles that compose the flowing layer particles are studied in this paper. In the flow regime examined in this work, percolation is often the dominant mechanism of free surface segregation such that the larger (lighter) particles rise to the top while the smaller (denser) particles sink to the bottom[49]. In a rotating tumbler, the reversible process between mixing and segregation eventually balances and the particle distribution becomes invariant with time (i.e., the system reaches a statistical steady state). Shi et al. [50] have shown that by periodically and ultimately reduces the extent of segregation. They suggested that, by reducing the extent of segregation, the ultimate balance between mixing and segregation (at steady state) is altered. When the flow is perturbed at a high frequency (above a critical value of the forcing frequency), segregation can be effectively eliminated. The relation between flow perturbation rate and extent of segregation is reconfirmed in this work, while at the same time we exploit this changing balance between mixing and segregation as a means of testing segregation models.

Although the mechanisms of segregation in shear flow are well understood and several continuum rate models hold promise for scale-up, accurate experimental validation of dynamic models remains extremely difficult. In this work, focusing on binary systems, we aim to use a framework established from previous work in our group [30,51,52] - and alluded to in the previous paragraph - as a means to validate different rate models. We focus exclusively on the rolling regime of a tumbler. Several different size and density models will be used to predict the critical value of the forcing frequency (and its dependence on material and process parameters). Then relationship between the extent of segregation and the rate of perturbation will be studied at steady state both simulative and experimentally for a variety of conditions. By controlling the periodic flow perturbations rate (tumbler rotation rate), particles sizes and density ratios we can evaluate how well competing models predict the critical value of the forcing frequency.

3.2 THEORY

3.2.1 Framework

The central idea of the segregation testing framework set forth here is that, while perturbing a flow at a rate significantly higher/lower than the critical forcing frequency will lead to almost complete mixing/segregation, choosing a perturbation frequency that is close to the critical value will lead to a ``unique'' steady state degree of mixedness. Thus, one can measure the resulting steady-state distribution of particles in order to evaluate the accuracy of a segregation models' prediction of the critical frequency (and how it varies with material and process parameters). In essence, this idea makes an analogy between the competition between the mixing and segregation behavior with the competition between a forward and backward reaction. That is, if one were to measure (or calculate) two of the three reaction components -- forward reaction rate, backward rate, equilibrium distribution -- the third would be determined. Here, we use the “equilibrium” segregation extent coupled with the known forcing frequency to assess the (third component) a segregation rate model. Specifically, we use an axially-located baffle to perturb the surface flow within a tumbler-type mixer at a predetermined frequency f (that is directly related to the tumbler rotation rate as discussed below).

In order to identify the critical perturbation frequency[52] one needs to recognize that segregation takes a finite time, t_s , for segregation to occur. As discussed previously [51] a reasonable choice of the characteristic segregation time may then be written as $t_s = \frac{d}{v_s}$, where d is the particle diameter and v_s is the segregation velocity taken from the segregation model to be tested. Following this procedure, the critical frequency can be expressed as

$$f_{crit} = \frac{1}{t_s} = \frac{v_s}{d} \tag{3-1}$$

When using an axially-baffled tumbler as our means of flow perturbation we note that the flowing layer is interrupted and the segregation orientation changes once per half revolution. If we set the effective forcing frequency as the inverse of the mean residence time in the layer t_l [53], we obtain the effective forcing frequency within the tumbler as

$$f = \frac{1}{t_l} = \frac{\sqrt{\omega\gamma}}{2\pi} \tag{3-2}$$

where ω is the rotation rate (rad/s) and γ is the shear rate in the flowing layer. The shear rate in a tumbler mixer has been reported by Ottino et al.[53] as

$$\gamma = M * [\frac{g * sin(\theta - \theta_s)}{d * cos(\theta_s)}]^{0.5} \tag{3-3}$$

where M is a constant, θ is the dynamic angle of repose and θ_s is the static angle of repose. Chou et al.[54] fitted experimental results with Eq.(3-3) and concluded that a constant value M=1.36, and we use this value throughout the paper.

It should be noted that, in Eq.(3-3), the estimated effective forcing frequency is derived from the non-baffled tumbler case; thus, the value of f is a lower bound of the real value since the flowing layer should be effectively truncated by the baffle, hence the material will visit the flowing layer more frequently in the baffled case. Combining Eq.(3-2) and Eq.(3-2), we obtain a ratio between the effective forcing frequency and the critical forcing frequency as shown below

$$\frac{f}{f_{crit}} = \frac{d\sqrt{\omega\gamma}}{2\pi v_s} \tag{3-4}$$

The mode of employment of Eq. (3-4) is as follows. We expect that the segregation extent of the system will decrease monotonically as the perturbation frequency, f, increases from small values. At some point, as $\frac{f}{f_{crit}}$ reaches/exceeds unity, we expect that the mixing/segregation balance will have shifted enough that we may expect a well-mixed system. Eq. (3-4) can be made analytic with respect to material properties and process parameters by incorporating a theoretical model for the segregation velocity v_s. Thus, all models to be tested within our framework will dictate this form in each case examined.

3.2.2 Density Segregation

3.2.2.1 Buoyant Model

Consider equal-sized particles of different densities in the flowing layer of a tumbler. The simultaneous rising and sinking of lower density and higher density particles, respectively, causes segregation. Vargas et al.[52] proposed a density model based on the assumption that the driving force for segregation is a particle buoyant force[6]. Assuming the segregation velocity is proportional to the buoyant force, the segregation velocity of the heavy particle will take the form:

$$v_s = K_s(1 - \bar{\rho}) \tag{3-5}$$

where $\bar{\rho}$ is the density ratio between light and heavy particles, and K_s is the characteristic segregation velocity depending on the local void fraction and granular temperature[52]. According to previous work[16] the dimensionless Peclet number Pe can be defined as $\frac{v_{segregation}}{v_{diffusion}}$ and is approximately equal to 1 for the material and process parameter space examined here. Thus, $\frac{K_s R}{D} \approx 1$. According to Savage[55], the diffusivity in a sheared layer D can be written as

$$D \propto d^2\gamma. \tag{3-6}$$

Incorporating the buoyant density segregation model described here into the segregation framework Eq.(3-4) leads to:

$$\frac{f}{f_{crit}} = \zeta_d \sqrt{\frac{\omega}{\gamma}} * \frac{1}{(1-\bar{\rho})} \tag{3-7}$$

where, due to current theoretical uncertainty, ζ_d is treated as a fitting parameter, but is expected to be of order 1.

3.2.2.2 Drag Model

The drag force on a segregating particle may be expected to impact the segregation rate, however this is not accounted for within the simple buoyant model outlined above. To account for this, Tripathi et al.[17] presented a density segregation model which includes the drag force. They started with a force balance on a particle as

$$0 = F\_w - F\_b + F\_d \tag{3-8}$$

where F_d is the drag force through the bed, F_w is the gravitational component in the segregation direction and F_b is the buoyancy force exerted on the particle by the granular medium (toward the surface or away from the segregation direction). The drag force F_d on the particle of diameter d is given by a modified Stokes law, $F_d = B\pi\eta d v_s$ where v_s is the sinking/segregation velocity, η is the viscosity caused by the surrounding granular medium and B is treated as a fitting parameter. To mimic the simplest case of density segregation, the behavior of a heavy particle in a medium of light particles (m_L) is analyzed[17] ; to sum everything up, the above equation can be rewritten as

$$v_s = -\frac{m_H g \cos\theta - m_L g \cos\theta}{B\pi\eta d} \tag{3-9}$$

Combining Eq. (3-9) with Eq. (3-4)and simplifying the combined equation yields

$$\frac{f}{f_{crit}} = \frac{3B}{2\pi g d}\frac{\eta\sqrt{\omega\gamma}}{\rho_H(1-\bar{\rho})\cos\theta} \tag{3-10}$$

The viscosity term η can be further defined as $\eta = \frac{\tau}{\gamma}$, where τ is the shear stress which Tripathi et al.[56] suggests may be written as:

$$\tau = P * tan(\theta) = \rho_{avg} d g \cos(\theta) \tan(\theta) \tag{3-11}$$

In Eq.(3-11), P is the pressure within the surface flow (and is calculated based on equations from Chou et al [54] and ρ_{avg} is the average density of the whole system. Combining these equations yields

$$\frac{f}{f_{crit}} = \frac{3B(1+\bar{\rho})}{4\pi(1-\bar{\rho})}\sqrt{\frac{\omega}{\gamma}} * tan(\theta) \tag{3-12}$$

3.2.3 Size Segregation

3.2.3.1 Linear Model

In the rolling regime of a tumbler mixer (dense flow), it is a well-known phenomenon that, under gravity, small particles sink through shear-generated voids while large particles rise to the top. Below is phenomenological size segregation model proposed by Hajra et al.[30]. In this model, the segregation velocity is assumed to be proportional to the particle size ratio and the average particle diameter.

$$v_s = -K(d_1 - \langle d \rangle) \tag{3-13}$$

In this expression, $\langle d \rangle = \dfrac{d_1\phi_1 + d_2\phi_2}{\phi_1 + \phi_2}$ is the mass-averaged particle size, d is the diameter of the particles and ϕ is the mass concentration of particles. For an equal-mass binary system, ϕ is equal to 0.5. Subscript 1 refers to variables for the smaller particle, while 2 refers to larger particles. K has been assumed to be a constant which has both an intrinsic and a concentration-dependent component (K_T and K_S respectively)[30]. Expanding $\langle d \rangle$ and simplifying Eq.(3-13) yields

$$v_s = K_\phi(d_1 - \bar{d}) \tag{3-14}$$

where K_ϕ is a constant at fixed total concentration and the size ratio $\bar{d} = d_1 / d_2$. Using the model outlined above, the characteristic segregation time can be written as

$$t_s = \frac{d_1}{K_\phi(1-\bar{d})} \tag{3-15}$$

where d_1 is the radius of the small particles. Defining the diffusion time t_D as d_1^2 / D , we again take the Peclet number to approximately equal to 1[30] so that $Pe = d_1 K_\phi / D \approx 1$. Combining the above equation with the diffusivity Equation (Eq.(3-6)), t_s can be written as $t_s \propto \frac{1}{\gamma(1-\bar{d})}$. Thus, we can rewrite Eq.(3-4) for the size segregation as

$$\frac{f}{f_{crit}} = \zeta_s \sqrt{\frac{\omega}{\gamma}} \frac{1}{(1-\bar{d})} \tag{3-16}$$

where ζ_s is treated as a fitting parameter.

3.2.3.2 Natural Log Model

Schlick et al. [21]derived a new size segregation model based on DEM simulation of a quasi-2D bounded heap flow. Similar to the linear model, this model also states that the segregation velocity is approximated as a linear function of the shear rate and the concentration of the other particles as:

$$v_s = -S\gamma(1-\phi_1) \tag{3-17}$$

Here S is the segregation length scale depending on the particle size and particle size ratio and ϕ_l is the mass fraction of large particles. A simulation correlation for S was suggested[21] as

$$S(d_1, d_2) = 0.26 d_1 log(\frac{d_2}{d_1}) \tag{3-18}$$

After combining Eq.(3-17) with Eq.(3-4) and rearranging, we obtain

$$\frac{f}{f_{crit}} = \frac{1}{4\pi * 0.26 * (1-\phi_1)} \sqrt{\frac{\omega}{\gamma}} \frac{1}{(log(1/\bar{d}))} \tag{3-19}$$

We should note that, in order to avoid spontaneous percolation of fines through the bed we have limited our size ratios to values that are reasonably close to unity. Thus, the functional form of Eq.(3-16) and Eq.(3-19) are largely the same to first order.

3.3 MEASUREMENT

3.3.1 Experiment

All models suggest that both the particle material property ratios ($\bar{\rho}$ or $\bar{d}$)and the rotation rate (ω) of the tumbler can impact the steady-state segregation of a single-baffled tumbler. Thus, to test our theory, the particle properties and rotation rate of the tumbler were controlled, and the extent of segregation at steady state was analyzed. The experiments were carried out in a half-filled glass tumbler of diameter 15 cm and length 1.5 cm. The tumbler has an axially-located baffle.

For the density portion, the experiments were conducted using 1:1 volume ratio combination of two types of 3 mm beads picked from cellulose acetate (1240 kg/m^3), steel (7900 kg/m^3)or glass (2500 kg/m^3). Later, the glass used in this experiment was etched using 5 wt% HF acid to increase the surface roughness and mixed with steel again for an extra set of experiment. Three density ratios $\bar{d} =$ 0.15, 0.31 and 0.5 were tested.

For the size portion, cellulose acetate balls of 4 different sizes with diameters 2, 3, 4 and 5 mm were used. Each size of ball has a different color. Four size ratios $\overline{d} =$ 0.4, 0.5, 0.66 and 0.75 were tested.

For all experiments, the tumbler was rotated around the horizontal axis with a chosen constant rotation rate (ω = 3-18 RPM.) using a computer-controlled stepper motor. In the flowing layer, the local surface angle and the local layer thickness are known for varying with the local flow properties[57]. Thus, the particle static angle of repose θ_s and dynamic angle of repose θ were measured using at the center of corresponding non-baffled tumbler case. The dynamic angle of repose θ was measured when the system reached steady state and the static angle of repose θ_s was measured when the non-baffled tumbler stopped rotating.

Images of the rotating tumbler were taken with a Nikon D200 digital camera once the segregation patterns became time invariant (after more than 5 rotations). A halogen light is used to increase brightness while taking pictures. For the size experiment, different particles were distinguished by their colors. For the density experiments, the reflective spots' position of each particle and the spots' intensity were used to distinguish different types of particles. Figure 3.1 shows the experimental results of steel/glass (dyed as red) particles system at steady state. The steady states of pictures were analyzed using a software called ImageJ. The picture analysis procedure followed the procedure described by Vargas et al \cite{Vargas:2008la}. The intensity of segregation (Eq.(3-20)) was used in order to quantitatively determine the degree of mixing. In Eq.(3-20)), $< c >$ is the average concentration of the whole system and C_i is the local concentration after separating the whole system into N uniformly distributed boxes. For equal total volume binary system, the IS ranges from 0 to 0.5. A low value of IS indicates a well-mixed system. Four pictures were analyzed and their average IS value was used at each condition.

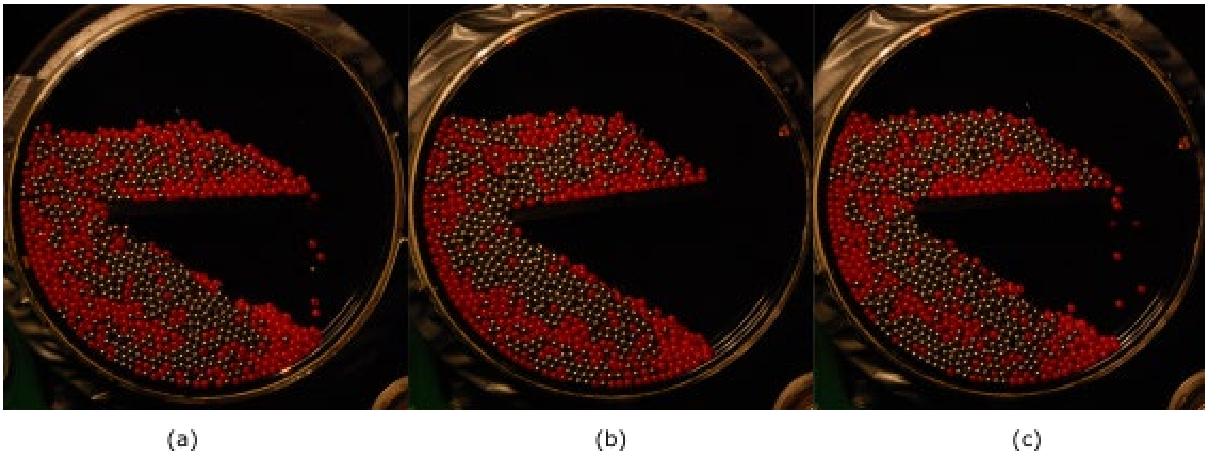

Figure 3.1: Density ratio $\bar{\rho} =$ 0.31 experiment results at different rotation speeds (a) 6 RPM (b) 9 RPM (c) 12 RPM

$$IS = \left[\frac{1}{N-1}\sum_{i=1}^{N}(C_i - \langle C \rangle)^2\right]^{1/2} \tag{3-20}$$

3.3.2 Simulation

For each experimental condition, the corresponding simulation was done using the discrete element method (DEM)[58]. Figure 3.2 shows three DEM simulation trials for steel/glass system ($\bar{\rho} =$ 0.31). For each curve, the average IS of the flat portion (shown as the dot lines) of the curve were used as the steady state IS value, which was later fitted into segregation models.

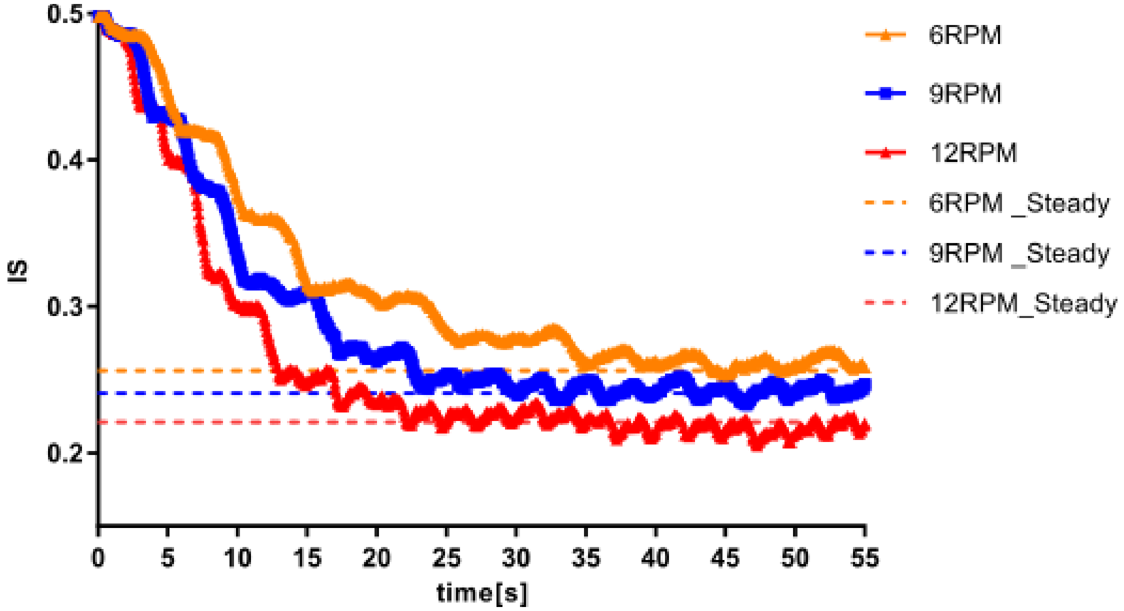

Figure 3.2: Density ratio $\bar{\rho} =$ 0.31 IS vs. time for three rotation rates

In the DEM method, the bulk flow of the material is captured via simultaneous integration of the interaction forces between individual pairs of particles[34,35]. In this section, we review the details of the model employed in this paper. A thorough description of both the normal interaction laws and the tangential models can be found elsewhere.

3.3.2.1 Normal Forces

The normal force is modeled as an elastic-plastic material after the work of Thornton[59,60]. The deformation of the particles α is mimicked via a computational "overlap" so that $\alpha = v_n dt$, where v_n is the velocity on the normal direction and dt is the time-step. In the above equation, α is positive for loading and negative for unloading. At the initial stages of loading, the normal force, F_n, is purely elastic and is given by

$$F_n^N = F_n^{N-1} + k_n * \alpha \tag{3-21}$$

where k_n , which equals to $2aE^*$, is the normal force constant from the Hertz theory[61]. In the above equation, a is the radius of the contact area and E^* is the representative Young's Modulus. In Eq.(3-21), F_n^{N-1} is the old normal force and F_n^N is the normal force at the current time-step.

Once the normal force exceeds a yield fore, F_y, a modified version of the contact force-displacement relationship based on Wu[40] is used. The normal force constant k_n of further loading is given by πYR^* and the deformation of the particles α equals to $\frac{\pi^2 Y^2 R}{4E^{*2}}$, where Y is the yield stress and R^* is the effective particle radius.

3.3.2.2 Tangential Forces

Walton and Braun derived the tangential (frictional) force[41]. For each time-step, the new tangential force acting at a particle-particle contact, F_t, is given as:

$$F_t^N = F_t^{N-1} - k_t \Delta s \tag{3-22}$$

where F_t^{N-1} is the old tangential force and $k_t \Delta s$ is the incremental change in the tangential force during the present time-step due to relative particle motion; i.e., Δs is the displacement during the present time-step; its expression is adapted from a vector form given by Walton[42]. When F_t is smaller than $\mu_f F_n$ where μ is the coefficient of sliding friction, based on Thornton[43] the frictional stiffness k_t equals to $8G^* a$, where G^* is the shear modulus and a is the radius of the contact area.

Although the simulated particle sizes and densities were matched to their corresponding experiments, there are still two differences between simulation and experimental conditions worth mentioning. First, the experiment used a quasi-2D tumbler but the simulation used periodic boundary conditions. The existence of the glass walls in the experiments caused some inconsistencies between experiment and simulation results. Second, pictures taken from the experiments only contain 2-D information while 3-D information were obtained from simulation. Thus, for simulations, much more data is available and the standard deviation of IS is therefore significantly smaller in simulated trials.

3.4 RESULTS

In this section we examine segregation results of experiments and simulations in a half-filed baffled tumbler, for both density and size binary system. Different models are fitted in the framework and compared with each other. A quantitative value is needed to distinguish between the subtleties of different models. Since our theoretical framework predicts that when the f / f_{crit} increases, the IS value will initially decrease and eventually reach a steady state, an ideal fit will be a monotonic decreasing function. Thus, Spearman's correlation $|r_s|$ was used to quantitatively determine which theory fits the framework better. The closer a model's $|r_s|$ value is to 1, the better the fitting is; and therefore, the more accurately we expect the model to capture segregation dynamics as a function of materials and process parameters.

3.4.1 Density Segregation

Three density ratios ($\overline{\rho} =$ 0.15, 0.5 & 0.31) were tested in a rotating tumbler at controlled rotating rate. For $\overline{\rho} = 0.31$, experiments have two sets of data. One set of data presents smooth glass beads vs. steel and another set presents HF treated rough glass beads vs. steel. The effect of rough surface is hard to mimic in simulation so only one set of $\overline{\rho} = 0.31$ data is presented for density simulation. Figure 3.3 shows the plot of IS as a function of $f \,/\, fcrit$ for the buoyant density model while Figure 3.4 shows the fitting for drag model. By comparing Figure 3.3 with Figure 3.4,it can be seen that the HF treated $\overline{\rho} = 0.31$ date set does not fit very well with other sets of data for buoyant model while it has a reasonable fit for drag model. This is expected since by changing the surface roughness of the beads, we changed the drag force, which is considered a variable in the drag model but not buoyant model. Moreover, the drag model overall has a higher $|r_s|$ value for both simulation and experiment. Thus, we can conclude that the variance of drag force has a noticeable impact on the segregation velocity of same size but different density particles.

Both models show the trend that while f / f_{crit} increases, the IS value decreases as expected. In other words, the system is mixed better when the flowing layer is perturbed more frequently. The experiments and simulations both show that higher density ratio $\overline{\rho}$ corresponding to lower IS value (better mixing) at same rotating rate. This is because the similar the properties of tested particles are, the better the system is able to mix. And if two sets of particles have identical mechanical properties (same density in our case), no segregation will occur since the system is mono-dispersed.

The fitting parameter ζ_d in Eq. (3-7)is set equal to 3 and the fitting parameter c in Eq. (3-10) is set to equal to 7.5 to make sure the IS value tends to flatten when the f / f_{crit} value reaches unity for both models. The analyzed IS values show a reasonable degree of agreement between simulations (3-D flow) and experiments (2-D flow) which means our simulation does a good job to mimic the real phenomenon. However, it should be noted that although the simulated particle sizes and densities were matched to their corresponding experiments, there are still two differences between simulation and experimental conditions. First, the experiment used a quasi-2D tumbler but the simulation used periodic boundary conditions. The existence of the glass walls in the experiments caused some inconsistencies between experiment and simulation results. Since the wall friction tends to prevent mixing, the IS value of experiments is slightly higher than the simulation. Also, based on the lower $|r_s|$ value, the fitting for the experiments is worse. Orpe et al.[57] mentioned that the effect of wall friction influence the dynamic surface angle. In agreement with their statement, our simulation results, which don't include wall friction, have smaller angles (dynamic & static) than the experiment results. For the drag model, since viscosity η is proportional to the dynamic angle, the f / f_{crit} value of the simulation is always smaller than the corresponding sets of experiments' values. Buoyant model is not sensitive to the angle differences so both experiment and simulation have same f / f_{crit} scales. Another difference between the experiments and simulation conditions is that pictures taken from the experiments only contain 2-D information while 3-D information were obtained from simulation. Thus, for simulations, much more data is available and the error bars of IS is therefore significantly smaller in Figure 3.3 and Figure 3.4.

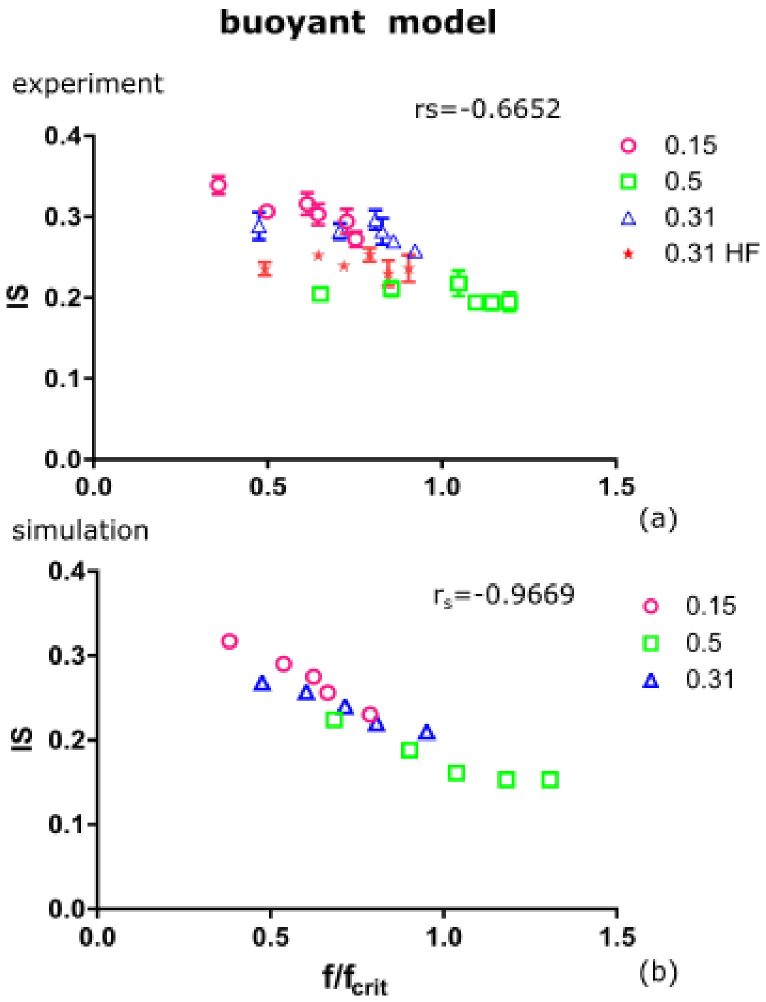

Figure 3.3:Fitted density buoyancy model. Experimental (a) and simulation (b) fitting of density segregating in a tumbler mixer while varying both density ratios $\bar{\rho}$ and rotation rate ω . Different colors denote different density ratios. ``HF" denotes trials where glass beads were roughened via etching.

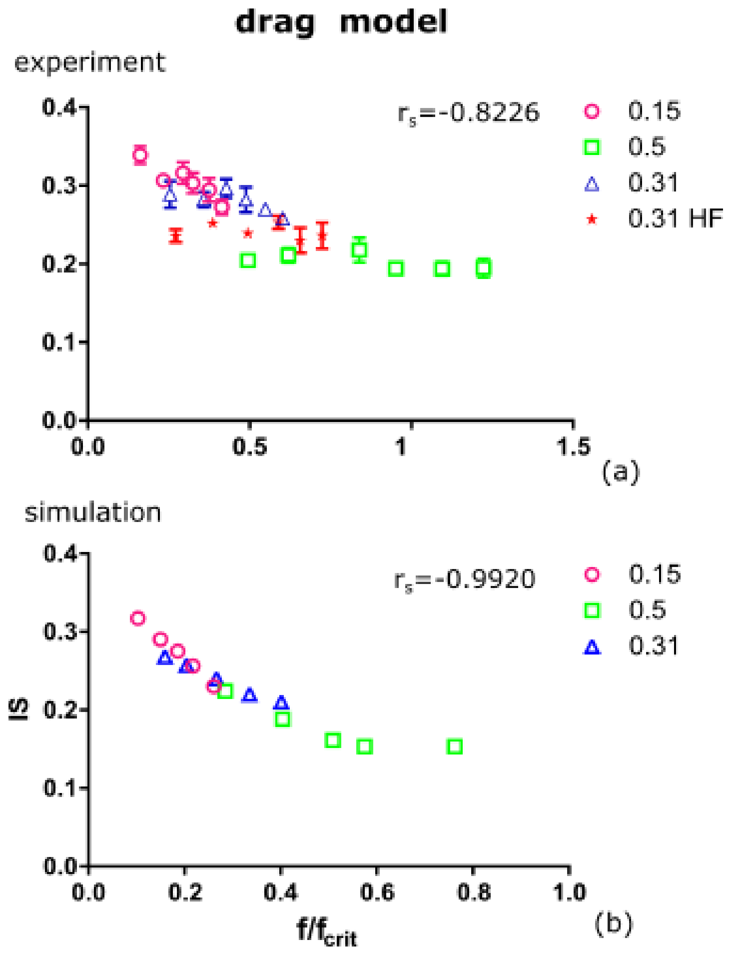

Figure 3.4: Fitted density drag model. Experimental (a) and simulation (b) fitting of density segregating in a tumbler mixer while varying both density ratios and rotation rate. Different colors denote different density ratios. ``HF" denotes trials where glass beads were roughened via etching.

3.4.2 Size Segregation

Four sets of experiments with varying particle size ratio were conducted. One set of experiments used acetate beads of 4 mm along with 2 mm ($\bar{d} = 0.5$). The second set of experiments used beads of 4 mm along with 3 mm ($\bar{d}$ =0.75). The third set of experiments is with beads of 3 mm along with beads of 2 mm ($\bar{d}$ =0.67). The last set of experiments used beads of *5mm* along with beads of 2mm ($\bar{d}$ =0.4). The fitting parameter ζ_s in Eq. (3-17)is set to equal to 1.

Figure 3.5 presents the IS versus the f / f_{crit} value for linear model where the value of f_{crit} is assumed to be linear related to the size ratio; while Figure 3.6 shows results for log model where f_{crit} is calculated as a log function of the size ratio. Same as observed in the density segregation, the IS value decreases while the f / f_{crit} increasing and larger size ratio sets have lower IS value because of similar particle properties. For both experiment models, when the f / f_{crit} value is larger than 1, the IS reaches a steady value around 0.2. For simulation models, while it is less obvious, the IS value is reaching a steady value when f / f_{crit} is larger than 1. Same as the density results, this agrees with our theory which states that when the value of f / f_{crit} is around or larger than 1, the baffle is perturbing the surface flow in the tumbler at a speed faster than the time t_s required for particles to segregate; thus, the system is seen as well-mixed so the IS value ceases to decrease even though the f / f_{crit} continuous to increase. Same as the density result, the experiments IS value is higher than simulation result, however, it is more obvious for size results because wall friction has more significant influence on lighter and smaller particles used in size experiment.

Although the log model fits slightly better (insignificantly higher $|r_s|$ value), those two models basically show the same trend. This is because within the size range we tested (0.4-0.75), the log function has a similar shape comparing with the linear function. In order to show the difference between those two functions more dramatically, a wider size range needs to be used. However, when the size ratio is too small, segregation will happen spontaneously and become independent of the rotation rate, and when the size ratio is too large, segregation will not be significant enough to be measured.

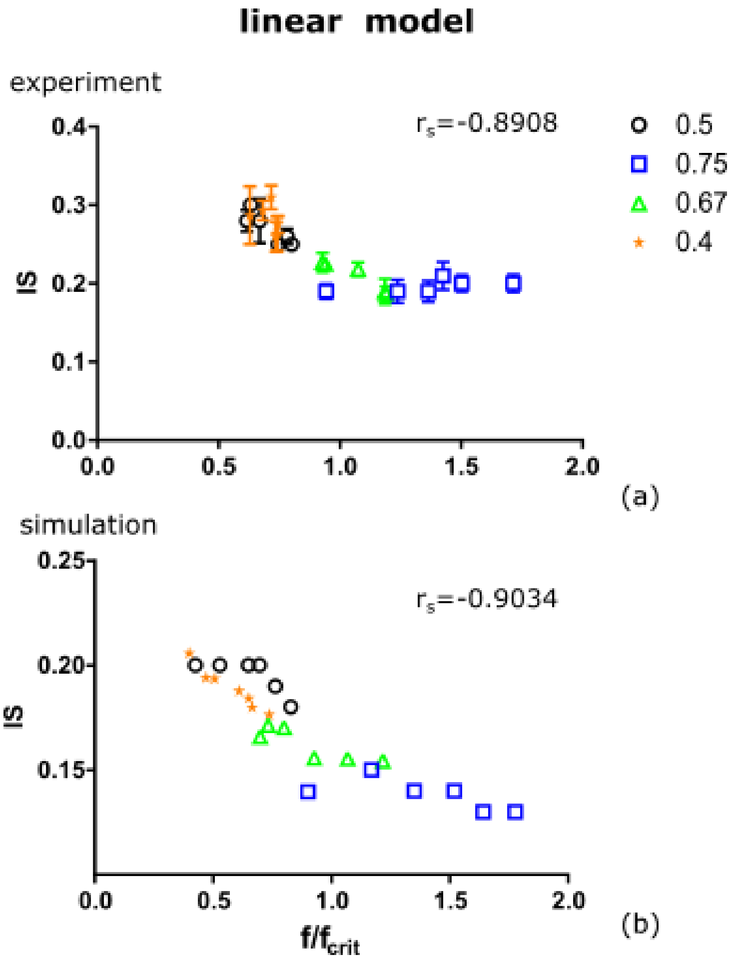

Figure 3.5: Fitted size linear model. Figure (a) shows experimental results while (b) shows simulation results. Both size ratio and rotation rate are variables. Each point presents one distinctive condition. Different colors denote different size ratios.

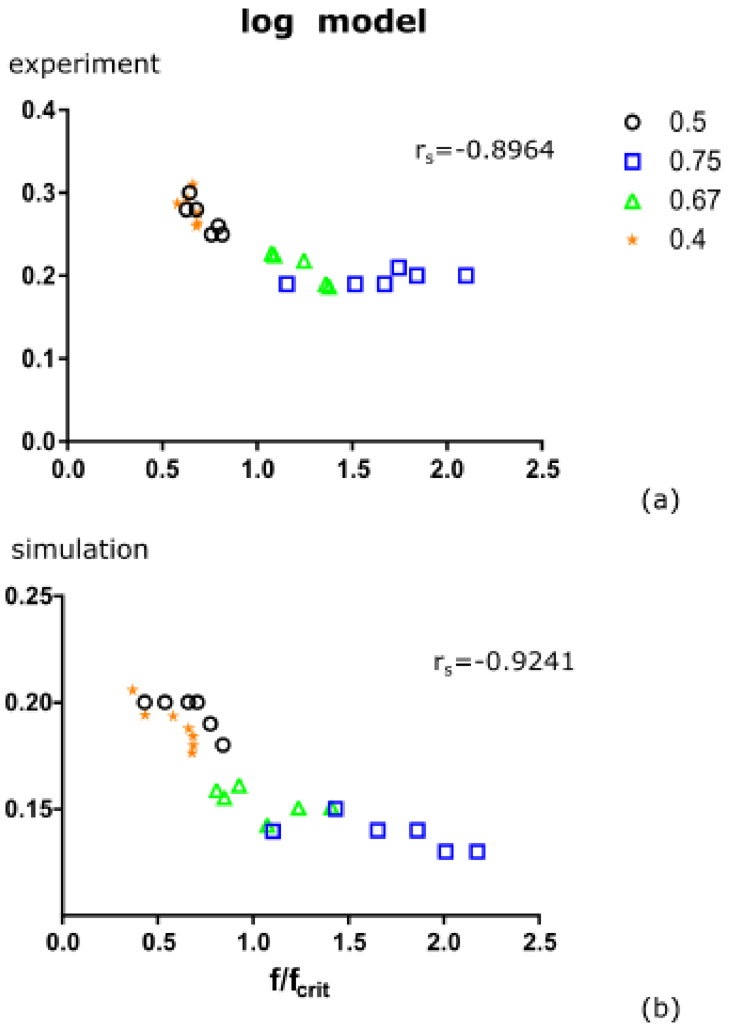

Figure 3.6: Fitted size log model. Figure (a) shows experimental results while (b) shows simulation results. Both size ratio and rotation rate are variables. Each point presents one distinctive condition. Different colors denote different size ratios.

3.5 CONCLUSION

A range of experiments and DEM simulations were carried out to study the surface flow in a quasi-2D rotating tumbler. Experiments were performed for a wide range of rotational speeds, particle densities, and particle sizes. The corresponding DEM simulations were run to compare results. The steady state situations of both experiments and simulations were analyzed using computational methods to analyze the IS value. For each condition, the corresponding parameters are plugged in different segregation velocity models. Based on the results, we have clearly established our framework as a sensitive semi-quantitative test of the validity of segregation rate models.

Our results show that for these two densities segregation models tested, the drag model fit in the framework better than the buoyant models; which indicates that drag force play an important role in density segregation. However, the IS value was reaching a constant value while f / f_{crit} value was still small. Further researches are necessary to find the right fitting parameters to fit in our experimental setting. For size segregation, the difference between models is less because of the similarity of those two models at the size range we tested. Both models are quite accurate based on our results. Our results show some inconsistency between experiment and simulation data. An improved experiment device or a new way to analyze segregation will be needed to overcome the experimental error caused by the existence of the physical glass wall.

This framework can experimentally validate existing and new kinetic models of segregation. It can also be used to predict or control the mixing extent of particle systems via manipulation of parameters such as rotation rate and particle ratio. And thus, contribute to an improved understanding of the segregation and mixing of granular materials.

4.0 A TRANSPORT ANALOGY FOR SEGREGATION AND GRANULAR RHEOLOGY

The content of this chapter is taken from Liu, S. & McCarthy, J. J. Transport analogy for segregation and granular rheology. Phys. Rev. E 96, 020901 (2017).

Segregation[62] is a costly phenomenon that has garnered research for decades [38,63,64]. In contrast, the study of dense phase granular rheology has only recently gained traction, but significant inroads have been made[65–69]. Despite these parallel strides, only a tenuous connection has been proposed[70] between these two seemingly disparate topics and work focusing on building a formal analogy is lacking, despite the synergistic advantages that analogies have afforded[71] in a variety of fields[72,73].

It is generally accepted[16,17] that the scaling of gravity driven density segregation is proportional to the density difference between species as well as to the local value of the shear rate within the flow (although segregation in the absence of gravity has been shown to be more complex[74,75]). This simple phenomenological scaling results in just three relevant dimensionless groups for segregation velocity, $\overline{v}_s = v_s / (\sqrt{g d_p})$, shear rate, $\overline{\gamma} = \dot{\gamma}\sqrt{d_p / g}$, and density, $\overline{\rho} = \rho_h / \rho_l$, where g is the acceleration due to gravity and d_p is the particle diameter; however, it does not account for the impact of varying boundary conditions (specifically, confining pressure P), thus it does not readily allow direct coupling between granular flow rheology and the segregation rate. In this Rapid Communication, we examine a simplified “ideal solution” segregating flow whereby isolated dense intruders segregate as a function of a host of rheological variables. By explicitly accounting for the confining pressure, we make a more direct connection between rheology and segregation. In this way, we not only shed light on how rheological-segregation coupling may be modeled, but also uncover a direct analogy between measurements of rheological variables and the resulting segregation rate.

A recent survey of density-based segregation models[76] found that a successful phenomenological model for the density-driven segregation velocity has been set forth by Tripathi and Khakhar[17]. They begin with a force balance on a single dense particle in a medium of light particles to get

$$0 = F_w - F_b + F_d \tag{4-1}$$

where F_w is the weight of the dense particle, F_b is the buoyant force, and F_d is the particle drag force. Taking the particle drag force to have a Stokesian form, they assume

$$F_d = \beta \pi \eta d_p v_s \tag{4-2}$$

where η is the particle medium viscosity, d_p is the particle diameter, β is a constant, and v_s is the segregation velocity. Assuming that the drag force and net particle weight are in balance, after simplification, yields an expression for v_s which may be written as

$$v_s = \frac{g d_p^2 (\rho_h - \rho_l)}{6 \beta \eta} \tag{4-3}$$

where g is the acceleration due to gravity and ρ_i is the density of the heavy (h) and light (l) particles, respectively. In order to recover the previously mentioned traditional scaling, one assumes that the stress τ within the granular flow is shear rate independent so that we can write

$$\eta = \frac{\tau}{\dot{\gamma}} \propto \frac{1}{\dot{\gamma}} \tag{4-4}$$

Based on the above equations, we recover that (1) v_s is proportional to the shear rate $\dot{\gamma}$ and (2) at a constant shear rate the segregation velocity v_s should scale as $(\rho_h - \rho_l)$.

To test these predicted scaling relations, yet at the same time allow for the variation of flow boundary conditions, we employ the discrete element method (DEM) to examine a wall-driven periodic plane shear cell. The details of the model can be found in a previous paper from our group[58]. Table I shows the material properties that were used in the simulations reported here.

Table 4.1: Material properties used in the simulations

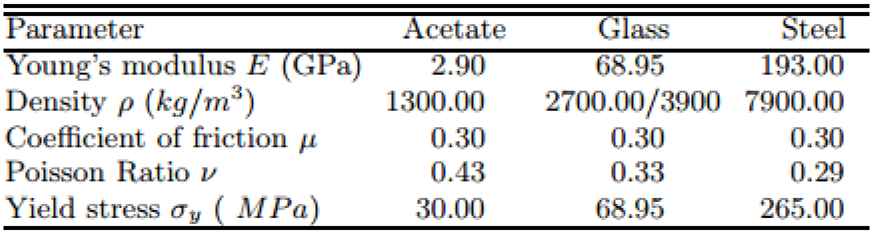

Parameter	Acetate	Glass	Steel
Young's modulus E (GPa)	2.90	68.95	193.00
Density ρ (kg/m^3)	1300.00	2700.00/3900	7900.00
Coefficient of friction μ	0.30	0.30	0.30
Poisson Ratio ν	0.43	0.33	0.29
Yield stress σ_y (MPa)	30.00	68.95	265.00

A schematic of the simulated three-dimensional (3D) plane shear flow system is shown in Figure 4.1. Periodic boundaries are used in both the x and z directions. In most trials, the majority of the particles have the same (light) density of $\rho_l = 1300\text{kg/m}^3$, material properties that roughly match cellulose acetate, and an average radius of 4.5 mm with a 10% particle size distribution to prevent crystallization. In some cases, we examine the impact of varying particle diameter over a range from d_p = 6.0 - 18 mm in 3.0 mm increments. For all simulations eight uniform heavy intruders (which have the same radius as the light particles, but with varying heavy density ρ_h) are randomly placed in the system. Three different ρ_h values are used (2700, 3900, and 7900 $\mathrm{kg/m^3}$), along with corresponding material properties that roughly match glass, ‘’heavy glass", and stainless steel, respectively. The top and bottom walls (shown as black in Figure 4.1 are roughened with particles and the top wall is given varying masses in order to examine the effect of confining pressure (P). Alternatively, several trials were run at a constant volume fraction (i.e., fixed height h) where we measured the time average of the pressure at the top wall (rather than prescribing the confining pressure). Shearing velocity is varied from 0.1 to 4.0 m/s (0.1, 0.5, 1, 2, 3, and 4 m/s) while the bottom wall remains static. To obtain a nearly homogeneous shear flow, fins made of wall particles are attached to both the top and bottom walls, and in most simulations we employ a modified gravitational field whereby (net) gravitational forces act only on the heavy intruders (similar to the approach of [77]). The particle bed is deep enough (15 particle diameters) that the segregating intruders reach a steady segregation velocity under all examined conditions. In a small number of simulations full gravity effects are included, however, due to shear localization in these cases we perform all calculations based on the local value of the shear rate (and only measure the segregation velocity while in the sheared region).

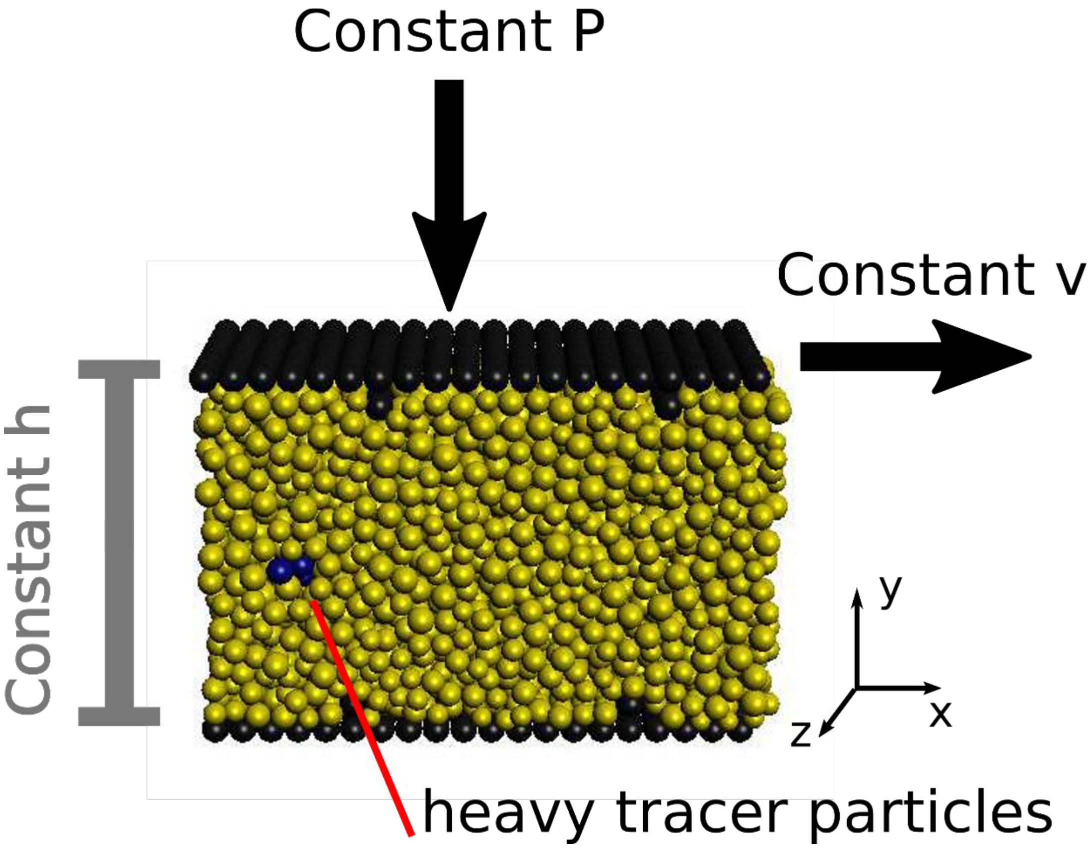

Figure 4.1: Schematic of the simulated plane shear geometry. The 3D flow is periodic in both the streamwise (x) and transverse (z) directions. Blue (dark) particles are heavy intruders while yellow (light) particles are lower density particles. We employ either constant pressure or constant volume boundary conditions.

In Figure 4.2 we show the dimensionless segregation velocity obtained for the average of the heavy intruders for three different density ratios under a range of boundary conditions (confining pressures versus fixed volumes and our modified gravity field versus full gravity), particle diameters, and shear rates. In Figure 4.2 (a), which shows the variation of $\overline{v_s}$ with dimensionless shear rate ($\overline{\gamma}$), we note that there are roughly three groups of curves, corresponding to each of the three density ratios; however, it is clear that there are a number of issues with this naive scaling. First, there is a systematic variation in the value of $\overline{v_s}$ for differing boundary conditions, whereby higher pressures and/or the constant volume cases result in a routinely smaller value of the segregation velocity. Second, when varying the particle diameter, we notice a qualitatively different shape to the scatter plot (it does not appear to pass through the origin, for example). Finally, when including the full effects of gravity, our segregation velocity values are uniformly lower than for the corresponding shear rates in modified gravity cases and ultimately the segregation rate saturates at dramatically larger values of the dimensionless shear rate.

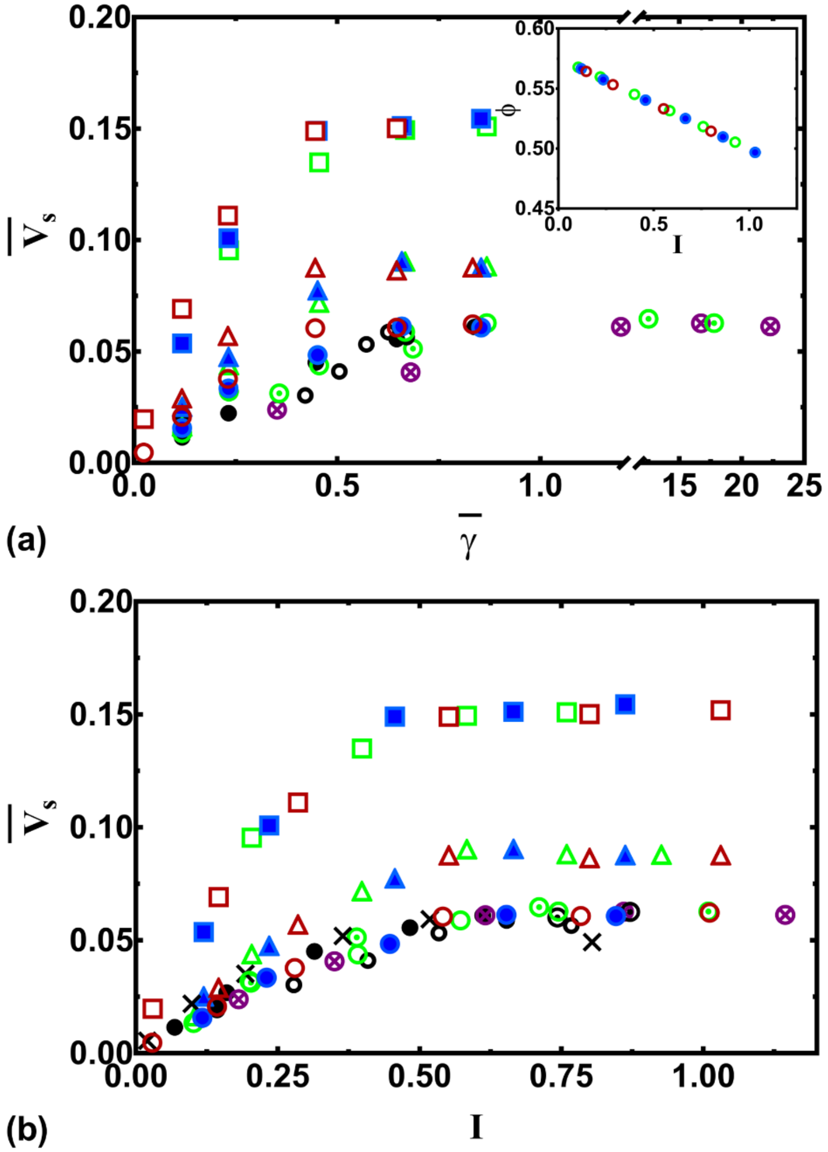

Figure 4.2: Segregation velocity under varying conditions of shear rate, density ratio, particle diameter, and boundary conditions. Differing colors represent boundary conditions [constant pressures: 78 Pa, -- red (dark gray); 117 Pa, blue (solid light gray); 156 Pa, green (open light gray); constant volume, solid circles; full gravity effects, dotted and crossed circles] while shape represents the density ratio (circle, $\bar{\rho}=2$; triangle, $\bar{\rho}=3$; square, $\bar{\rho}=6$). While most particles are 9.0 mm in diameter, the thick-walled open circles represent a range from 6.0 - 18.0 mm. (a) The dimensionless segregation velocities are plotted vs the shear rate made dimensionless with $\sqrt{g/d_p}$. The inset shows packing fraction as a function of I. (b) In this panel we have replotted the $\bar{v}_s$ as a function of inertia number (I). Note that the varying boundary conditions all collapse onto individual curves corresponding to different density ratios. In all figures, error bars on the data are smaller than the symbol sizes chosen.

In order to fix these issues with the scaling, and as a first step toward connecting segregation to granular rheology, in Figure 4.2 (b) we instead plot $\overline{v}_s$ against a different dimensionless shear rate, that of the inertia number (I). The inertia number[8], given as $I = \dot{\gamma} d_p \sqrt{\frac{\rho}{P}}$, is the final, relevant independent dimensionless group governing this problem, it relates the timescale of shearing to the timescale of consolidation, and has been a staple of constitutive model development in recent years [68,69,78,79]. We note that I is a better independent variable for correlating changes in segregation velocity as the scatter from pressure (and constant volume) variation is now eliminated in the higher density ratio (triangle and square) trials. Moreover, the low-density ratio (circle) case now collapses results not only for varying boundary conditions, but also for varying particle diameters and for both full and modified gravity cases (note that the modified gravity case uses the measured average bed pressure and the local shear rate in the calculation of I). Using the inertia number allows us to capture a clear observation that the segregation rate saturates [Figure 4.2 (b)] at a specific value of I in much the same way that the effective friction (μ_{eff}) is seen to saturate (at high Inertia numbers) in $\mu_{\text{eff}}(I)$ rheology [8,9]. Also, we note that, while our $\overline{v}_s$ results now collapse onto three curves regardless of particle size and boundary condition, the relevant scaling for the density ratio is not captured in this plot. This scaling is examined next.

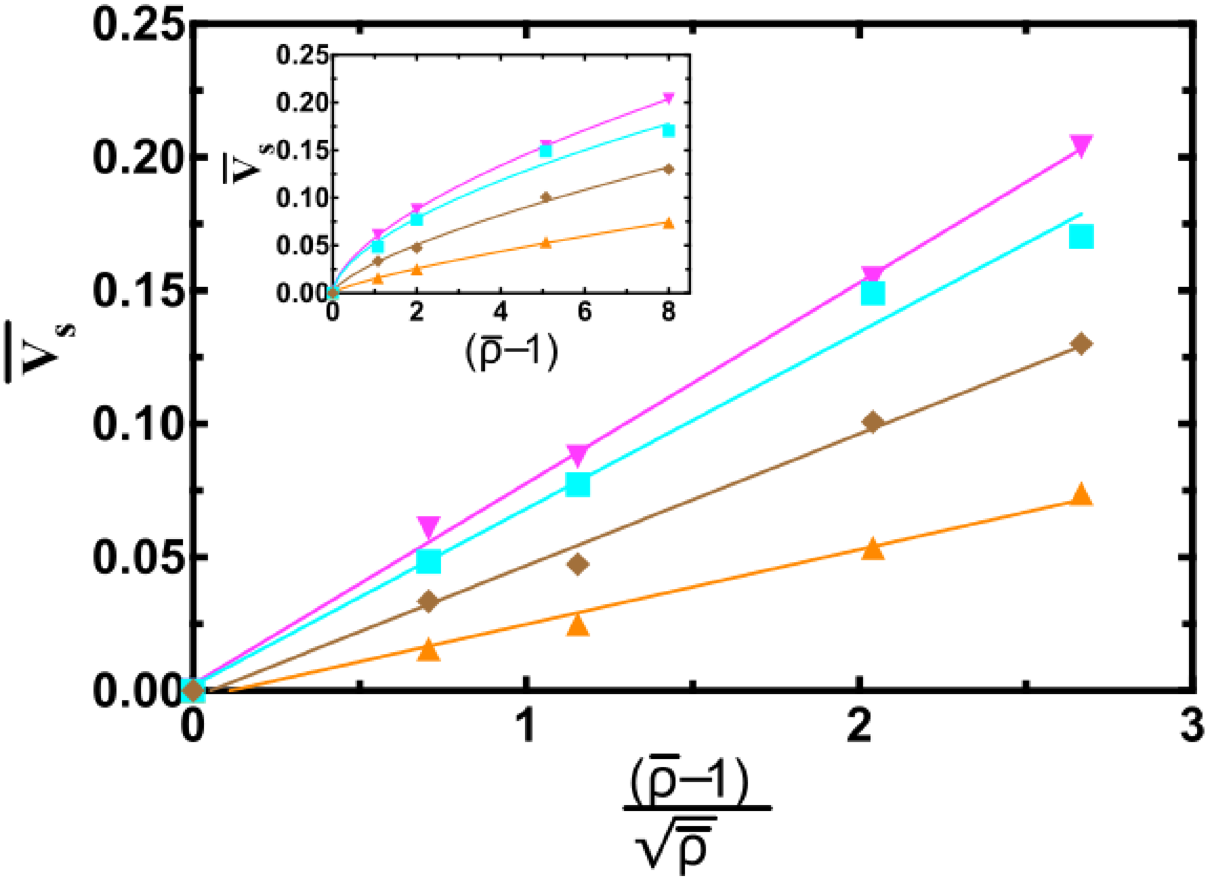

Figure 4.3: Variation of dimensionless segregation velocity with varying density at fixed values of the inertia number (upright triangle: I=0.1193, diamond I=0.2350, square: I=0.4563, inverted triangle: I=0.8627). The inset shows the traditional scaling of the segregation rate with the dimensionless density difference. Note that, in contrast to previous studies, we find a power law relationship with exponents that range from 0.6 to 0.75. In contrast, when we plot the segregation velocity vs our proposed density scaling, we obtain straight lines.

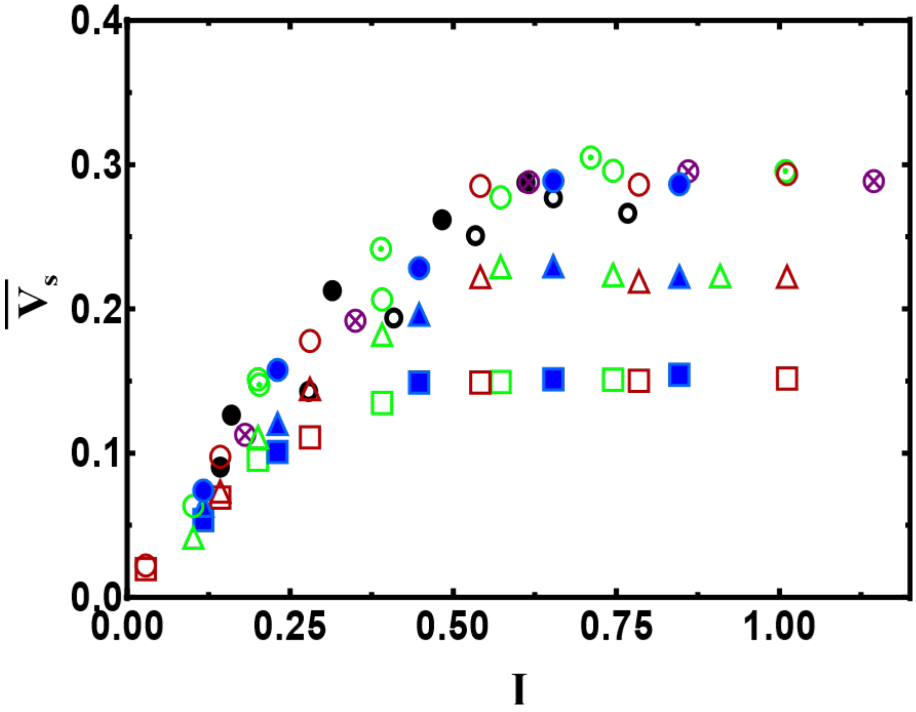

Figure 4.4: Traditional scaled segregation velocity under varying conditions of shear rate, density ratio, particle diameter, and boundary conditions. Differing colors represent boundary conditions [constant pressures 78 Pa, red (dark gray); 117 Pa, blue (solid light gray); 156 Pa, green (hollow light gray); constant volume, solid circles; full gravity effects, dotted and crossed circles] while shape represents the density ratio (circle, $\overline{\rho} = 2$; triangle, $\overline{\rho} = 3$; square, $\overline{\rho} = 6$). While most particles are 9.0 mm in diameter, the thick-walled open circles represent a range from 6.0 to 18.0 mm. The dimensionless segregation velocities are plotted vs the shear rate made dimensionless with $\sqrt{g / d_p}$. The magnitude of the segregation velocity is scaled by the traditional density scaling [that is, ($\rho_h / \rho_l - 1$)]. Note that, particularly in the saturated rate region, it is clear that this scaling does not collapse the data.

Turning to the impact of the density ratio, one can note that using the traditional density scaling suggested from Eq.(4-3) ($\rho_h / \rho_l - 1$), fails to collapse the data [that is, the plot in Figure 4.3(inset) does not lead to a straight line and Figure 4.4 does not collapse, especially on the saturated regime]. If we relax the assumption that all segregating flows operate in the rate-independent regime and instead develop a scaling relation for the local viscosity near a segregating particle, we can recast Eq.(4-3) and not only recover the proper density relationship (Figure 4.3, motivated below), but also establish a direct analogy between granular flow rheology and the segregation velocity.

We start by choosing a characteristic stress scale in the neighborhood of the heavy intruder(s) as the quantity $\tau_{char} \sim \rho_h g d_p$. If we similarly take the local shear rate to be related to a characteristic collisional velocity v_{coll} (to be identified later), divided by the particle diameter we obtain

$$\eta \sim \frac{\rho_h g d_p}{v_{coll}/d_p} \tag{4-5}$$

For a heavy intruder, a density dependence of the collisional velocity v_{coll} arises due to the fact that the intruder must undergo repeated collisions with the lighter ``background" particles. By performing a conservation of energy balance around a colliding particle [80], we obtain a post collision characteristic velocity given as $v_{coll} \sim v_o \left(\frac{\rho_h}{\rho_l} \right)^{1/2}$ where v_o may be thought of as the pre collisional characteristic velocity. Combining these expressions, we can write an equation for the viscosity near a heavy intruder particle that is segregating within a granular fluid as

$$\eta \sim \frac{\rho_h g d_p^2}{v_o \left(\frac{\rho_h}{\rho_l}\right)^{1/2}} \tag{4-6}$$

This simple model suggests a modification of the density scaling from what is traditionally used whereby

$$v_s \sim \frac{v_o(\bar{\rho}-1)}{\sqrt{\bar{\rho}}}. \tag{4-7}$$

As a direct test of this scaling, we plot the measured segregation velocity as a function of this density scaling for fixed values of the inertia number (see Figure 4.3). Note that each set of results examined lies on a straight line whose slope is a function of the inertia number chosen and that all curves correctly pass through the origin.

In order to more fully realize the form of Eq. (4-7), we finally examine the characteristic (pre) collisional velocity v_o. Obviously, in the absence of interactions with neighboring particles, the characteristic velocity of a falling intruder would scale as $\sqrt{d_p g}$ (motivating the choice of dimensionless scaling thus far used). If we argue that the relevant velocity is actually a "frustrated free fall" whereby the characteristic velocity varies from this scaling value solely due to interactions with neighboring particles, we can write that the number of interactions with neighbors per unit time is captured by the product of the coordination number z and the shear rate, $z\dot{\gamma}$ That is, the quantity $z\dot{\gamma}$ may be thought of as the inverse of the time between interparticle interactions (note that z has been shown to be a function of the inertia number[69,78] so that, at higher inertia numbers, the time between interactions increases). We note that, in our results, the average coordination number per particle decreases from a finite static value via a power law of the form $z \sim I^{-a}$ -similar to what was discussed by DaCruz et al.[67]

However, as seen in Figure 4.5(a), we find two regimes where $a = 1/3$ and 1 for I values below and above 0.5, respectively. We note that this transition point is coincident with the saturation location of both the effective friction coefficient, μ_{eff}, and the segregation velocity. Finally, if we limit the effective number of neighbor interactions to those that occur faster than the consolidation time-scale, $t_c = d_p(\rho_l / P)^{1/2}$, we obtain a choice of v_o that is given by

$$v_o \sim (\sqrt{d_p g}) z \dot{\gamma} t_c = (\sqrt{d_p g}) z I \tag{4-8}$$

One way to interpret our scaling in Eq.(4-8) is that the maximum time between collisions is the consolidation time. Thus, in the limit of large I, we obtain free-fall scaling during the full extent of the consolidation time. At the other extreme, where the time between collisions is small, the ``frustrated-free fall'' velocity can become quite small. Combining Eq.(4-7) with Eq.(4-8) and recovering the constants from previous equations yields an expression for the dimensionless segregation velocity as

$$\bar{v}_s = \frac{v_s}{\sqrt{d_p g}} = \frac{z(\bar{\rho}-1)}{6\beta\sqrt{\bar{\rho}}} I \tag{4-9}$$

Thus, by using our scaling, and determining a relationship between the collision frequency and inertia number (I), we yield a closed form equation for segregation velocity that includes only a single parameter β that captures the drag force felt on a segregating particle [as well as an $O(1)$ correction to our collision velocity scaling argument]. Figure 4.5(b) shows the relationship between segregation velocity (scaled with our density relation) and I for all simulation conditions studied and includes a line corresponding to Eq.(4-9) with $\beta = 1$ (which, in a fluid system, would imply that form drag is small compared to frictional drag).

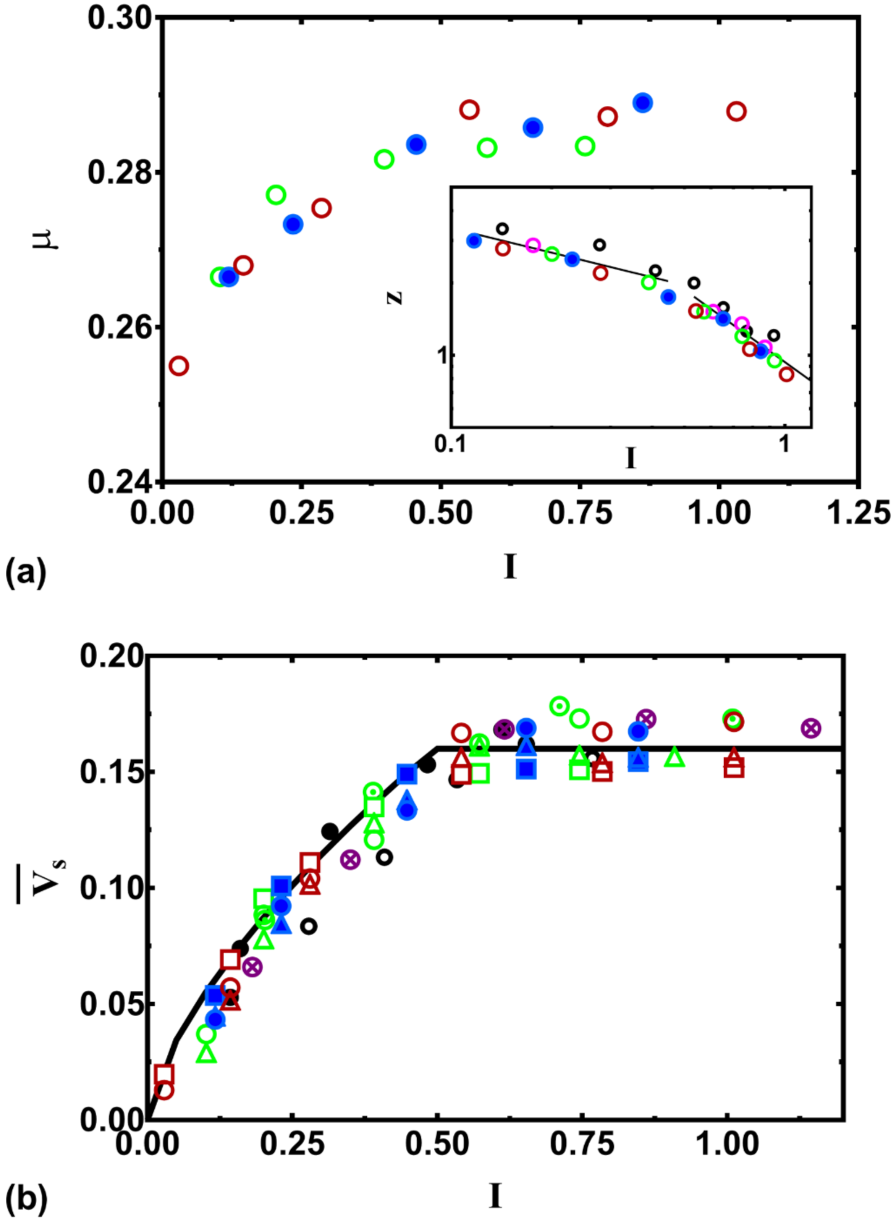

Figure 4.5: Rheology and segregation in a sheared cell system under varying conditions of shear rate, density ratio, particle diameter and boundary conditions (symbols explained in Figure 4.2). (a) shows how the effective friction coefficient changes with the inertia number. The inset shows the variation of the coordination number with I. Note that both rheological quantities display a regime change near a value of I = 0.5. (b) shows the dimensionless segregation velocity rescaled with our proposed density scaling [Eq.(4-7)] and plotted against I. Note that all results fall on a master curve regardless of gravitational condition, boundary condition, or other process parameters. The included line represents the model proposed in Eq. (4-9). The inset shows the packing fraction as a function of I.

It is interesting to note that the location of the segregation velocity (and μ_{eff} & z) transition corresponds to the value of I where the solid packing fraction decreases below a value of roughly $\phi \approx 0.52$ [Figure 4.2(a) inset]. This value of the packing fraction is characteristic of a simple cubic lattice of equal sized spheres. While the rheological transition from linear $\mu_{\text{eff}}(I)$ to saturated μ_{eff} has been reported at varying values of I in the literature[8,67,69], examining these transitions in light of this packing fraction observation one notes that a simple cubic solids' fraction criterion would identify this critical I value irrespective of whether the system is 2D[65,81] or 3D[69]. Regardless of the origin of this transition, here we show that recasting our data in light of the inertia number collapses our results onto a single master curve for a wide variety of process variables, boundary conditions, and gravitational conditions and allows us to recognize - and predict the location of - a regime where the segregation rate saturates. This observation could have significant industrial importance as it could enable the rationale design of industrial processing methods that could lead to dramatically reduced segregation extents since operating in the ``saturated" regime (i.e., at high I values) will enable more rapid processing to reduce the ultimate degree of segregation observed. Moreover, this work highlights that density-based segregation is not only coupled to the underlying flow rheology in shearing geometries, but that a true analogy exists whereby determination of the relationship between the coordination number (z) and I can lead directly to a quantitative expression for the segregation velocity (and likely vice versa).

5.0 PARTICLE DENSITY SEGREGATION IN GRANULAR SHEAR FLOW: MODELING AND EXPERIMENT

Granular particles have long been known to segregate when they possess different properties such as density, size and shape; but the physics of this phenomenon is complicated and not fully understood even now. Segregation in shear flow is especially important as it is common in multiple industrial processes. While there are a handful of studies that focus on density segregation within dense shear flows[17,32,52], there is to date no fundamental understanding of segregation's density dependence and pressure dependence. In our previous computational study[76], we tried to tackle this problem by connecting density-based segregation with granular rheology. Here, we perform experiments similar to our simulation setting in an attempt to physically back up our proposed theory and computational results.

In our previous work, we examined density segregation behavior within a simulated "ideal flow condition " (plane shear cell) and made a connection between segregation velocity v_s and flow rheology by introducing the inertia number I[8], given as $I = \dot{\gamma} d_p \sqrt{\rho / P}$. In the definition of inertia number equation, $\dot{\gamma}$ is the shear rate, d_p is the particle diameter, ρ is the particle density and P is the confining pressure of the system. Our proposed dimensionless segregation velocity model is shown as in Eq.(5-1). In this equation, $\overline{v_s}$ is the dimensionless form of the segregation velocity, β is a fitting parameter, g is the acceleration due to gravity, z

is the particle coordination number, $\bar{\rho}$ is the density ratio between the heavy ρ_h and light ρ_l particles and I is the inertia number based on the granular flow properties. The coordination number z is not a directly measurable parameter under most experimental conditions, but we noted that, based on our simulation, z had a direct correlation with I similar to what has been found by others work[67]. The average coordination number per particle has two regimes and under both regimes it decreases with the inertia number via a power law of the form $z \propto I^{-a}$ with $a = 1/3$ and 1 for I value below and above 0.5, respectively.

$$\bar{v}_s = \frac{v_s}{\sqrt{d_p g}} = \frac{z(\bar{\rho}-1)}{\beta\sqrt{\bar{\rho}}} I \tag{5-1}$$

This new model is based on two conclusions which are contrary to the conventional wisdom within the literature. (1) We found that v_s is not linearly proportional to the shear rate $\dot{\gamma}$ as generally accepted[17,82,83]. Instead, v_s is linked to the inertia number I, which partially depends on $\dot{\gamma}$. Moreover, v_s will reach a constant value once I reaches a critical value. (2) Under the same I, v_s scales with the density ratio $\bar{\rho}$ as $\frac{\bar{\rho}-1}{\sqrt{\bar{\rho}}}$, rather than the more intuitive $(\bar{\rho}-1)$. It should be noted that one possible rationale for at least a portion of these discrepancies is that our study involved only heavy intruders (i.e., a vanishingly small concentration), rather than a more balanced binary mixture.

To test our simulation/theory, we have performed experiments trying to mimic, as closely as possible, our simulated conditions. We constructed an experimental annular Couette cell as shown in Figure 5.1 with a vertically movable bottom plate. Particles are confined between two cylindrical rings and between the top and bottom plates. The radius of the inner steel ring of the annulus is 25.35 mm and the radius of the outside glass ring is 59.45 mm. Both top and bottom plates are made of steel to dissipate static charge. Four fins are attached to both plates to prevent particle slipping. A computer controlled ClearPath motor is used to run the experiments under four different rotation rates (10, 20, 30 & 40 RPM). A Sony Digital Still Camera DSC-RX10M3 is used to obtain two types of videos. (a) 240 fps high frame videos. The high frame videos are taken and later analyzed in PIVLab to capture the flow direction velocity (u) profiles. (b) normal videos. Those videos are later cut into images using 15 fps setting to manually trace heavier tracer particle's (steel) segregation behavior. The majority of the particles (either glass or acetate) inside the system have a diameter of 3 mm while a trace amount ($\sim 10\%$) of differently sized particles (either 2.38 or 3.175 mm) with similar density are added into the media to prevent crystallization. Steel particles are always used as the tracer particles and thus in this experiment, we test v_s under two different density ratio sets ($\overline{\rho} = 2.8$ and $\overline{\rho} = 5.9$). The properties of the three types of particles used in this experiment are shown in Table 5.1. A strong magnet is used to attract steel tracer particles towards the glass surface in order to more easily capture the segregation behavior and to reset the experimental conditions. Since the magnet is only used outside of the video recording zone, we believe this action does not impact the measurable segregation velocity. Before each trial of experiment, the experiment cell is always rotated and running upside down since we found that flows to be much easier to shear from the bottom than from the top. Two different experimental configurations were run. Under the constant pressure (CP) configuration, the top aluminum bar is allowed to move and a constant pressure is applied toward the particle media with a pressure around 2300 Pa. Under the constant volume (CV) configuration, the top aluminum bar is lifted off the particle surface just slightly and secured to prevent movement. A comparison of the segregation velocity under those two conditions can show how v_s varies with parameters other than shear rate and thus, shows the direct impact of pressure/inertia number on density segregation.

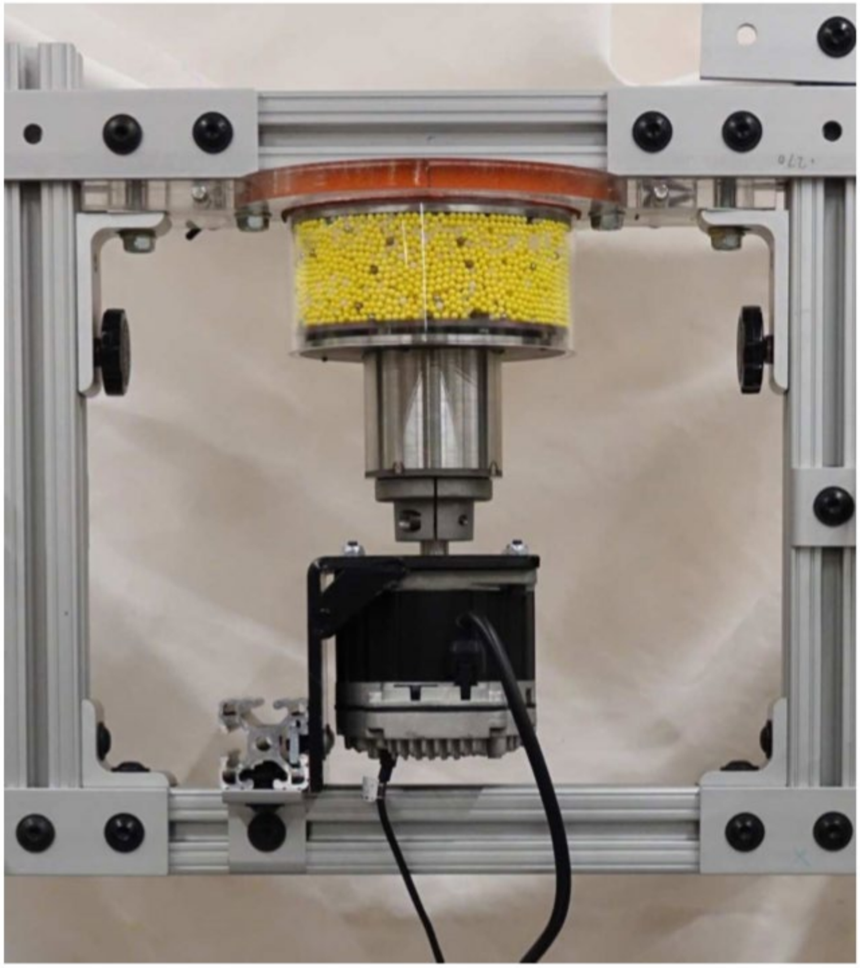

Figure 5.1：Experimental apparatus set up. Photograph are taken with 3mm tracer steel particles within an acetate particle medium

Table 5.1:Material Information used in the Experiments

Parameter	Acetate	Glass	Steel
Density ρ (kg/m^3)	1280	2700	7600
Number of Particles	15 000	12 000	100

The measured average horizontal velocity (u) as a function of height (H) for glass media particles is shown in Figure 5.2. In most cases, only part of the bed is able to be shared and only velocity at the shear-able portion of bed is shown in the figure. The acetate horizontal velocity profile is not shown because it looks almost exactly the same as the glass case. All velocity profiles have close to an exponential function shape so an exponential trend line is calculated for each condition and then the shear rate $\dot{\gamma}$, which is one of the actual controlling parameters driving segregation, is calculated based on the local slope of this trend line.

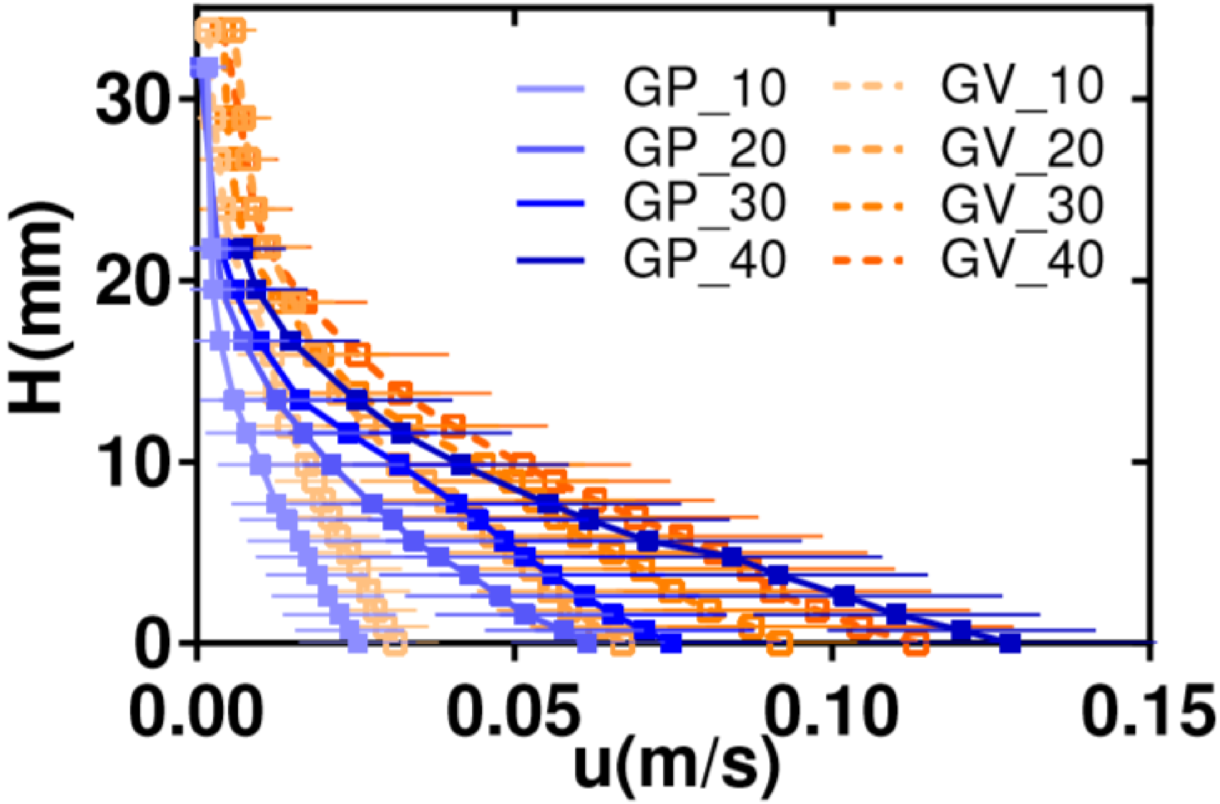

Figure 5.2：Measured glass velocity profile u as a function of cell height(H) for both constant pressure (CP) and constant volume (CV) conditions. H equals to zero represent the bottom of the cell

The measured global solid volume fraction ϕ_g is roughly equal to 0.59 under the constant pressure configuration and 0.58 under the constant pressure configurations. Although the global solid volume fraction does not vary dramatically under different configurations, the local solid volume fraction ϕ_l, which varies with cell height (H), can be much more sensitive. There is no simple method to measure ϕ_l but Figure 5.3 shows indirectly how ϕ_l varies. As the figure shows, lower H value has higher v_s. This can be explained by higher shearing rate near the bottom plate but it can also be explained by a lower ϕ_l. Furthermore, at the same H value (and roughly the same $\dot{\gamma}$), v_s is in generally higher under the CV configurations compared with the CP configurations. In this case, lower ϕ_l, (not $\dot{\gamma}$), is more likely to be the reason for higher v_s. Since we know ϕ is related to I directly[67,76], Figure 5.3 can be seen as the first evidence showing that v_s depends on I.

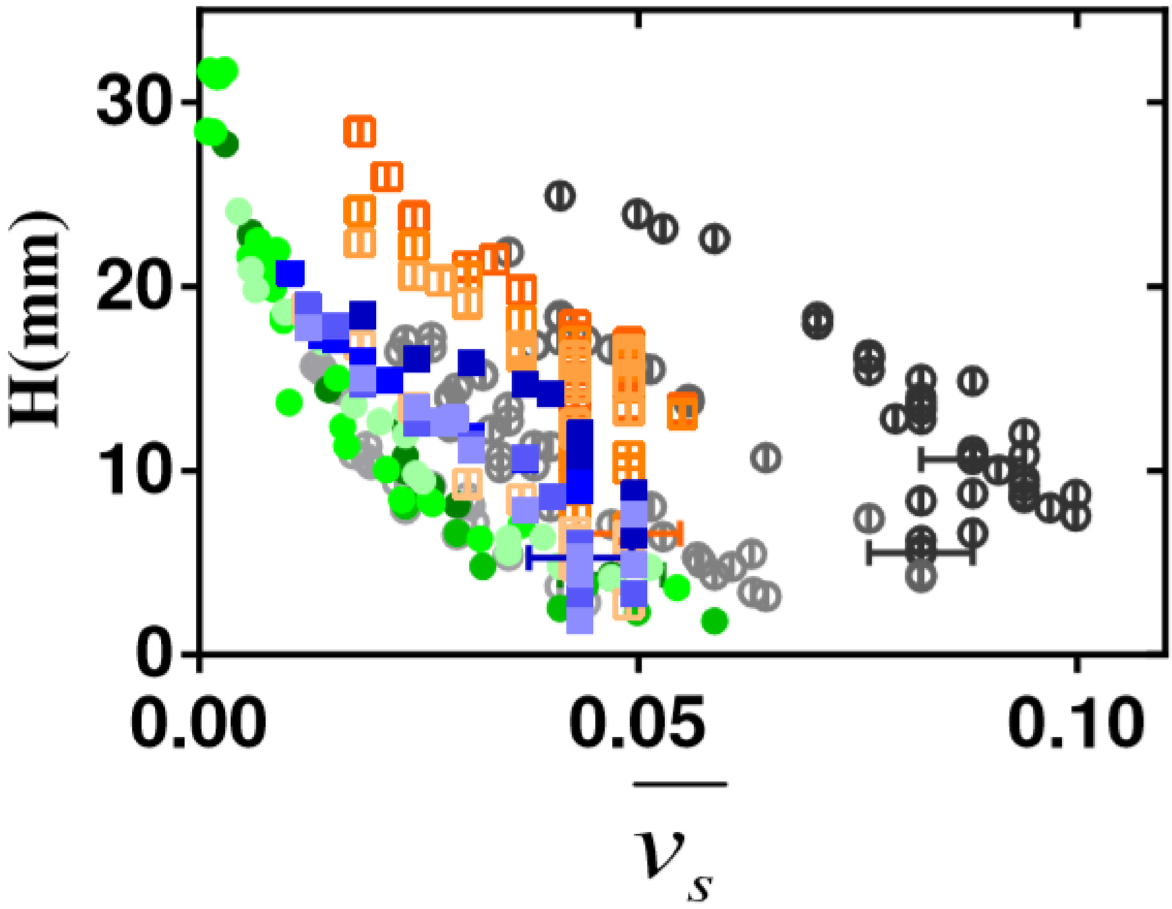

Figure 5.3: Measured dimensionless segregation velocity $\overline{v_s}$ as a function of cell height(H) for both constant pressure (CP) and constant volume (CV) configuration and for both acetate and glass bulk particle systems. H equals to zero represent the bottom of the cell. The legend used is same as in Figure 5.5. Only several error bars are present to simplify the plot but actually each data point have the same standard deviation

Although the initial confining pressure of the system is measurable, we don't really have a method to calculate the dynamic pressure inside the system while the bottom plate is rotating. Under different rotation rates, the actual pressure applied on the particles is likely to be different. Since pressure is one of the parameters within the inertia number, we need a way to quantify it. Two assumptions are made in order to calculate the pressure. Based on our proposed theory, v_s is proportional to $z*I$ and while v_s is at the increasing regime, z is proportional to $I^{-1/3}$. Thus, if we assume this correlation is correct, v_S should be proportional to $I^{2/3}$ in the segregation velocity increasing regime. Furthermore, we can assume that the pressure within the system is a constant under the assumption that the hydrostatic pressure is negligible comparing to the dynamic pressure caused by shearing. Based on those two assumptions, when we plot v_s as a function of $\dot{\gamma}^{2/3}$, the slope (k) of the increase part of the plot should be proportional to the pressure. Thus, the slope $k \propto C^2 * P$, where C is a scaling parameter. In this way, although the exact value of pressure is still unknown, we are able to qualitatively compare pressure under different configurations. We followed this logic to calculate $C^2 * P$ but because of limited data sets and the influence of hydrostatic pressure, a big uncertainty is involved. Figure 5.4 shows the pressure scale ($C^2 * P$) under each rotation rate.

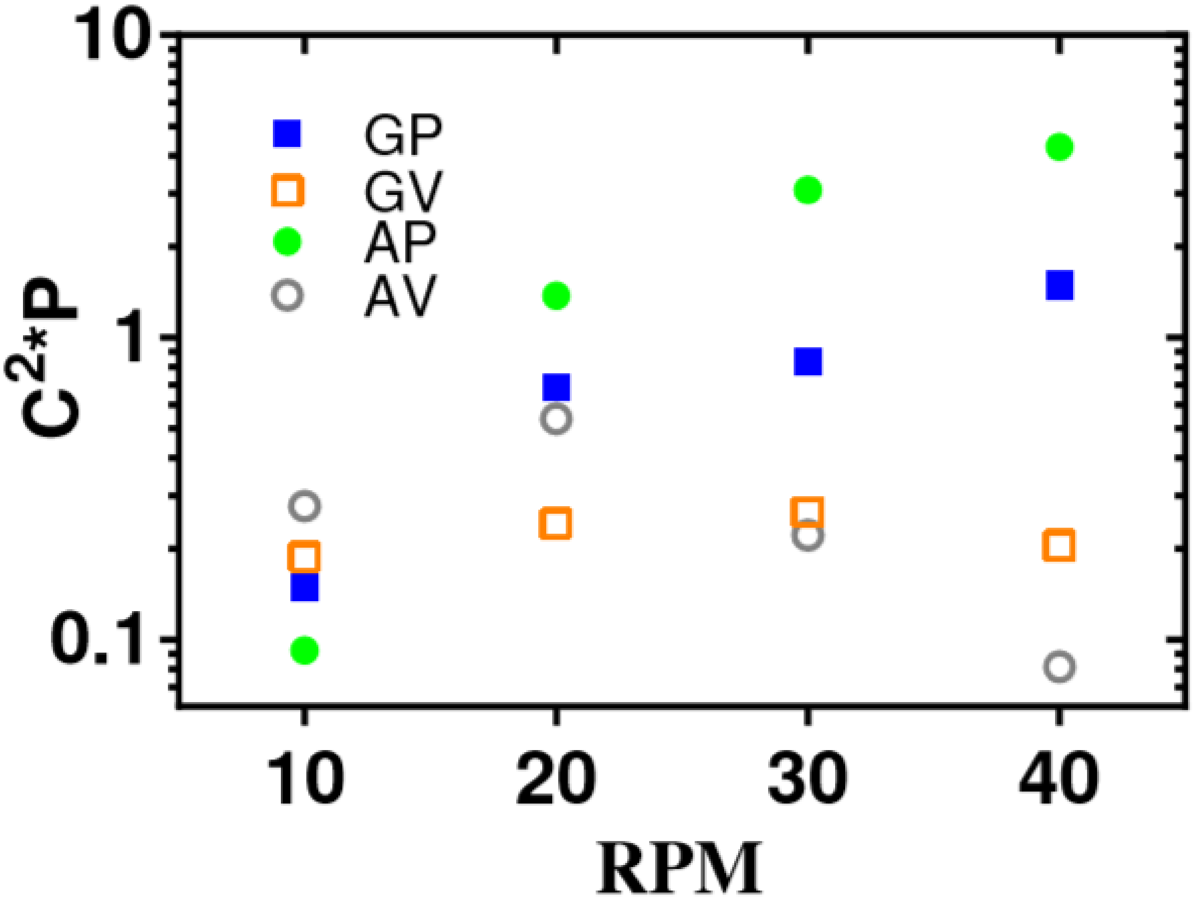

Figure 5.4: The scaled pressure C2∗P for glass constant pressure (GP), constant volume (GV) cases and acetate constant pressure (AP), constant volume (AV) cases under each rotation rate (10, 20, 30 & 40 RPM).

Figure 5.5 shows how the segregation velocity changes with inertia number for both acetate and glass conditions. As the figure shows, both $\overline{v_s}$ reaches the saturated regime once I is big enough. Only several error bars are shown in figures because all data points have the same error scale. The error comes from the fact that a pixel is the smallest unit for length measurement and when measuring particle's travel distance, the potential error is usually around 2 pixels. One 3 mm particle has the length of around 45 pixels. Since the experimental configuration is not exactly same as our previous simulation and the real-life flow condition is more complicated than a simplified simulated flow, we are not certain that v_s should become saturated when I reach 0.5. Here we used the fitting parameter C to adjust the scale of I so $\overline{v_S}$ becomes saturated at $C * I \approx 0.5$ solely for the purpose of easier comparison with our simulated results. Figure 5.5.(a) in general has a higher $\overline{v_s}$ than Figure 5.5.(b). This is no surprise since the density ratio $\bar{\rho}$ for steel in acetate is much higher than steel in glass. The value of $\overline{v_s}$ is in general smaller compared to our simulation result, but this can simply cause by differing particle properties. Figure 5.5 supports our earlier conclusion that v_s is not linearly increasing with shear rate and that v_s will saturate at high inertia number.

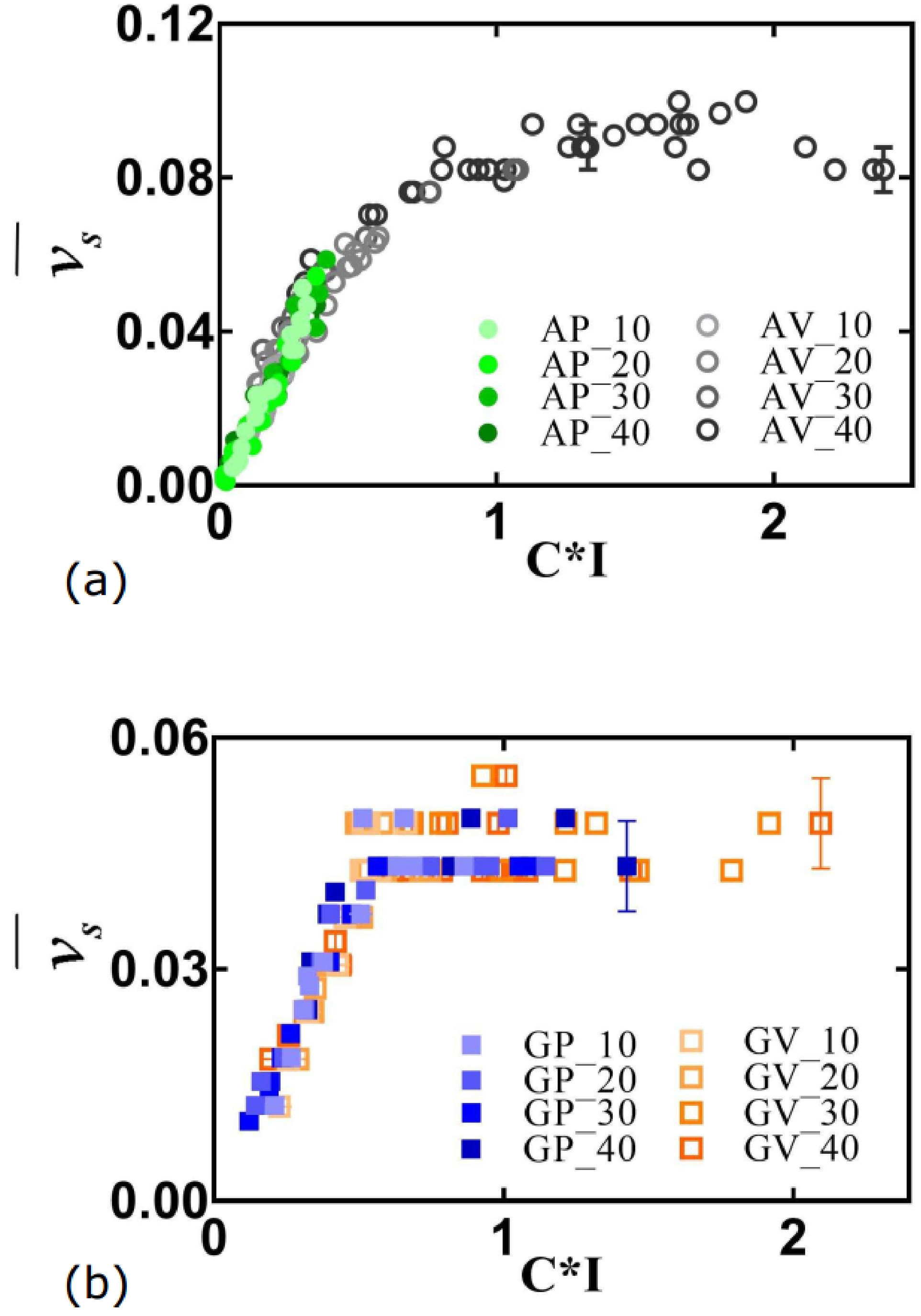

Figure 5.5: The dimensionless segregation velocity $\overline{v_s}$ as a function of scaled inertia number (C ∗I). Plot (a) represents both acetate constant pressure and constant volume conditions and plot (b) represents glass constant pressure and constant volume conditions.

In order to test the second conclusion, we scaled the $\overline{v_s}$ for steel in glass cases (GP & GV) with the proposed density ratio $(\overline{\rho}-1)/\sqrt{\overline{\rho}}$ to the steel in acetate case level. In other words, we multiply the $\overline{v_s}$ value in Figure 5.5.(b) by 1.87. If our previous proposed conclusion is correct, the two different curves should collapse together, especially at the saturated regime. This is mostly true as shown in Figure 5.6. Thus, Figure 5.6 also supports that our proposed segregation density dependence.

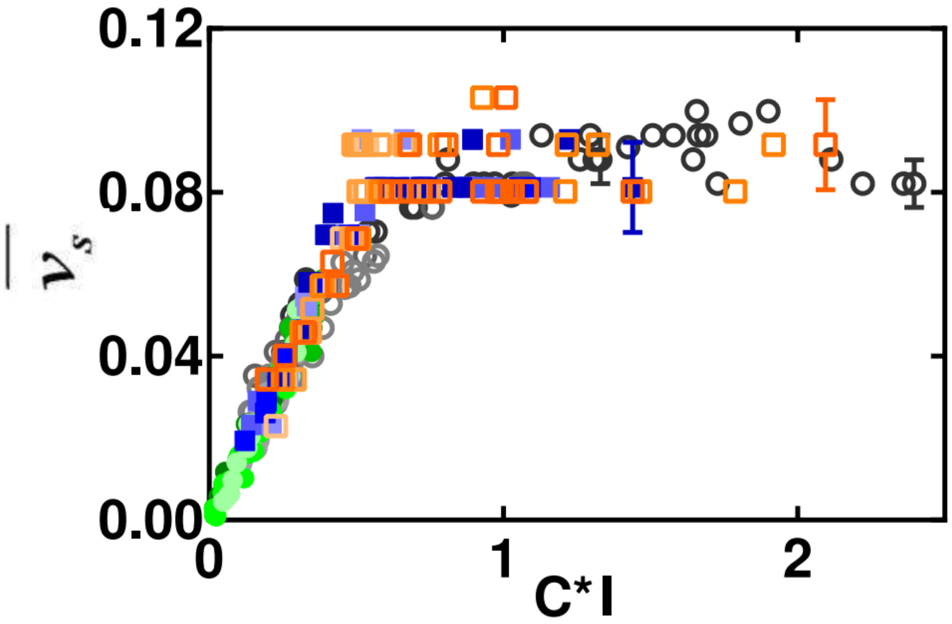

Figure 5.6: The re-scaled dimensionless segregation velocity $\overline{v_s}$ as a function of scaled inertia number ($C*I$). The legends are same as in Figure 5.5.

These experiments help to strength our theory that density-based segregation is directly related to the flow rheology and particle density segregation has a saturated regime. The saturated behavior of segregation could have significant industrial impact since it could potentially be used to redesign mixing devices to dramatically decrease the segregation extent of a process.

6.0 A RHEOLOGY PERSPECTIVE OF SHEAR INDUCED SIZE SEGREGATION

6.1 INTRODUCTION

Dry granular materials are ubiquitous in day to day life and are second only to water as the world's most handled industrial material[68]. When random mixtures of granular material of different properties -- such as size or density -- are handling in the presence of a gravitational field, segregation can occur. Segregation is usually undesirable and can result in unstable product quality and/or cause handling and processing difficulties. Size segregation is particularly important due to its ubiquity within industrial contexts, thus this mode of segregation poses a costly problem to industrial practitioners.

For size segregation, it is generally believed that there are two dominant mechanisms leading to the ultimate behavior observed. First, inter-particle percolation is a void-filling mechanism similar to the concept of "random fluctuating sieve" that tends to result in smaller particles moving in the direction of gravity while, secondly, squeeze expulsion is the process by which individual particles are squeezed out of one layer due to an imbalance of contact forces[84,85]. This paper will focus on the net result of these processes where shear-induced dilation causes small particles to move though the voids between bigger particles under the influence of gravity. Cook and Bridgwater[86] argued that statistical mechanics can be used to explain percolation since small particles are statistically more likely to fall down into voids than are bigger particles. Here we adopt this formalism and integrate their ideas with recent work on the impact of granular rheology on (density) segregation[76].

There have been several binary particle size models that have tried to predict particle concentration changes using a continuum model approach and some have been quite successful[28,87,88]; however, the accuracy of these models is highly dependent on both the choice of the size segregation model embedded within the method as well as the choice of model parameters used. While many previous researchers have examined size segregation under varying conditions[77,89–91], the fundamental equations governing the percolation process is still unclear. Thus, a study performed within one geometry may not be successfully extended to other geometries and a model that works under one range of shearing conditions may not fit other conditions. Recently, the study of the relationship between segregation and flow rheology has begun to gain traction[70,92]. Nevertheless, and despite the fact that studies show that segregation is influenced by volume fraction, stress and local friction coefficient, etc. at present no direct connections between rheology and size segregation has been articulated within the literature.

In the current work, we focus on size segregation in a well-defined and controllable system, that of a simple sheared cell with vanishing concentration of segregating material, in order to build a fundamental size segregation model. We combine our previous findings related to the impact of flow rheology on density segregation with a probability function (similar to the approach of Cook and Bridgwater[86]) in order to build a new model which is able to accurately capture/predict segregation results under a wide variety of operational conditions.

6.2 MATERIAL AND METHODS

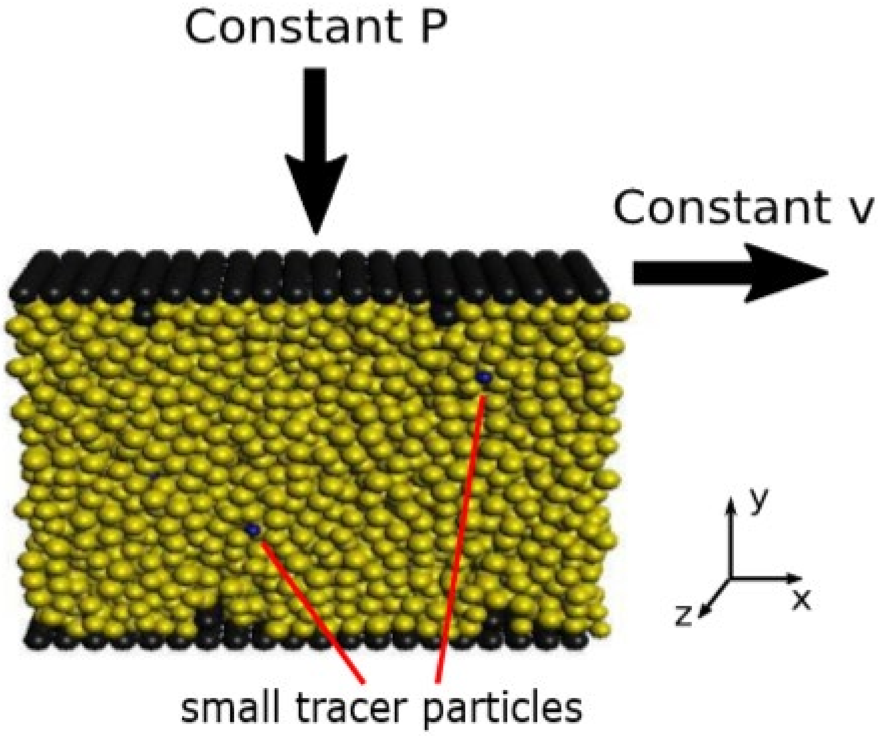

Figure 6.1; Schematic of the simulated plane shear geometry. The 3D flow is periodic in both the stream-wise (x) and transverse (z) directions. Yellow (light) particles are big bulk particles and blue (dark) particles are small intruders. The size ratio in the picture is 0.67. Constant pressure boundary condition is employed.

For this study, we used the similar approach as for our density study[76]. We employ the discrete element method (DEM) to examine a wall-driving periodic plane shear cell. The details of the DEM model can be found in a previous paper from our group[58,93]. In all of our trials, particles have the property that roughly match cellulose acetate (shown in Table 1). In most trials, the majority of the particles have the same average diameter (9 mm) with a 20% particle size distribution to prevent crystallization. In some cases, particle diameter of 3 and 6 mm were examined in order to check the scalability of our theory. For all simulations, eight uniform small intruder (which have the same density as all other particles, but with varying smaller diameter) were randomly placed in the system. Five different size ratios were tested (0.35, 0.4, 0.5, 0.67 and 0.75). For the majority of figures in this paper we show only 3 size ratios, for simplicity; however, when comparing theory with measurement, all 5 size ratios are used. The top and bottom walls of the shearing cell are roughed with immobilized particles and the top wall is given varying masses in order to examine the effect of confining pressure P. The pressure ranges from 78 to 3120 Pa. The shear rate is varied from 7.6 to 60 1/s while the bottom wall remains static. To obtain a nearly homogeneous shear flow, in most cases, only the small tracer particles were subject to gravitational forces in a similar fashion to the work of Khola[77]. While it is expected that doing this will cause the equivalent of both size and density segregation, we have found that the measured size segregation values under this approximation are comparable with a handful of full gravity simulations that we have run. Thus, in accord with the general consensus in the literature, we find that the impact of the (small) density segregation is negligible relative to that of size segregation under the conditions examined here.

Table 6.1: DEM Material Properties

Parameter	Acetate
Young's modulus E (GPa)	2.90
Density ρ (kg/m^3)	1300.00
Coefficient of friction μ	0.30
Poisson Ratio ν	0.43
Yield stress σ_y (MPa)	30.00

6.3 SIMULATION RESULTS

In our simulations, we measure the segregation velocity by calculating the vertical distance that the smaller particles travel during a period of time. First, the dimensionless form of the segregation velocity $V_s / \sqrt{gd}$ is plot as a function of dimensionless shear rate γ in order to check whether the widely used linear shear rate scaling[21,94] is observed under the conditions examined here . The results shown in Figure 6.2 illustrate that, despite testing three different methods of rescaling the shear rate -- i.e., $\frac{\gamma}{\sqrt{dg}}$, $\frac{\gamma d}{\sqrt{T}}$, and $I = \gamma d\sqrt{\frac{\rho}{P}}$ - V_s is not seen to linearly depend on shear rate over our range of shearing values. In addition, it is clear that none of the tested scaling yield a recognizable trend in the data.

In related work on density segregation[76], our group has found that there is a sharp transition in segregation behavior as a function of the Inertia number (I). While the plot in Figure 6.2.c is not able to collapse data, for a single value of larger particle and intruder size ratio there is some indication of a similar transition behavior when I reaches 0.5 (e.g., observe the triangle results).

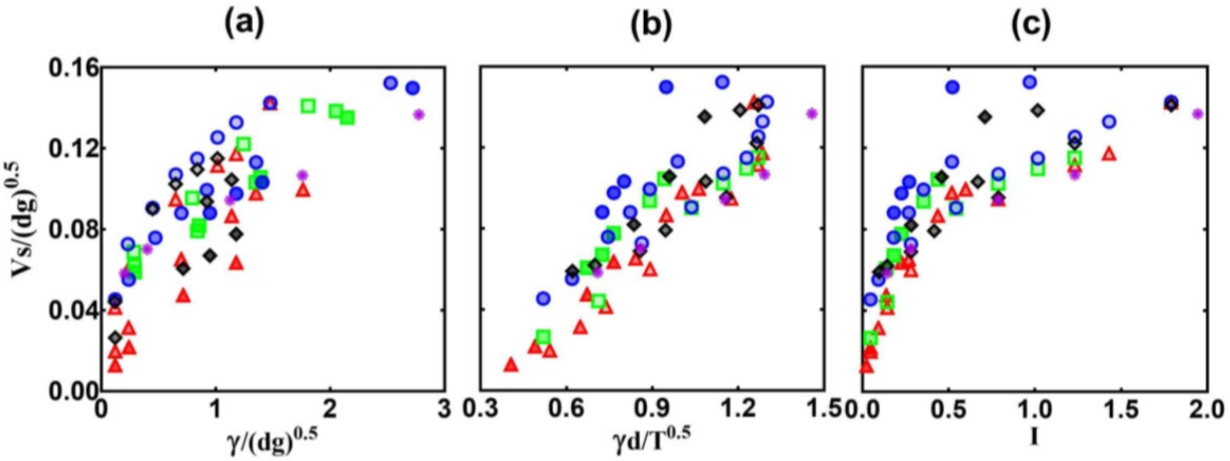

Figure 6.2: Dimensionless segregation velocity as a function of three forms of dimensionless shear rate. (a) the shearing velocity is dimensionless by dividing $\sqrt{gd}$. (b) the shearing velocity is dimensionless by dividing the square root of granular temperature $\sqrt{T}$. (c) the dimensionless shearing velocity is represented by the inertia number. Star symbol represents d = 3mm and P = 77.9Pa. Diamond symbols represent d = 6mm and P ranges from 77.9 to 701.1pa. For 9 mm particles, P range from 77.9 to 1558 Pa were tested. Circle represent size ratio $\bar{r} = 0.5$, square for $\bar{r} = 0.67$ and triangle for $\bar{r} = 0.75$. For each condition, lower transparency means higher pressure.

While traditional methods to plot the data were not able to show a clear trend, we are able to collapse all of the data (Figure 6.3). In Figure 6.3.a , three distinct curves show three different size ratios, but a clear trend is seen for all imposed pressures, shear rates, and bulk particle sizes (3, 6, and 9 mm). The fact that $I*\sqrt{\bar{T}}$ is able to capture the impact of all of these variables is strong evidence that both local velocity fluctuations and flow rheology need to be considered for dense phase size segregation. Moreover, in Figure 6.3.b, the data can be further collapsed (for all size ratios examined) by dividing the x axis by the projected area ratio of the particles ($\bar{r}^2$). This shows that instead of size ratio, the projected area is likely to be one of the control parameters for size segregation.

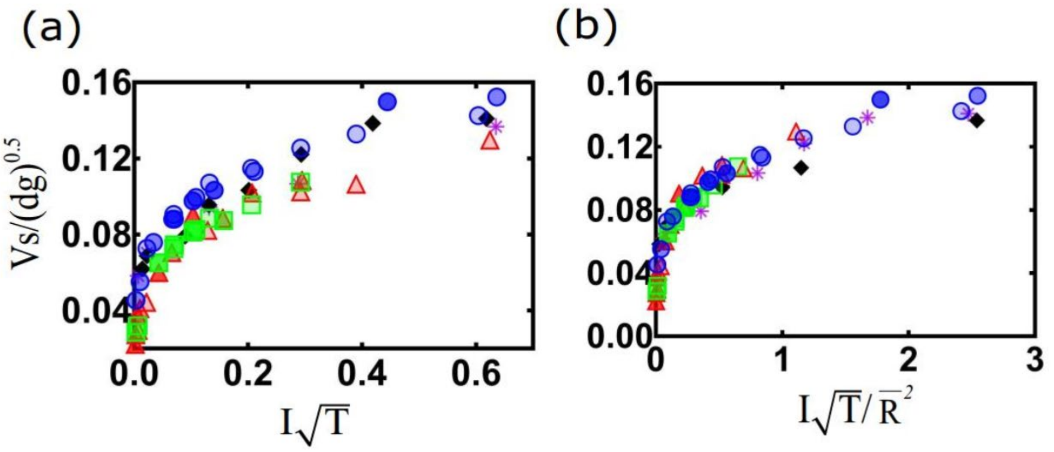

Figure 6.3: (a) Dimensionless segregation velocity as a function of inertia number multiplies by square root of granular temperature. (b) Dimensionless segregation velocity as a function of inertia number multiplies by square root of granular temperature and the inverse of size ratio square. **Star symbol represents d = 3mm and P = 77.9Pa. Diamond symbols represent d = 6mm and P ranges from 77.9 to 701.1pa. For 9 mm particles, P range from 77.9 to 1558 Pa were tested. Circle represent size ratio $\bar{r} = 0.5$, square for $\bar{r} = 0.67$ and triangle for $\bar{r} = 0.75$. For each condition, lower transparency means higher pressure.**

6.4 RESULTS

6.4.1 Granular Temperature T

In a shearing system, inter-particle collisions induce random particle velocities which are similar to the kinetic temperature of molecules. The magnitude of this velocity fluctuation is called the granular temperature T which is defined as:

$$T = \frac{1}{3} | < u^2 > + < v^2 > + < w^2 > | \tag{6-1}$$

where u, v, w are particle velocities on each direction.

Granular temperature, unlike in a molecular system, is a by-product of the flow and thus depends on the fluid mechanics[95]. GDR MiDi[8] reported the following scaling law for T under shearing cell configuration:

$$T \propto d\dot{\gamma}\sqrt{\frac{P}{\rho}} \tag{6-2}$$

Based on the equation, T depends on both the shear rate γ and the confining pressure P. We had a similar observation from our simulation; but the exact relation we got is different. Figure 6.4.(a) inserted shows our simulated result for granular temperate T as a function of shear rate γ. Since the majority of particles have the bigger diameter, the granular temperature T is measured based on the big particles; so, it only changes with bulk particle diameter not size ratio $\overline{r}$. Based on our result, we found that instead of a linear relationship, the granular temperature actually has a power dependence of the shear rate γ: $T \propto K\gamma^{1.5}$. As shown in Figure 6.4.(a), in the log-log plot, all lines have a slope of approximately 1.5. After comparing the value of constant K under different pressures and particle diameters, we propose a new granular temperature scaling law in a shearing cell as shown below:

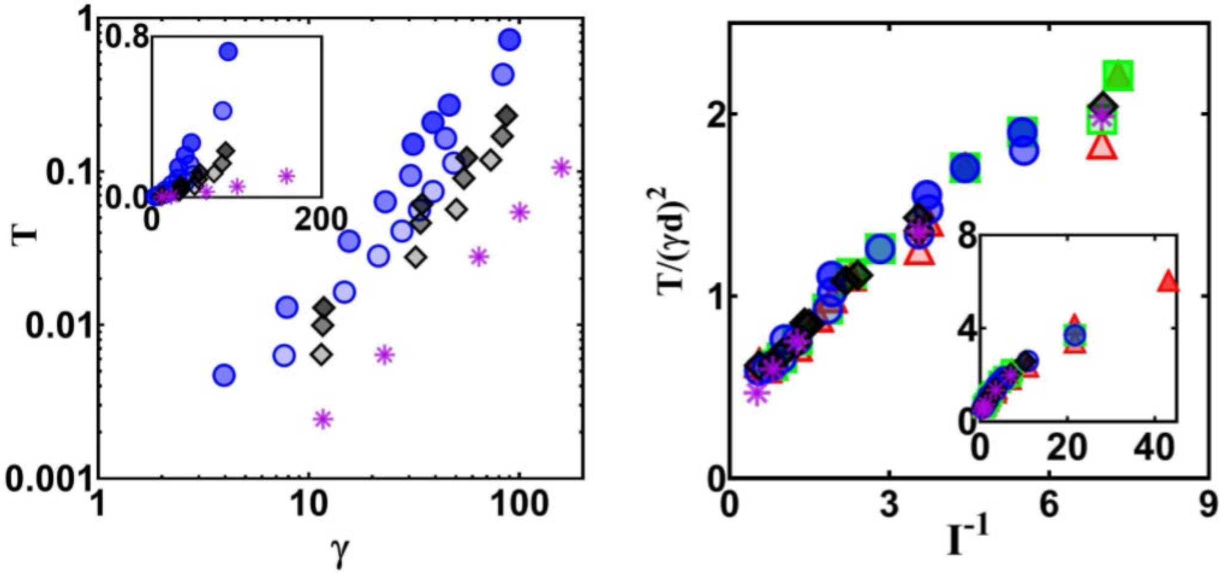

Figure 6.4: (a) Log-log scaled plot of granular temperature (m2/s2) as a function of shear rate (m/s) for size ratio ($\bar{r}=0.5$). The insert shows the same plot in linear scale. (b) Dimensionless granular temperature as a function of inverted inertia number (I^{-1}). The insert shows a broader range of I^{-1} while the big picture focus on I bigger than 0.1. Star symbol represents $d=3mm$ and $P=77.9Pa$. Diamond symbols represent $d=6mm$ and P ranges from 77.9 to $701.1pa$. For 9 mm particles, P range from 77.9 to 1558 Pa were tested. Circle represent size ratio $\bar{r}=0.5$, square for $\bar{r}=0.67$ and triangle for $\bar{r}=0.75$. For each condition, lower transparency means higher pressure.

$$T \propto (d\dot{\gamma})^{3/2}(\frac{P}{\rho})^{1/4} \tag{6-3}$$

This equation is able to capture the varies of value K pretty well under different pressure P and particle diameter d. Eq.(6-3) can be rearranged into a dimensionless form as

$$\frac{T}{(d\dot{\gamma}))^2} \propto \frac{1}{I} \tag{6-4}$$

where I is the inertia number defined as $I=\gamma d\sqrt{\frac{\rho}{P}}$ [8].

As shown in Figure 6.4. (b), this dimensionless form works reasonably well for inertia number bigger than 0.1; but a different behavior was observed for T under smaller inertia number (Figure 2.1(b) insert). A potential reason for this is flow mechanism changing caused by regime transition from intermediate flow regime to the quasi-static regime at low inertia number as mentioned in GDR MiDi[8].

6.4.2 Coordination Number Z

The coordination number Z is measured from the DEM simulation based on how many particles are contacting with the target particles at a time step. The measured Z is an averaged value over a period of time. Figure 6.5 plots the coordination number Z as a function of inertial number I for the bulk particles (9mm) and small tracer particles under each size ratio. Same as our previous founding and some other researches, Z vs. I has a power law behavior ($Z \sim I^{-a}$)[67,69,76] and based on our simulation, there are two regimes where a $\approx$ 0.3 and 1 for I values below and above 0.5 respectively.

We observed that at the same Inertia Number, Z value depends lightly on pressure (higher Z at higher P) which has not being reported before and the reason maybe that the higher granular temperature under higher pressure causes more random movement. However, this dependence is much smaller comparing to the impact of size ratio $\bar{r}$ so it isn't considered when fitting the data.

In general, the smaller the particle is, the smaller the value of Z is. To easily observe the impact of particle size, we also plotted the scaled Z in Figure 6.5; which is calculated as $Z_{scaled} = Z * (\frac{1}{\bar{r}})^2$. As it is shown in the figure, scaled Z overlaps with the big particle Z values. This means that Z is proportional to $\bar{r}^2$. This makes sense since the number of contacts should be proportional to the sphere surface area (Area $\sim r^2$)

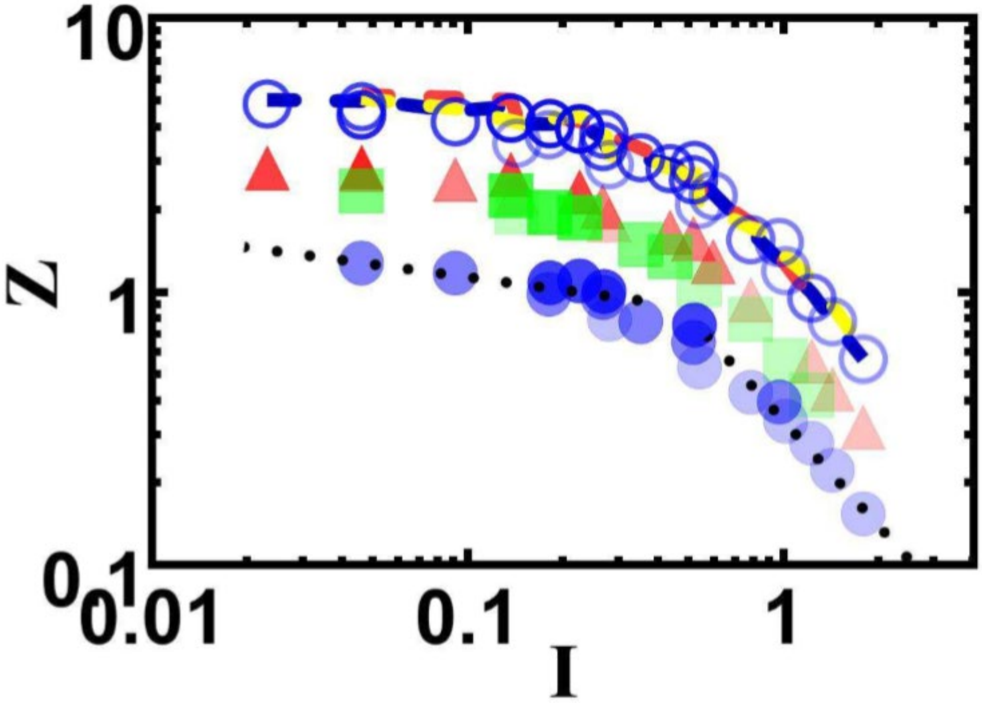

Figure 6.5: Coordination Number (Z) as a function of Inertia number (I). The hollow circle represents coordination number for bulk particles. For tracer particles, each different shape means one size ratio. Circle represent size ratio $\bar{r} = 0.5$, square for $\bar{r} = 0.67$ and triangle for $\bar{r} = 0.75$. For each condition, lower transparency means higher pressure. The colored dashed lines represent scaled coordination number Z_{scaled}. Data for coordination number can be fitted in to two power equations. $Z(I <= 0.5) \propto (1/\bar{r})^2 * I^{-0.295}$ and $Z(I > 0.5) \propto (1/\bar{r})^2 * I^{-1.164}$. The power law transition is indicated by a dotted line.

6.4.3 A segregation Model and Comparison with Simulation Results

In our model, we consider size segregation as a process which has two phases. The expansion/dilation phase and the segregation/percolation phase. For the expansion phase, we adopt an idea similar to that of Cooke and Bridgwater[86]. The core concept of this statistical argument is that we assume each bulk particle to be constrained within a cubic space. In order for segregation/percolation to even present as a possibility, this space must expand sufficiently to allow passage. In our approach, however, instead of assuming that the dimensionless expansion size necessary to satisfy this constraint is the diameter ratio of small to large particles r_s / r_b, we instead assume that it is controlled by the projected area ratio $(r_s / r_b)^2$. Thus, we assume that if the gap area in the box is greater than some critical value $R*^2$, the small particle would be able to progress though the gaps. Logically, $R*^2 \sim (r_s)^2$. Thus, the probability that the expansion is sufficient to allow a small particle of radius r_s to be able to pass though gaps with a distance R_g is

$$P({R_g}^2 > R*^2) = exp(-(R*/R)^2) \sim exp(-(r_s/R)^2)) \tag{6-5}$$

The actual gap size, R_g, that is present within a bed can be calculated based on the solid volume fraction ϕ. Using arguments set forth originally by Bagnold (and recapitulated by Hunt[96]), the dimensionless mean radial separation distance between particles (λ) can be related to the solid volume fraction ϕ via

$$\lambda = [(\phi_0/\phi)^{1/3} - 1] \tag{6-6}$$

where ϕ_0 is the maximum possible concentration. In this work, ϕ_0 is treated as equal to 0.74 (i.e., that of mono disperse close-packing) since the majority of our particles have the same size. Note that the mean radial separation distance λ is generally smaller than the actual hole diameter (Figure 6.6), as the structure of the bed (and hence the hole geometry) constantly changes during flow. As there is no easy way to measure the hole size, as a first approximation, we use a fixed constant C that it taken to be larger than 1 in order to relate λ to the hole size. In this work, C has been fit to have a value of 2.7. After considering both the influence of changing of hole size and the probability to fall through a hole, the percolation probability can be written as a function of the solid volume fraction in the way shown below and plotted in Figure 6.7

$$P(exp) = exp(-(\frac{\bar{r}}{(C*\phi_0/\phi)^{1/3}-1})^2)) \cdot (\frac{1}{\lambda})^2 \tag{6-7}$$

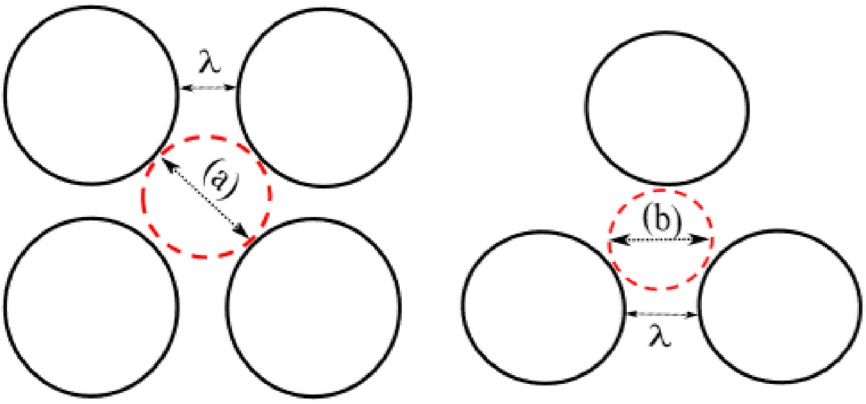

Figure 6.6: Two potential relationships between the particle mean radial separation distance λ and the actual hole size. The view is from above the shearing cell and each black circle represents one particle. The dotted line cycle represents the potential hole within the layer where upper layer particle can fall into. Since there are infinity ways particles can form holes within a layer, only the two simplest cases are presented here. The hole diameter $a=\sqrt{2}(\lambda+1)-1$ **and** $b=(\lambda+1)/\sqrt{3}$ **.**

As alluded to above, we argue that segregation requires more than simply creation of a properly sized hole. Thus, the actual probability of a small particle falling into (or segregating) into a particular gap cannot be predicted using Eq.(6-5). Instead, we need to take into consideration the fact that the small particle must ``explore'' the space above the hole and form an estimate of the rate at which this will occur.

Using an argument similar to that set forth in Liu[76], we think of the segregation velocity, v_s, as undergoing a ''frustrated free fall'' whereby drag forces between the segregating particle and its neighbors limit the rate at which a segregating particle may percolate through the bed. In contrast to the case of density segregation, where a particle may essentially create its own ``hole" do to gravitational force differences, in size segregation the particles must both encounter and traverse a hole in order for segregation to progress. In analogy to density segregation, the characteristic segregation velocity is that of free fall (i.e., $\sqrt{dg}$) where the falling distance d is taken to be the distance between granular layers (here given by the larger particle diameter). We further take the ratio of the consolidation time ($d[\rho / P]^{1/2}$) to the average inter-particle interaction time (i.e., the inverse of the particle interaction rate, which has been shown to be captured by $Z\gamma$, where Z is the coordination number and γ is the shear rate) to indicate fraction of time available for free-fall. Lastly, in accord with the observations of Campbell[97] with regard to the importance of granular temperature in size segregation, we further limit the free-fall to the effective rate at which a particle can explore its neighboring space. This latter effect is quantified via the ratio of the average fluctuational speed ($\sqrt{T}$) relative to the interlayer collision rate ($d\gamma$). Consolidating these effects, we argue that a proper characteristic velocity for size-based segregation can we written as

$$v_S \sim \sqrt{dg} Z\gamma d \sqrt{\frac{\rho}{P}} \frac{\sqrt{T}}{d\gamma} \sim \sqrt{dg} Z I \bar{T} \tag{6-8}$$

where $\bar{T}$ is the granular temperature made dimensionless with $(\gamma d)^2$.

Combining this expression (Eq.(6-8)) with the probability of percolating though (Eq.(6-7)), we can write the actual measurable dimensionless segregation velocity V_s as

$$Vs = \frac{v_s}{\sqrt{dg}} = A \cdot (\frac{1}{\lambda})^2 \cdot Z \cdot \sqrt{\bar{T}} \cdot I \cdot exp(-(\frac{1}{(C \cdot \bar{r} \cdot \phi_0/\phi)^{1/3} - 1})^2)) \qquad (6\text{-}9)$$

where A is a fitting parameter that accounts for the deviation of granular drag from Stoke's law taken to have a value of 2.6 in our case.

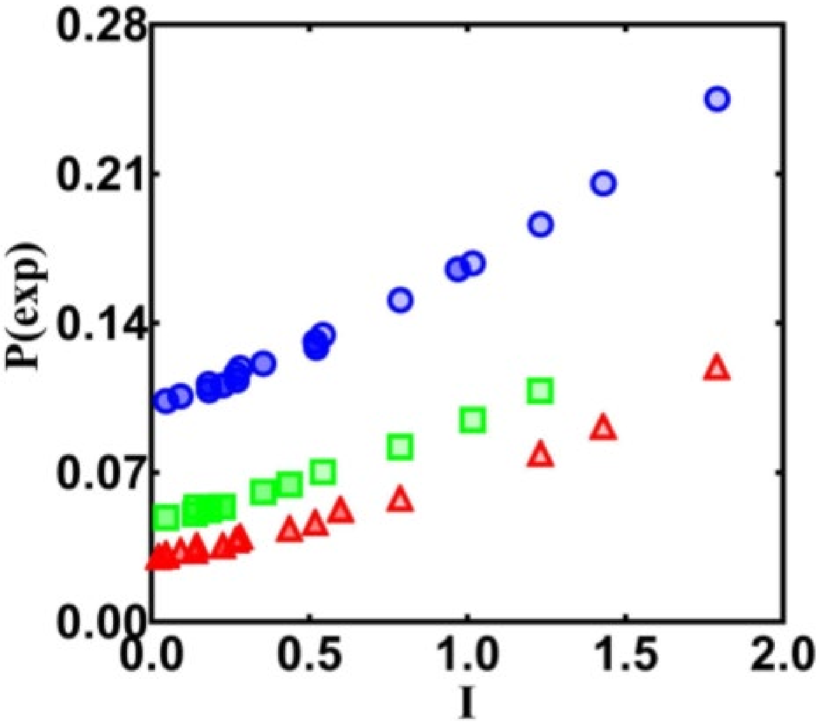

Figure 6.7: Probability for small particle to fall into holes as a function of inertia number. Circle represent size ratio $\bar{r}$ = 0.5, square for $\bar{r}$ = 0.67 and triangle for $\bar{r}$ = 0.75. For each condition P range from 77.9 to 1558 Pa were tested. Data points have lower transparency means higher pressure.

In Figure 6.8, we compared our proposed theory with the measured segregation velocity from simulation. Most points are able to fit into the $y = x$ diagonal line, thus the agreement between our theory and measured segregation velocity is remarkable.

Under all parameters, only $P(exp)$ and Z have a size ratio dependence and both of them depend on the project area $(r_s / r_b)^2$. This means that project area $(r_s / r_b)^2$, instead of the size ratio (r_s / r_b), is the size parameter impacting size segregation velocity; which conflicts with several previous researches stated[86,98].

In Figure 6.8, we compared our proposed theory with the measured segregation velocity from simulation. Most points are able to fit into the $y = x$ diagonal line, thus the agreement between our theory and measured segregation velocity is remarkable.

Under all parameters, only $P(exp)$ and Z have a size ratio dependence and both of them depend on the project area $(r_s / r_b)^2$. This means that project area $(r_s / r_b)^2$, instead of the size ratio (r_s / r_b), is the size parameter impacting size segregation velocity; which conflicts with several previous researches stated[86,98].

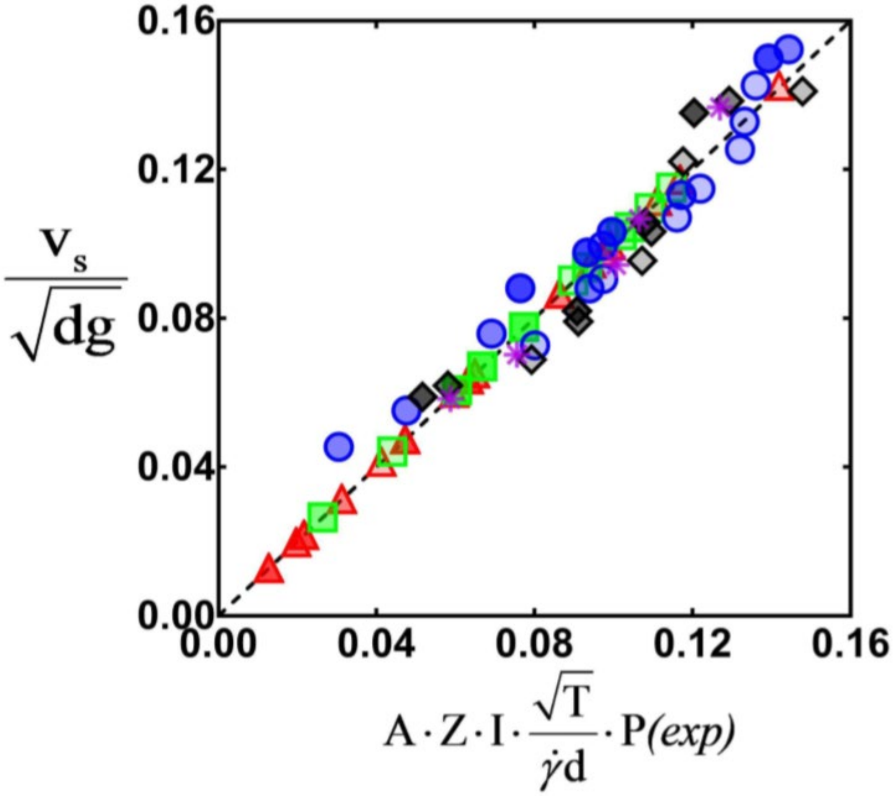

Figure 6.8: Measured dimensionless segregation velocity result versus proposed segregation velocity model. The dotted diagonal line represents y = x so points fall on the line means good fit between theory and measured value. Star symbol represents d = 3mm and P =77.9Pa. Diamond symbols represent d = 6mm and P ranges from 77.9 to 701.1pa. For 9 mm particles, P range from 77.9 to 1558 Pa were tested. Circle represent size ratio $\overline{r}$ = 0.5, square for $\overline{r}$ = 0.67 and triangle for $\overline{r}$ = 0.75. For each condition, lower transparency means higher pressure.

6.5 CONCLUSION

It is well known that for a given solids concentration, the probability of finding a hole that small particles can fall into is larger than the probability of finding a hole that a large particle can fall into. Hence, there is a tendency for particles to segregation with small particles at the bottom. However, none of the existed models is able to fitted into our simulated results very well. In this work, steady state DEM shear cell simulation was used to generate segregation velocity for tracer small particles in a medium of big particles. The simulation was performed over a range of particle size ratio, shear rate and pressure. Based on the simulation results and our previous researches in density segregation, we proposed a new size segregation model which combined flow rheology with kinetic sieving mechanism. This model is able to predict our simulated size segregation much better than existed models. Other than that, two important observation from our new theory and simulated results are: first, size segregation is not linearly dependent on shear rate. It also has a mild dependence on pressure which is usually ignored. Secondly, size segregation is influenced by the project area ratio of particles instead of just particle diameter ratio. The results of this work can help improve understanding of the influence of flow rheology to size segregation and help make better size models in the future. The next step of this work will be exploring size segregation for binary mixing and also size segregation under time dependence unsteady flows.

7.0 COHESIVE PARTICLE SEGREGATION AND GRANULAR RHEOLOGY

7.1 INTRODUCTION

Granular materials many commonly used in various industries, such as chemical, food and pharmaceutical. In operations, such as flotation, coating and granulation, instead of processing as dry materials, granular particles are frequently processed by adding a liquid phase. This has a significant effect on particle flow because when liquid exists between two contacting particles, a liquid bridge will be formed[58]. The cohesive capillary force caused by the liquid bridge can be much larger than the particle weight and thus leads to different flow behavior than dry particle processes. These flow modifications may be manifested as particle agglomeration and reduced segregation[99,100]. The fundamental impact of cohesion on particle flow behavior is lacking despite recent advances[45,99,101]. Because the economic impact of particle processing is significant[102], a deeper understanding of the effects of cohesive particles is needed.

While studies focusing on cohesive granular particles are scarce, in contrast, the study of dense phase granular rheology has gained traction recently[8,57,66]. Several papers have studied the connection between rheology and segregation[56,76] and the rheological behavior of cohesive granular materials[103]; however, no study, to our knowledge, has focused on how flow rheology is related to wet particle segregation.

In this paper, we focus on the segregation behavior of wet granular particles inside a shear cell. We show how flow rheology influences wet particle segregation and compare the results with dry particle segregation.

7.2 SIMULATION

7.2.1 Simulation set up and measurement method

In this work, we use a similar approach to that used in our previous study[76]. A discrete element method (DEM) code build in our lab was used to examine a wall-driving periodic plane shear cell. A schematic of the simulated 3D plane shear flow system is shown in Figure 7.1. Periodic boundaries were used in both the x and z directions. In the simulation, the majority of the particles had the same (light) density and had material property of acetate. Eight uniform heavy intruders, which had the properties of glass, were randomly placed in the system. The material properties used for the simulation are shown in Table 7.1. For the majority of cases, the density ratio between heavy and light particles ($\bar{\rho}$) was set to be 2 but in several cases, to study the impact of density, the heavy tracer particles' density was increased to 3900 kg/m^3 and thus $\bar{\rho}$ was equal to 3.

In order to obtain a nearly homogeneous shear flow (linear shear), fins made of wall particles were glued to both top and bottom walls, and a modified gravity force was applied only to the heavy tracer particles. Four different particle sizes (2,3,4 and 6 mm), with a 20 % particle size distribution to prevent crystallization, were tested. The reason we examine several background particle sizes is to test the impact of changes in the granular bond number (Bo_g) on the flow behavior. The Granular Bond number[58], which is commonly used to quantify the impact of adhesive binary interactions on mixing (Eq.(7-1)), increases when the size of the particles decreases; and for Bo_g number smaller than 0.5, the wet force is usually seen as having no impact on flow behavior[58].

$$Bo_g = \frac{F_c}{W} = \frac{2\pi R\gamma}{\frac{4}{3}\pi R^3 \rho g} = \frac{3\gamma}{2R^2 \rho g} \tag{7-1}$$

In the above equation, F_c is the maximum capillary force and W is the weight of the tracer particle. In this work, water is used as the liquid phase and thus the surface tension γ is set equal to 0.072 N/m. The shear rate range of this simulation is between 16 to 125 s^{-1} and the pressure is within the range of 17 to 160 pa. By doing so, the so called inertia number[8], which is defined below, has a range of values between 0.1 and 1.4.

$$I = \dot{\gamma} d_p \sqrt{\frac{\rho}{P}} \tag{7-2}$$

In Eq.(7-2), $\dot{\gamma}$ is the shear rate, P is the confining pressure, which depends on the wall mass, and d_p is the particle diameter.

In the simulation, the shear rate $\dot{\gamma}$ was calculated based on both the moving wall velocity and the distance between walls. The intruder particles' segregation velocity was calculated based on the slope of the average particle's movement plot as a function of time.

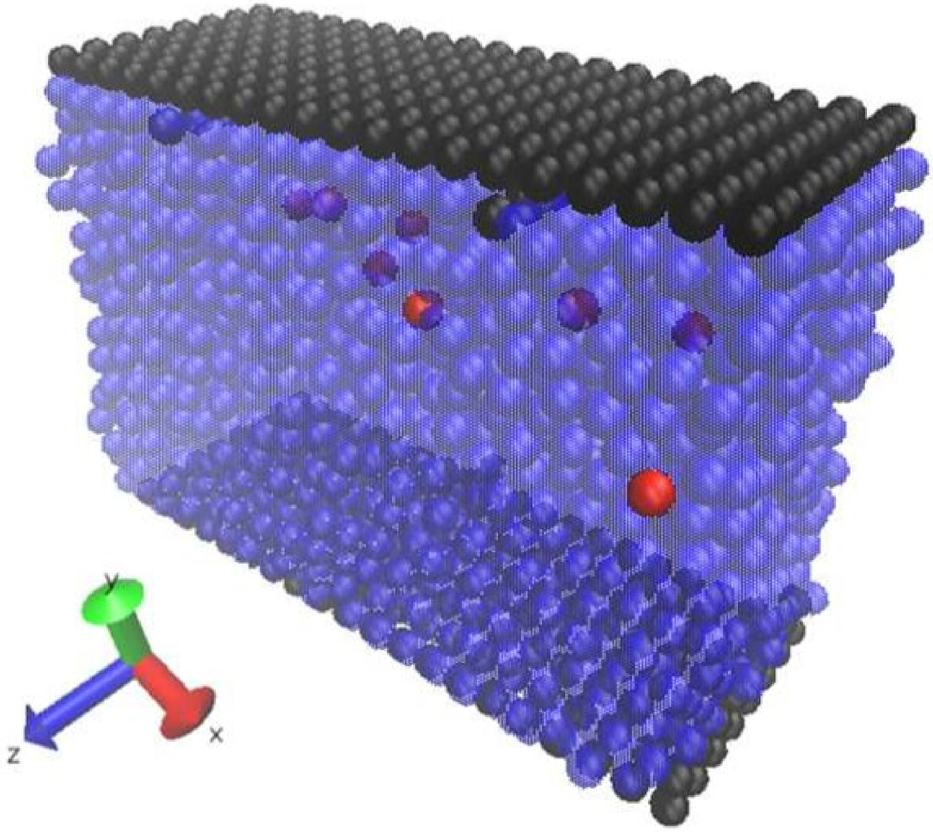

Figure 7.1: Schematic of the simulated plane shear geometry. The 3D flow is periodic in both the streamwise (x) and transverse (z) directions. Red (dark color) particles are heavy intruders and blue (light color) particles are lighter density particles. While the blue/light particles do not experience a gravitational force, the net force (self-weight minus an effective buoyant force) acts on the red/heavy intruders.

7.2.2 Simulation method

In the DEM code, the bulk flow of the material is captured via simultaneous integration of the interaction forces between individual pairs of particles[34,35]. When two wet particles contact each other, the liquid on their surface will form a liquid bridge and generate a cohesive and viscous force. In the sections below, we briefly review the model employed in this paper. A thorough description of the contact mechanics and particle dynamics can be found in previous papers from our group[101,104].

Table 7.1: Material properties used in the simulations

Parameter	Acetate	Glass
Young's modulus E (GPa)	2.90	68.95
Density ρ (kg/m^3)	1300.00	2700.00
Coefficient of friction μ	0.30	0.30
Poisson Ratio ν	0.43	0.33
Yield stress σ_y (MPa)	30.00	68.95

7.2.2.1 Normal Forces

The normal force is modeled as an elastic-plastic material using a similar method to that described in Thornton etc. [59,60]. The deformation of the particles α is mimicked via a computational "overlap" so that $\Delta\alpha = v_n dt$ represents the incremented changes in the overlap, where v_n is the velocity in the normal direction and dt is the time-step. $\Delta\alpha$ is positive for loading and negative for unloading. At the initial stages of loading, the normal force, F_n, is purely elastic and is given by

$$F_n^N = F_n^{N-1} + k_n * \Delta\alpha \tag{7-3}$$

where k_n, which equals to $2aE^*$, is the normal force constant from the Hertz theory[61]. In the above equation, a is the radius of the contact area and E^* is the representative Young's Modulus. In Eq.(7-3), F_n^{N-1} is the old normal force and F_n^N is the normal force at the current time-step.

Once the normal force exceeds a yield fore, F_y, a modified version of the contact force-displacement relationship based on Wu[40] is used. The normal force constant k_n of further loading is given by πYR^* and the deformation of the particles α equals to $\frac{\pi^2 Y^2 R}{4E^{*2}}$, where Y is the yield stress and R^* is the effective particle radius.

Once particles are in contact, the liquid on the particle surface will form a pendula bridge and both the capillary force F_c and the viscosity force on the normal direction F_{vn} are calculated using equations below.

$$F_c = -\pi\gamma R * (exp(A * S + B) + C) \tag{7-4}$$

$$F_{vn} = -6\pi R\mu v_n R/S \tag{7-5}$$

In the equations, S is the separation distance between the pair of particles, A, B and C are constants depend on a liquid bridge's volume, μ is the interstitial fluid's viscosity and R is the particle radius.

7.2.2.2 Tangential Forces

Walton and Braun derived the tangential (frictional) force[41]. For each time-step, the new tangential force acting at a particle-particle contact, F_t, is given as:

$$F_t^N = F_t^{N-1} - k_t\Delta s \tag{7-6}$$

where F_t^{N-1} is the old tangential force and $k_t\Delta s$ is the incremental change in the tangential force during the present time-step due to relative particle motion; i.e., Δs is the displacement during the present time-step; its expression is adapted from a vector form given by Walton[42]. When F_t is smaller than the sliding friction force ($\mu_f F_n$), the frictional stiffness k_t equals to $8G^* a$, where G^* is the shear modulus and a is the radius of the contact area[43].

Wet contact results in an additional viscosity force (F_{vt}) in the tangential direction with a similar manner to that of the normal direction (Eq.(7-7)). However, instead of v_n, this viscosity force depends on the relative tangential velocity of the spheres v_t.

$$F_{vt} = -6(\frac{8}{15} ln \frac{R}{S} + 0.9588)\pi R \mu v_t \qquad (7\text{-}7)$$

7.3 RESULTS

7.3.1 Dry granular flows

Dry granular flow has been frequently studied in recent years[8,57,67,76,81]. Based on dimensional analysis, a simple rheological theory (represented by Inertia number (Eq.(7-2))has been proposed and shown to be able to correctly predict many dense phase granular behaviors[65]. Our previous study found that this rheological theory can also lead to unique insights into particle segregation problems[76].

As shown in Figure 7.2, we found that when we plot the dimensionless segregation velocity ($\overline{V_s} = V_s / \sqrt{gd}$) as a function of inertia number (I), two regimes: a close to linearly increasing regime and a saturated regime. The inertia value separated those two regimes are always around 0.5, which corresponds roughly to a solids fraction of $\phi\sim0.52$. This is a strong evidence that flow rheology and dry granular particle segregation are related.

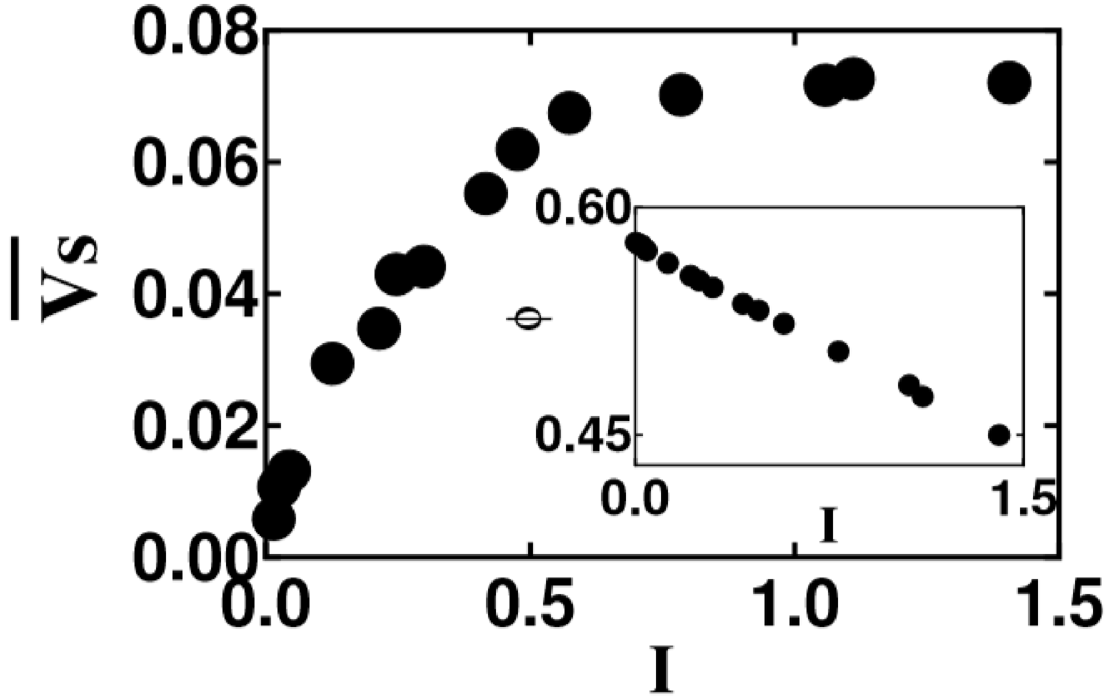

Figure 7.2: The dimensionless segregation velocity of dry granular material as a function of inertia number in a sheared cell system for $\bar{\rho} = 2$. The inserted sub-figure shows the linear relation between solid volume fraction and inertia number

Tripathi and Khakhar proposed that density segregation can be presented by a force balance equation: $0 = F_w - F_b + F_d$, in which F_w is the gravity force, F_b is the buoyancy force and F_d is the drag force[17]. Based on this force balance equation and an argument that the local shear rate around the tracer particles depends on both the coordination number and the global shear rate, we derived a new density segregation model in term of rheological parameters and the coordination number (z) as shown in equation below:

$$\overline{v_s} = \frac{v_s}{\sqrt{d_p g}} = \frac{z(\bar{\rho}-1)}{\beta\sqrt{\bar{\rho}}} I \tag{7-8}$$

In this equation, β is a fitting parameter and g is the gravitational acceleration. Since under high inertia number, the coordination number is proportional to I^{-1} as shown in Figure 7.3, the rate of segregation reaches a saturated value after this critical I value.

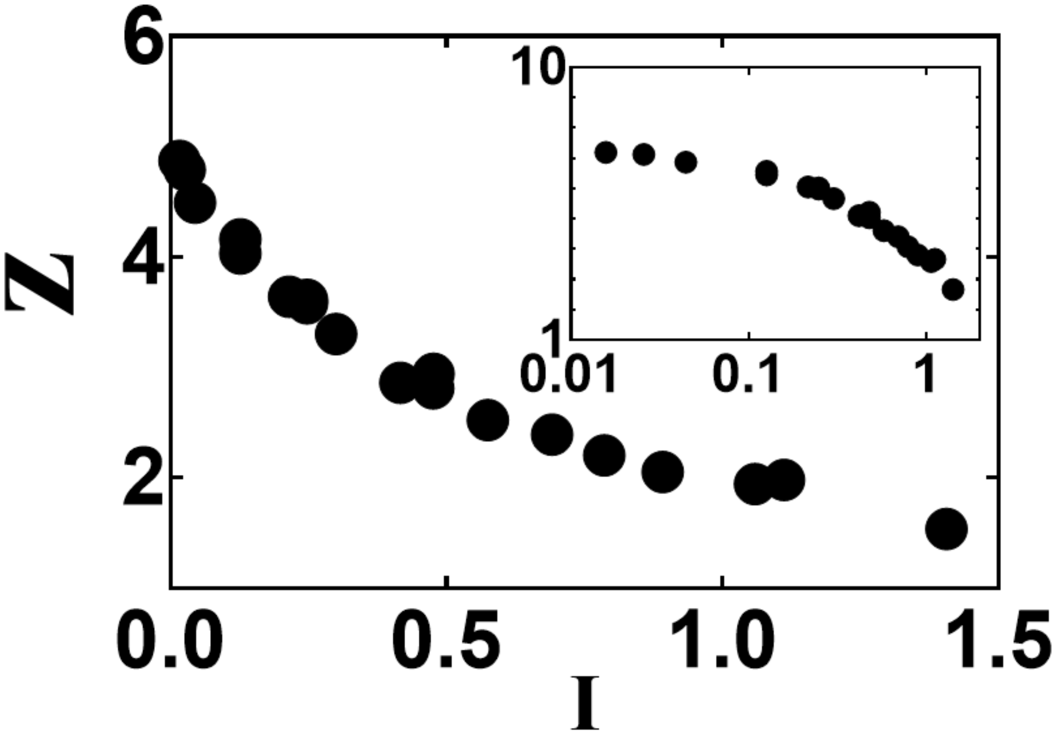

Figure 7.3: Coordination number as a function of Inertia number for dry granular material. The inserted figure shows the same plot in a log-log scale.

7.3.2 Wet granular flows

There is anecdotal evidence that wetting can slow down or even prevent segregation to happen; thus, one might expect that the segregation velocity for wet particles is slower than dry particles under the same condition, and at the same time, that the impact of wetting is larger for smaller particles (bigger granular bond number Bo_g). Surprisingly, when we plot the dimensionless segregation velocity as a function of inertia number (Figure 7.4) for wet granular materials, we find that for all four different diameter cases tested, the data was able to collapse with the reference dry granular data sets. This indicates that under the same rheological condition, the wet granular flow has the exact same segregation behavior as the dry granular flow; which is contrary to conventional wisdom. Figure 7.4 also suggests that wet segregation has the same mechanism as dry segregation.

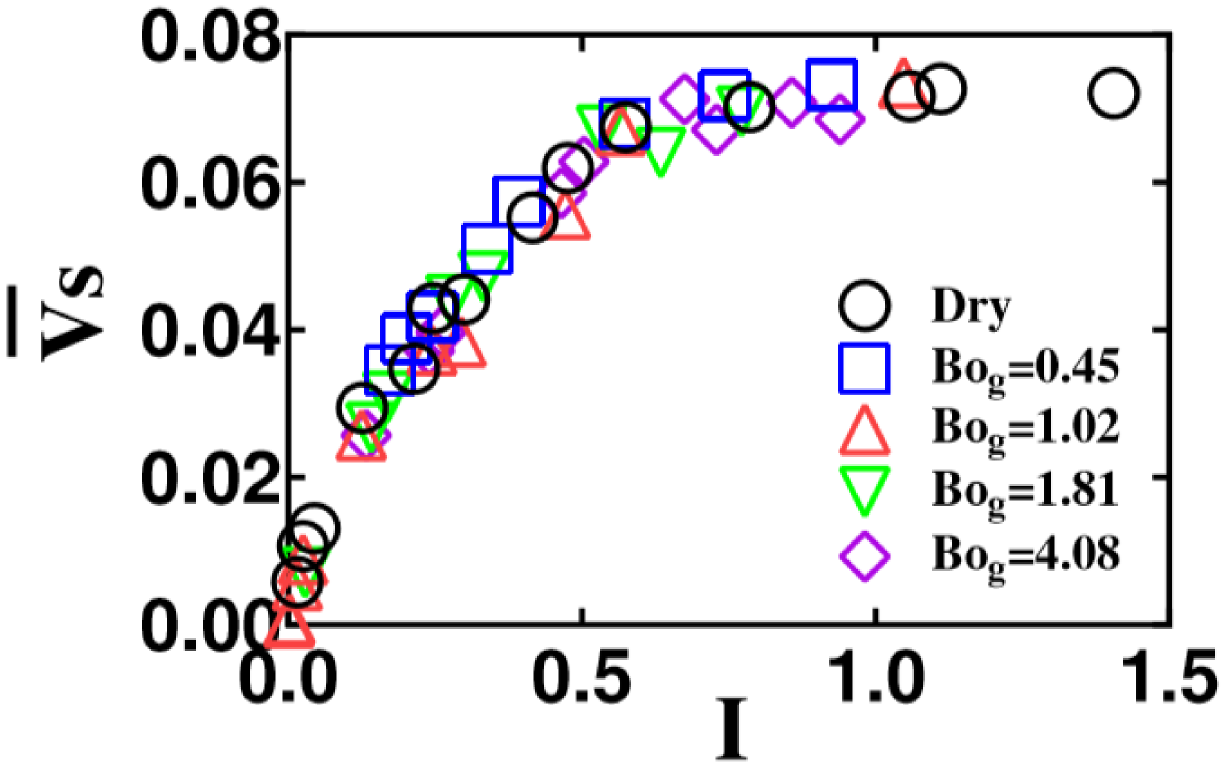

Figure 7.4: Dimensionless wet segregation velocity as a function of inertia number for particle diameter 6mm (Bo_g = 0.45), 4mm (Bo_g = 1.02), 3mm (Bo_g = 1.81) and 2mm (Bo_g = 4.08). Dry segregation is also plotted as a reference.

When we plot the solid volume fraction as a function of inertia number (Figure 7.5.(a)), we find that, although the relationship is still linear, the solid volume fraction for larger granular bond number cases are always smaller. In a similar vein, Figure 7.5.(b) shows that under the same inertia number, higher granular bond number conditions always have higher coordination number, z. This observation means that our previously proposed dry granular segregation model (Eq.(7-8)) won't work for wet granular flows without adjustment, but it also portends the required modification.

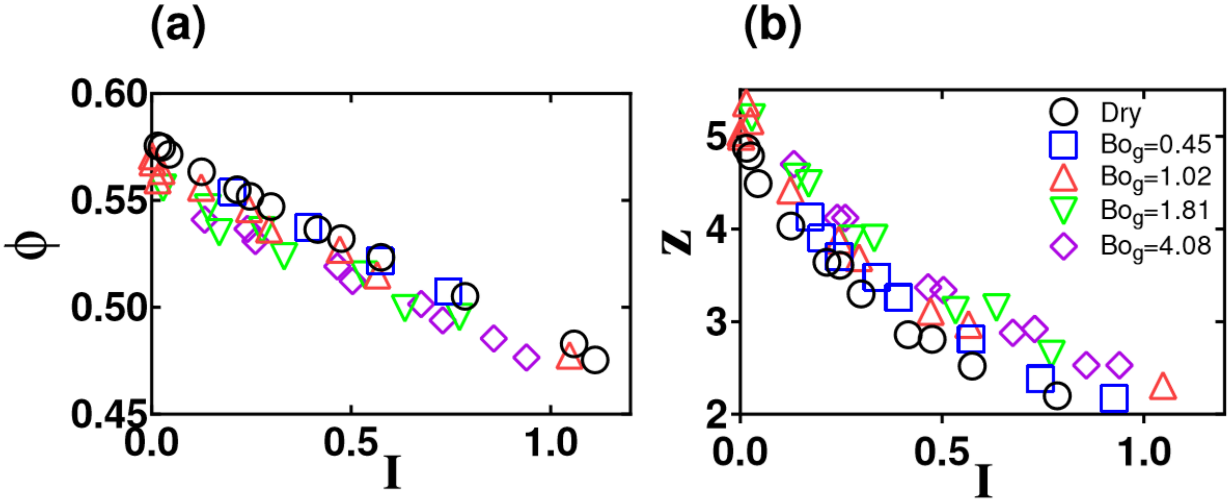

Figure 7.5: (a) Solid volume fraction as a function of inertia number for wet cases and the reference dry case. (b) Coordination number as a function of inertia number for wet cases and the reference dry case. Four wet cases, particle diameter 6mm ($Bo_g = 0.45$), 4m m ($Bo_g = 1.02$), 3mm ($Bo_g = 1.81$) and 2mm ($Bo_g = 4.08$) are shown in figures.

To modify our segregation model, we treat the forces caused by wetting conditions as a drag force and write a new force balance equation for density segregation in wet granular flow as $0 = F_w - F_b - F_d - F_{dw}$. In this equation, F_{dw} is the drag force caused by wetting. Taking both drag forces to have a Stokesian form, they both can be written as $F_d = \beta\pi\eta d_p v_s$, where β is a fitting parameter. Thus, if we rearrange the equation and use the same argument as our dry flow theory, the segregation velocity model can be written as

$$\overline{v_s} = \frac{v_s}{\sqrt{d_p g}} = \frac{z(\bar{\rho}-1)}{(\beta_{dry}+\beta_{wet})\sqrt{\bar{\rho}}} I \tag{7-9}$$

In above equation, both β_{dry} and β_{wet} are fitting parameters. Eq. (7-9) can explain why wet segregation vs. rheology figure has the same shape as dry segregation.

In order to further explain the behavior, we see in Figure 7.4, we need to look at the problem from another angle. In our previously proposed dry segregation theory, we stated that particle collision energy can be transferred to kinetic energy and thus, the higher the interparticle interaction rate (i.e., $Z\gamma$), the faster a particle may segregate. However, under wet conditions, not all contacts can be viewed as collisions. The cohesive forces between particles will actually attract particles together and decrease particles' kinetic energy. Thus, in order to calculate the effective interaction rate, we propose an adjusted coordination number (z_{adj}) as shown below:

$$\overline{v_s} = \frac{v_s}{\sqrt{d_p g}} = \frac{z(\bar{\rho}-1)}{(\beta_{dry}+\beta_{wet})\sqrt{\bar{\rho}}} I \tag{7-10}$$

In this equation, F_c is the capillary force, which can be seen as equal to $\pi\gamma d_p$[45], F_z is the collision force, which should be proportional to the confining pressure and thus, can be seen as equal to $\alpha\pi d_p^2 P/4$. Here α is a fitting parameter with a value of 10. In Figure 7.6, we present the adjusted coordination number for wet conditions compared with the coordination for the dry case. As can be seen, the adjusted coordination numbers collapse with the dry coordination number for every granular bond number. In another word, under the same inertia number, the adjusted coordination number for different wet conditions will always have the same value as the dry reference case. However, this can be seen more as a flow regime constraint as opposed to a modeling failure. Thus, after switching the parameter for z to z_{adj}, our previous proposed segregation model (Eq.(7-8)) can be used to predict wet segregation velocity as well.

One thing worth pointing out is that based on our simulation, if the value of $\frac{F_c}{F_z}$ is bigger than ~ 0.2, the simulation will have trouble keeping the shearing profile linear because of the strong attraction force between particles. As a result, if the value of $\frac{F_c}{F_z}$ is bigger than ~ 0.2 both the adjusted coordination number (z_{adj}) and dimensionless segregation velocity ($\overline{v_s}$) will not collapse with the dry case. Thus, the ratio $\frac{F_c}{F_z}$ can be used as an indicator of when wet flow/segregation behaves dramatically different from dry.

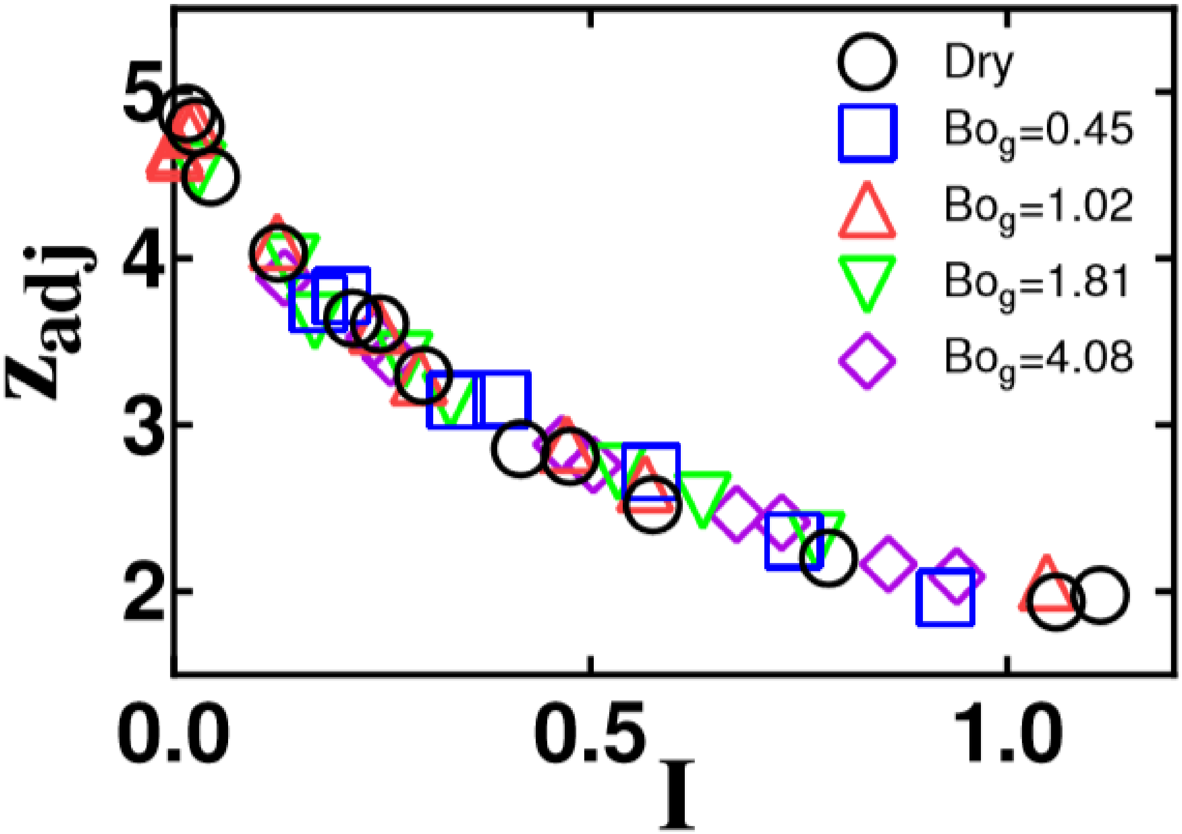

Figure 7.6: Adjusted coordination number (Eq. 6) as a function of inertia number for four different diameter wet conditions (6mm, 4mm, 3mm and 2mm) and the reference dry condition.

8.0 AN EXPERIMENTAL STUDY OF CYLINDRICAL PARTICLE'S EFFECTIVE SIZE IN A ROTATING TUMBLER

8.1 INTRODUCTION

A granular system is a collection of individual solid particles. The overall granular behavior is controlled by the contact forces between the individual particles within the system. Particle segregation, one of the unique problems existed in granular systems, is the process of spontaneous separation when particles with different properties particles (size, density, shape, surface property etc.) are combined and agitated. While there is a wealth of research in a variety of different flow vessels devoted to studying size segregation[27,77,91,92] and density segregation[17,52,93], and there is a relatively new trend of studying the underlying physics of granular flows[66,105,106], shape segregation has received relatively spare attention until fairly recently[107]. This is due, in part, to the fact that the physics for irregularly shaped particles in dense flows are more complicated and particle shape-based simulations are harder to perform than those with idealized spherical particles. Despite the fact that there are only a few studies that investigate shape segregation, the phenomenon is industrially common. For example, pharmaceutical tablets, coal and food grain processing all involve non-spherical particles and it is known that particle shape has a significant impact on the flow behavior in these industries.

A number of recent studies have investigated the behavior differences between the flow of spherical and non-spherical particles. Cleary[108] found that in a simple shear flow non-circular particles have a higher granular temperature and lower solid fraction than corresponding spherical particles due to particle spin. Yamane et al.[109] found that non spherical particles have a higher maximum velocity and thinner active layer than spherical particles in a rotating cylinder. Mandal et al.[110] studied the effect of particle aspect ratio on the rheology of the flow in a rotating cylinder and found that the dynamic angle of repose and apparent viscosity increases with particle aspect ratio while velocity and shear profile are comparably similar between no spherical and spherical particles. Rasouli et al.[111] used the multiple radioactive particle tracking (RPT) technique to compare the flow behavior of cylindrical and spherical particles inside a rotating drum. They studied the general velocity profile of cylindrical particles and proposed an effective particle size model for cylindrical particles. This model represents one of several that we test in this study.

The rotating drum or tumbler partially filled with granular material has been a common experimental geometry to study granular surface flows[21,93]. Increasing the rotational speed of the tumbler has been known to change flow regimes (slipping to rolling to centrifuging) [112,113]. In industrial operations, the rolling regime, in which a shallow layer of particles flows within the active layer (free surface flow) and the remaining material rotates as a solid (passive layer), plays an important role in a wide range of processes such as mixing, coating and drying.

In this work, we take an initial step towards building an understanding of how shape segregation works by studying the behavior of cylindrical particles within a medium of spherical particles in a quasi-2D rotating tumbler operating in the rolling regime.

8.2 EXPERIMENT

Our experiment setup is shown in Figure 8.1. The quasi-2D tumbler has a radius of 0.13 m and depth of 26.3 mm. Experiments are run with the device half-filled with spheres as well as 30 tracer cylinders, which represents a negligible number fraction inside the system and are initially set on top of the free surface. The tracer particles were dyed using red ink to make them more distinguishable. All particles have properties of steel ($\rho = 7900kg / m^3$). Three different sizes of steel balls are used (3, 4.5 and 6.35 mm) and multiple type of cylinders/disks which have different lengths and diameters are tested. We define disks as cylinders whose diameters are bigger than their lengths. The shape properties of cylinders used in this experiment are given in

Table **8.1** in which #7 and #8 are considered as disks while the rest are a more traditional elongated shape of cylinder. All the particles we use in this study are also shown in Figure 8.2. To compare with size segregation, which is well studied and usually tested using different sizes of sphere particles, we also run several trials of experiments using spheres as tracer particles. Those experiments are set as reference and were compared with cylinder results later.

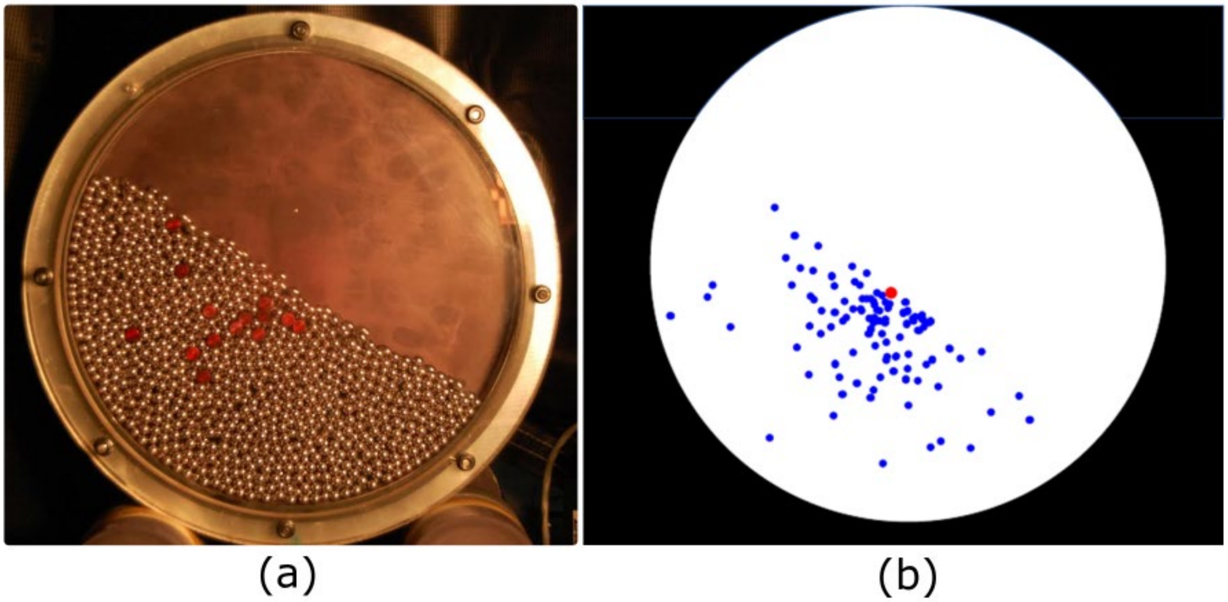

(a) (b)

Figure 8.1: (a) Experimental Results for #7 tracer disks (as shown in Table 4.1) inside 6.35 mm spheres at 1.7 RPM. (b) Analyzed results for the same experiment condition. Each blue dot indicates a tagged tracer particles' position and the red dot is used to indicate the center of the tumbler

Table 8.1: Cylinder Shape Factors

Cylinder #	1	2	3	4	5	6	7	8
Diameter(mm)	3	4.5	6	3.98	3.98	3.98	7.14	7.14
Length (mm)	6.2	6.2	6.2	4.8	7.0	9.4	2.61	3.91

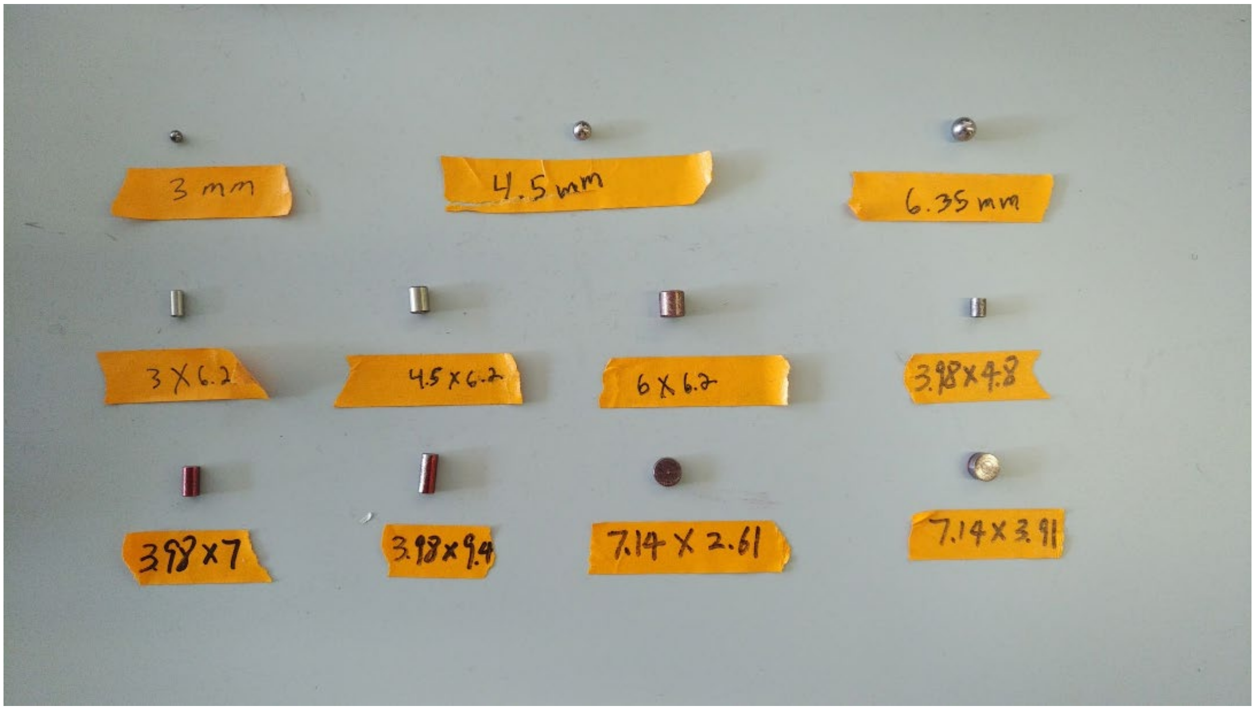

Figure 8.2: All particles used in the study

A computer-controlled stepper motor is used to control the rotation rate of the tumbler. Experiments are carried out for five different rotating rate (ω =1.7, 3.5, 5.2, 7.0 and 8.6 RPM) and the flow resulted in the rolling regime under each condition. Images of the rotating tumbler are taken with a Nikon D200 digital camera once the flow becomes steady. A halogen light is used to increase brightness while taking pictures. The steady state pictures are analyzed using image analysis software (GIMP). For each experimental condition, the position of the tracer particles was tagged for each picture (which is taken no more frequently than once per 1/4 rotation) until 100 tracer particles' positions are recorded. An analyzed picture is shown in Figure 8.1.b. The tracer particles' average distance to the tumbler center and the distance variance are calculated for each experimental condition. Generally speaking, the shorter the average distance to the center, the higher the tending of the material to exhibit inward segregation. Additionally, the higher the variance, the more mixed the system is. This method of qualifying segregation is similar to that used by Felix et al. for their size segregation study[114].

Later, in order to examine the impact of the side walls, we performed a set of experiments with disks in spheres in a 3-D cylinder. The cylinder has a diameter of 15 cm and length of 8 cm. The experiment was carried out at the rotation rate of 3 RPM. We took pictures from the top of the cylinder to observe the disks' behavior while in the free surface flow without the influence of wall effect.

8.3 RESULTS AND DISCUSSION

There are multiply ways to quantitatively represent a cylinder as a comparably sized sphere. In this section, we summarize the most commonly used methods and categorize them into three classes (1-D, 2-D and 3-D) and present a new way to quantify a cylinder's behavior when they are among spheres. We quantify the efficacy of those definitions by comparing the cylindrical particles' average distance to the center (Dc) of the tumbler to the location that we obtain using differing sized spheres as tracer particles. If our results are able to collapse onto a single curve, we consider the method able to correctly predict a cylinder particle's effective size. In the paragraphs below, we discuss the three classes of category, one by one.

We define methods in the 1-D class as those that use a one-dimensional length scale to predict the cylinders' size behavior. Two types of 1-D methods are shown here. "1-D short" uses the shortest length of the cylinder (either the diameter or the length depending on the shape) to predict the cylinder's effective size, while "1-D average" uses the average value between the length and diameter of the cylinder, i.e., (1-D $_{Average} = (Length + Diameter)/2$). In Figure 8.3

(a) and (b), we show the 1-D short results for the lowest (1.7) and highest (8.6) RPM that we tested. Although the exact values are different, both cases show the same trend. The majority of the cylinder results are able to align with the size segregation sphere results (shown as stars) while disks (shown as hexagons) are closer to the tumbler edge than expected. This suggests that, when quantifying using the 1-D short method, disks predicted effective sphere sizes are smaller than they should be. Nevertheless, it is worth pointing out that when comparing sub figure (a) with (b), figure (a)'s data is more scattered. When the x axis has the same value, a higher aspect ratio ($Length / Diameter$) cylinder has a higher Dc value in Figure 8.3.(a) but not in Figure 8.3.(b). This can be understood due to the fact that cylindrical particles tend to spin within the flow at a lower RPM (broader particle orientation probability distribution), thus, they exhibit a larger effective size than the case when the majority of particles align with the flow (as they do at higher RPM).

Despite the differences, Figures (a) and (b), in general, display the same trend. Thus, for the remainder of this paper we only show the average Dc value for all 5 of the RPMs that we tested. In this way, we can reduce the impact of experimental noise/error on our comparison. The R-squared values of all cylinders (R_c^2) and disks data points (R_c^2) to the reference (shown as stars) are calculated and show for each method.

Figure 8.3. (c) shows the average results for 1-D short. It shows the same trend as sub figure (a) and (b). We determine the Dc value for small spheres in big spheres mixture and display it as the star symbol at x axis value equals to 1. For any distance to center (Dc) value smaller than the pure mixed case (i.e., for smaller sphere tracers), we consider as inward segregation and they are indicated as the shaded region of the figure.

Figure 8.3. (d) shows the 1-D average results. As shown in the figure, for this measure, disks (hexagons) size are correctly predicted (collapse with the reference curve shown by stars); however, all cylinder values are lower than the reference values. This means that when using 1-D average method to calculate the effective particle size, the calculated scale is bigger than the cylinder's actual effective size.

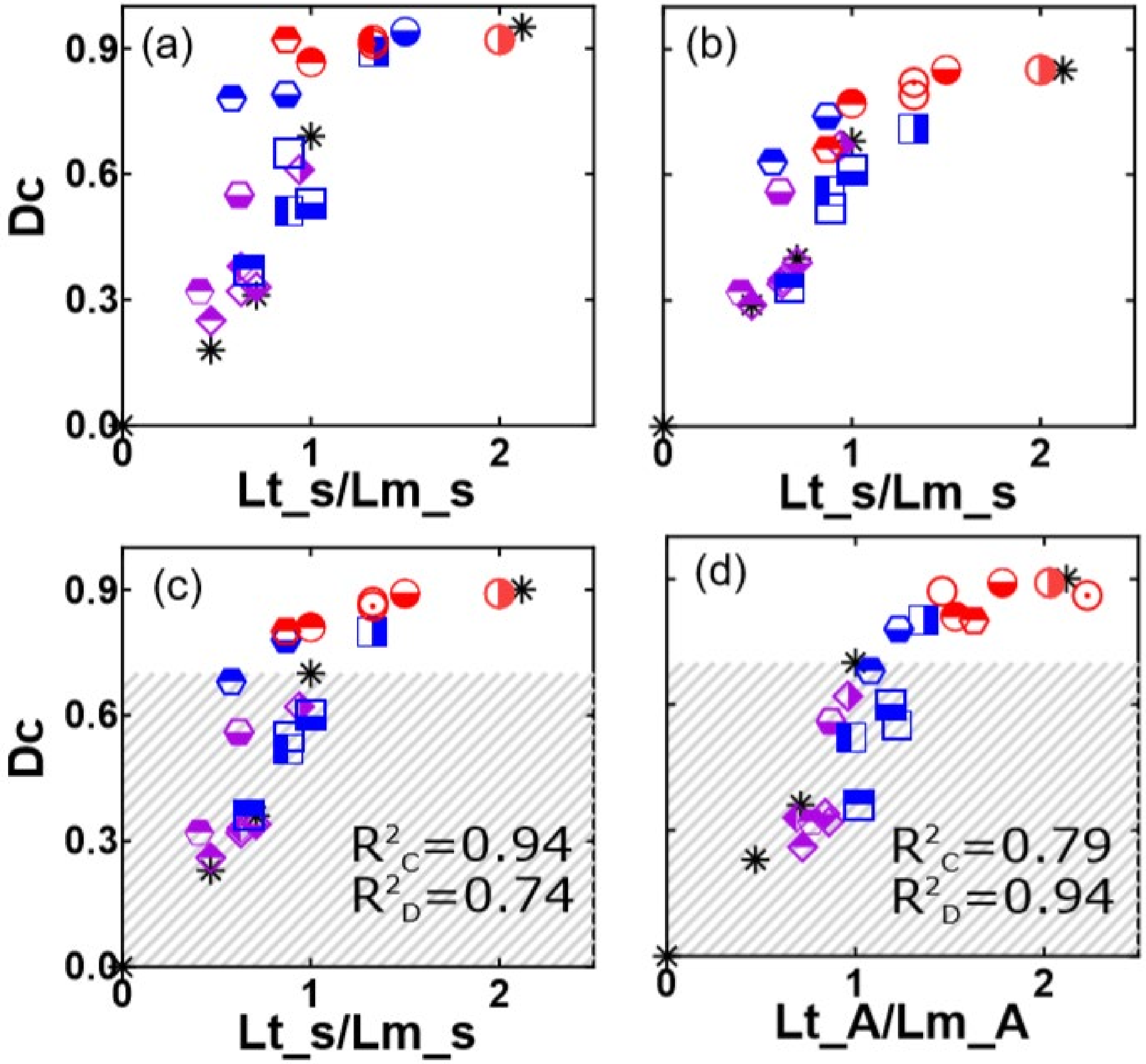

Figure 8.3: Average distance to the center vs. area scale ratio between tracers (cylinders) and the bulk materials (sphere). (a) shows the 1-D short plot under 1.7 RPM, (b) shows the 1-D short plot under 8.6 RPM, (c) shows the 1-D short plot for the average results for all five RPM and (d) shows the average 1-D Average results. In every figure, circle(red) represents 3 mm sphere, square(blue) for 4.5 mm sphere, diamond(purple) for 6.35 mm spheres, hexagons for tracer disk results and stars for sphere-sphere size segregation results. Each different fill means one-cylinder type. For disks (shown as hexagons), top filled is for #7 in table 1 and bottom filled for #8. For cylinders (shown in different shapes depends on the spheres media), #1 is top filled, #2 is bottom filled, #3 is right part filled, #4 is left part filled, #5 is an empty symbol and #6 has a dot inside the symbol

We also plot the results in 2-D area scales. The sphere's 2-D area scale is its projected area, but for cylinders, there are two ways to describe its projected area. If the majority of the cylinders are oriented in the flow direction, the proper area scale would be their largest projected area, thus $A_l = length * diameter$. On the other hand, if the majority of cylinders are freely rotating within the flow, it will exhibit a different projected area than the typical long area. In Figure 8.4, we show how we define particle's effective *rotating* length.

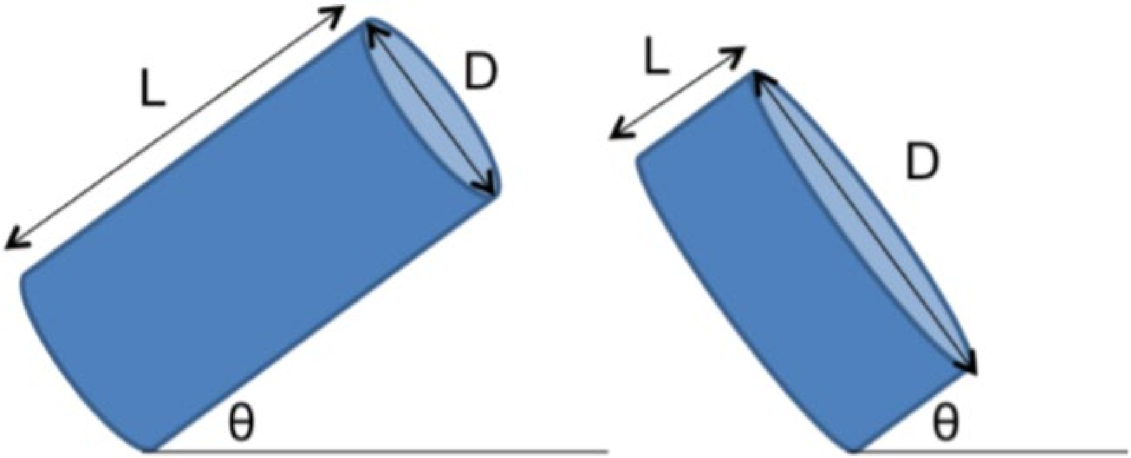

Figure 8.4: Defined shape parameters in both cylinder and disk particles.

The average length ($\overline{L}$) of a spinning cylinder can be described as

$$\bar{L} = \frac{\int_0^{\pi/2}[Diameter\cdot sin(\theta)+Length\cdot cos(\theta)]d\theta}{\pi/2} = \frac{Length+Diameter}{\pi/2} \qquad (7\text{-}11)$$

Therefore, the spinning area scale can be written as $A_s = \overline{L} * D$. The lay-down plot is shown in Figure 8.5.(a) and the spinning plot is shown in Figure 8.5.(b). As both figures show, the cylinder data sets are consistently lower than the sphere data set; but the difference is more obvious when using the spinning area to quantify the shape of the cylinders. As in Figure

8.3.(d), a lower than reference value means that by using the area to quantify the cylinders' behavior, the calculated value is bigger than the actual cylinder's effective sphere size. Although the cylinder results are lower than expected, Figure 8.5.(a) shows that the 2D lay-down method reasonably predicts the disks (hexagon) effective sphere size.

Figure 8.5.(c) shows the 3-D volume method, in which the volume of the cylinder is compared with the volume of spheres directly. As the figure shows, by treat cylinders as the same volume spheres, the size effect of cylinders is overly exaggerated.

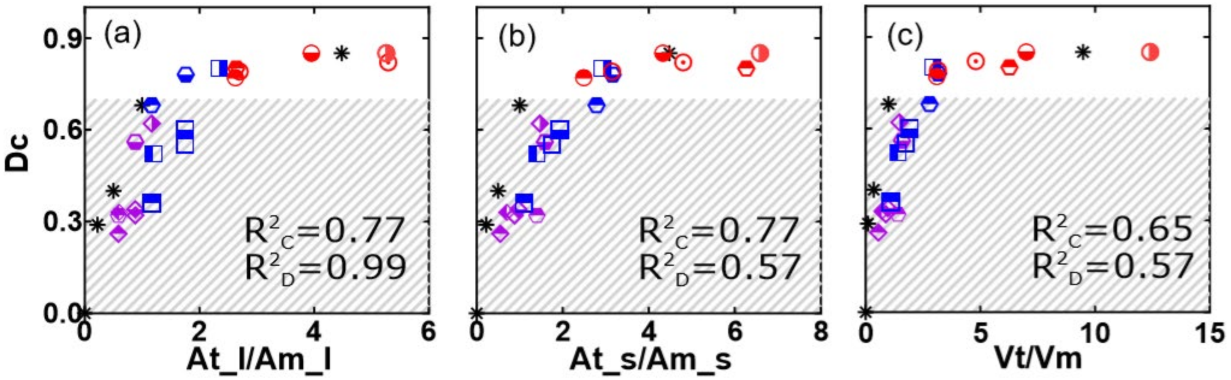

Figure 8.5: Average distance to the center vs. Area ratio between tracers (cylinders) and the bulk materials (sphere). (a) shows the 2-D lay down plot (b) shows the 2-D spinning plot and (c) shows the 3-D volume plot. In every figure, circle(red) represents 3 mm sphere, square(blue) for 4.5 mm sphere, diamond(purple) for 6.35 mm spheres, hexagons for tracer disk results and stars for sphere-sphere size segregation results. Each different fill means one-cylinder type. For disks (shown as hexagons), top filled is for #7 in table 1 and bottom filled for #8. For cylinders (shown in different shapes depends on the spheres media), #1 is top filled, #2 is bottom filled, #3 is right part filled, #4 is left part filled, #5 is an empty symbol and #6 has a dot inside the symbol

Of all the methods we tested to calculate the effective particle sizes, 1-D short is the best at predicting an elongated cylinder's effective size, while 2-D lay-down is better at predict the disk's effective size. This suggests that disks and elongated cylinders behave differently in an active flow and thus, when researching cylindrical particles' flow behavior, most researchers focus on aspect ratios bigger than 1 to avoid the inconsistency issue[107,110]. In this work, in an attempt to solve this problem, we propose a new method which is able to predict the effective size for both disks and elongated cylinders, which we call the 2-D flowing-area method. We argue that if the majority of cylinders become oriented in the flow, the number of collisions the tracer cylinder particles are going to have is proportional to its edge area ($\pi * (Diameter / 2)^2$). Disks, on the other hand, behave differently. As shown in Figure 8.1 and Figure 8.6, based on our experiments, tracer disk particles are more likely to roll down the free surface vertically rather than lay flat and align with the flow. To make this finding more convincing, we analyzed 44 pictures taken from the top of the 3-D cylinder and we found that statistically, the chance of seeing a tracer particle rolling down the free surface is 70 % higher than seeing it lying flat above the flow. At the same time, once disks segregated into the flow vertically, they would likely stay in that orientation within the flow due to steric constraints that prohibit further reorientation. As a result, the effective flowing area for disks has the shape of a rectangle ($A_f = Diameter * length$).

For both cylinders and disks, this flowing area can be compared with the bulk particles' surface area directly to predict an effective particle size. As Figure 8.7 shows, by using flowing area to indicate cylinders/disks' effective size, we are able to collapse all the shape results with the reference data set very well. Thus, we can say that the flowing area is a more accurate and general way to calculate the effective particle sizes for elongated cylinders/disks than the other methods mentioned earlier.

Figure 8.6: Experimental results for #7 tracer disks (as shown in Table 1) with 4.5 mm bulk spheres inside a 3-D cylinder container running at 3 RPM.

This flowing area argument is similar to the effective projected area proposed by Guo et al.[115]. Our previous density and size segregation studies have also indicated that the number of collisions is one of the most important factors in determining the segregation velocity[76,116]. Moreover, based on our size study, in the case of spherical particles, the number of collisions (or the so-called coordination number in our case) is proportional to the particle's surface area. Thus, it makes sense that the average tracer particle's distance to center, which itself is a function of the segregation velocity, depends on the flowing surface area of that cylinder/disk.

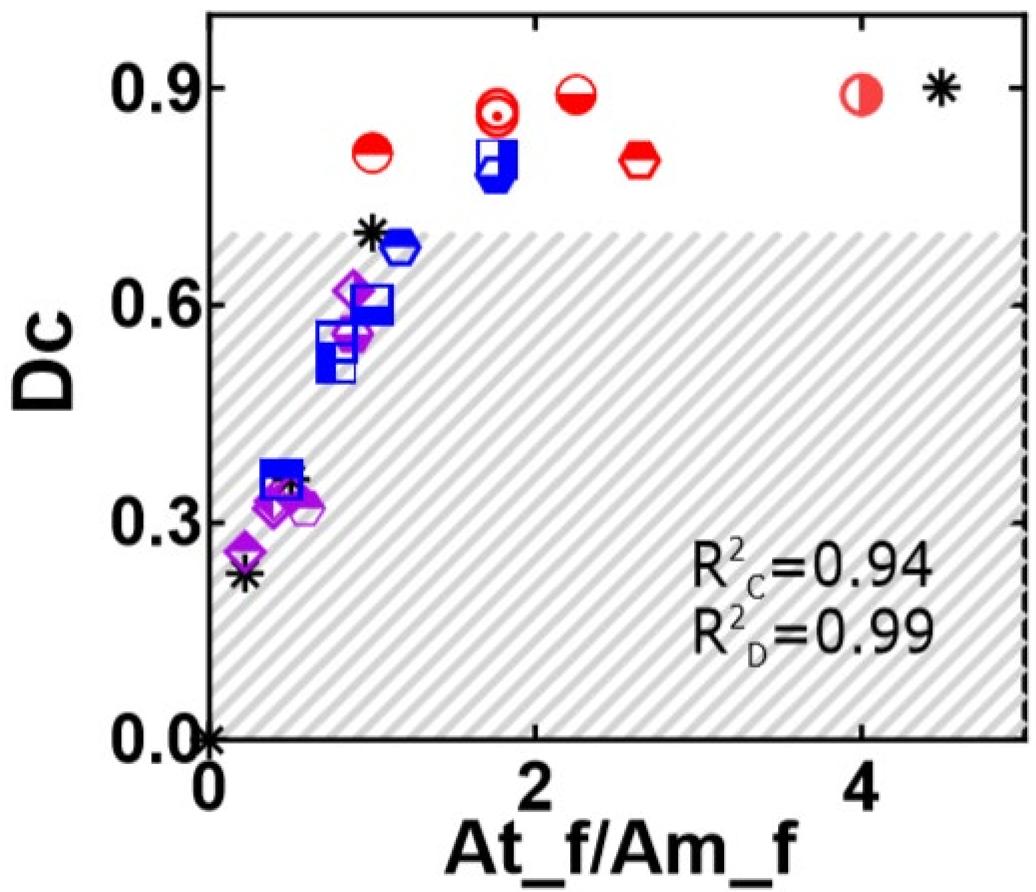

Figure 8.7: Average distance to the center vs. flowing area ratio between tracers (cylinders) and the bulk materials (sphere). Circle(red) represents 3 mm sphere, square(blue) for 4.5 mm sphere, diamond(purple) for 6.35 mm spheres, hexagons for tracer disk results and stars for sphere-sphere size segregation results. Each different fill means one-cylinder type. For disks (shown as hexagons), top filled is for #7 in table 1 and bottom filled for #8. For cylinders (shown in different shapes depends on the spheres media), #1 is top filled, #2 is bottom filled, #3 is right part filled, #4 is left part filled, #5 is an empty symbol and #6 has a dot inside the symbol

8.4 CONCLUSION

A range of experiments were carried out to study tracer cylindrical particles' segregation behavior within spheres in a quasi-two-dimension rotating tumbler. Experiments were performed for a range of rotational speeds. Three different sizes of spheres are used to mix with 30 tracer cylindrical particles. Both the impact of length and diameter of tracer cylinders were studied. The steady state situations of experiments were analyzed using image analysis software and the tracer particles' distance to the center of the tumbler is calculated.

Our results show that the common methods used to predict cylinder/disk's effective size cannot capture the whole shape segregation picture for cylinders of varying aspect ratio. They either focus on an elongated cylinder's size effect and cannot correctly predict disk's effective size or vice versa. We proposed a new area scale which takes into consideration the fact that the flowing area of a particle is the actual parameter that determines the number of contacts a particle has with its surrounding media and thus influences its segregation velocity. This method is able to correctly predict both elongated cylinder and disk's effective size when compared with our experimental results. With the correct particle effective size calculated, shape segregation can be treated as a type of size segregation, which has a more developed segregation theory, and thus segregation velocity can be calculated easily.

In this study, only cylinders inside a media of spheres are considered. Zhao et al.[107] has shown that when cylinders have different length but same diameter are mixed together, the 2-D lay down is the correct method to predict the segregation behavior. It is possible that this is caused by the fact that cylinder flow is more complex than sphere flow which is more homogeneous. Further study is needed to generate a universal rule which applies to broader types of situations.

BIBLIOGRAPHY

1. Henann, D. L. & Kamrin, K. A predictive, size-dependent continuum model for dense granular flows. *Proc. Natl. Acad. Sci. U. S. A.* **110,** 6730–5 (2013).

2. Shamlou, P. A. *Handling of bulk solids : theory and practice*. (Butterworths, 1988).

3. Hill, K. M., Khakhar, D. V, Gilchrist, J. F., McCarthy, J. J. & Ottino, J. M. Segregation-Driven Organization in Chaotic Granular Flows. *PNAS* **96,** 11701–11706 (1999).

4. Conway, S. L., Shinbrot, T. & Glasser, B. J. A Taylor vortex analogy in granular flows. *Nature* **431,** 433–437 (2004).

5. Pouliquen, O., Delour, J. & Savage, S. B. Fingering in Granular Flows. *Nature* **386,** 816–817 (1997).

6. Khakhar, D. V, Orpe, A. V & Hajra, S. K. Segregation of granular materials in rotating cylinders. *Phys. A-Statistical Mech. Its Appl.* **318,** 129–136 (2003).

7. Rasouli, M., Dubé, O., Bertrand, F. & Chaouki, J. Investigating the dynamics of cylindrical particles in a rotating drum using multiple radioactive particle tracking. *AIChE J.* **62,** 2622–2634 (2016).

8. Midi, G. D. R. On dense granular flows. *Eur. Phys. J. E. Soft Matter* **14,** 341–65 (2004).

9. Gray, J. M. N. T. & Edwards, A. N. A depth-averaged μ(I)-rheology for shallow granular free-surface flows. *J. Fluid Mech* **755,** 503–534 (2014).

10. Knight, J. B., Jaeger, H. M. & Nagel, S. R. Vibration-Induced Size Separation in Granular Media: The Convection Connection. *Phys. Rev. Lett.* **70,** 3728–3730 (1993).

11. Gray, J. & Hutter, K. Pattern formation in granular avalanches. *Contin. Mech. Thermodyn.* **9,** 341–345 (1997).

12. Samadani, A. & Kudrolli, A. Segregation Transitions in Wet Granular Matter. *Phys. Rev. Lett.* **85,** 5102–5105 (2000).

13. Zik, O., Levine, D., Lipson, S. G., Shtrikman, S. & Stavans, J. Rotationally Induced Segregation of Granular Materials. *Phys. Rev. Lett.* **73,** 644–647 (1994).

14. Hill, K. M., Caprihan, A. & Kakalios, J. Bulk segregation in rotated granular material measured by magnetic resonance imaging. *Phys. Rev. Lett.* **78,** 50–53 (1997).

15. Fan, Y. & Hill, K. M. Shear-induced segregation of particles by material density. *Phys. Rev. E* **92,** 022211 (2015).

16. Khakhar, D. V, McCarthy, J. J., Ottino, J. M. & Shinbrot, T. Transverse Flow and Mixing of Granular Materials in a Rotating Cylinder. *Phys. Fluids* **9,** 3600–3614 (1997).

17. Tripathi, A. & Khakhar, D. V. Density difference-driven segregation in a dense granular flow. *J. Fluid Mech.* **717,** 643–669 (2013).

18. Savage, S. B. & Lun, C. K. K. Particle Size Segregation in inclined chute flow of cohesionless granular solids. *J. Fluid Mech.* **189,** 311–335 (1988).

19. Dolgunin, V. Segregation modeling of particle rapid gravity flow. *Powder Technol.* **83,** 95–103 (1995).

20. Fan, Y. & Hill, K. M. Phase Transitions in Shear-Induced Segregation of Granular Materials. *Phys. Rev. Lett.* **106,** 218301 (2011).

21. Schlick, C. P., Fan, Y., Umbanhowar, P. B., Ottino, J. M. & Lueptow, R. M. Granular segregation in circular tumblers: theoretical model and scaling laws. *J. Fluid Mech.* **765,** 632–652 (2015).

22. Gray, J. M. N. T. & Ancey, C. Multi-component particle-size segregation in shallow granular avalanches. *J. Fluid Mech.* **678,** 535–588 (2011).

23. Chew, J., Parker, D. & Hrenya, C. Elutriation and species segregation characteristics of polydisperse mixtures of Group B particles in a dilute CFB riser. *AIChE J.* **59,** (2013).

24. Pereira, G. G. & Cleary, P. W. Radial segregation of multi-component granular media in a rotating tumbler. *Granul. Matter* (2013). doi:10.1007/s10035-013-0448-2

25. Remy, B., Khinast, J. G. & Glasser, B. J. Polydisperse granular flows in a bladed mixer: Experiments and simulations of cohesionless spheres. *Chem. Eng. Sci.* **66,** 1811–1824 (2011).

26. Willits, J. T., Arnarson, B. O. & Values, M. Kinetic theory of a binary mixture of nearly elastic disks. *Phys. Fluids* **11,** 3116–3122 (1999).

27. Fan, Y. & Hill, K. M. Shear-driven segregation of dense granular mixtures in a split-bottom cell. *Phys. Rev. E* **81,** 041303-- (2010).

28. Gray, J. M. N. . & Thornton, A. R. A theory for particle size segregation in shallow granular free-surface flows. *Proc. R. Soc. A Math. Phys. Eng. Sci.* **461,** 1447–1473 (2005).

29. Oda, M. A mechanical and statistical model of granular material. *Soils Found.* **14,** 13–27 (1974).

30. Hajra, S. K., Shi, D. & McCarthy, J. J. Granular mixing and segregation in zigzag chute flow. *Phys. Rev. E* **86,** 061318 (2012).

31. Jaeger, H. M. & Behringer, S. R. N. R. P. Granular Solids, Liquids and Gases. *Rev. Mod. Phys.* **68,** 1259–1273 (1996).

32. Cassar, C., Nicolas, M. & Pouliquen, O. Submarine granular flows down inclined planes. *Phys. Fluids* **17,** 103301 (2005).

33. Pouliquen, O. & Forterre, Y. A non-local rheology for dense granular flows. *Philos. Trans. A. Math. Phys. Eng. Sci.* **367,** 5091–5107 (2009).

34. Cundall, P. A. & Strack, O. D. L. A Discrete Numerical Model for Granular Assemblies. *Geotechnique* **29,** 47–65 (1979).

35. Walton, O. Application of Molecular Dynamics to Macroscopic Particles. *Int. J. Eng. Sci.* **22,** 1097–1107 (1984).

36. Thornton, C., Yin, K. K. & Adams, M. J. Numerical Simulation of the Impact Fracture and Fragmentation of Agglomerates. *J. Phys. D. Appl. Phys.* **29,** 424–435 (1996).

37. Jain, K., Shi, D. & McCarthy, J. J. Discrete Characterization of Cohesion in Gas-Solid Flows. *Powder Technol.* **146(1),** 160–167 (2004).

38. Williams, J. C. The Segregation of Powders and Granular Materials. *Fuel Soc. J.* **14,** 29–35 (1963).

39. McCarthy, J. J., Shinbrot, T., Metcalfe, G., Wolf, J. E. & Ottino, J. M. Mixing of Granular Materials in Slowly Rotated Containers. *AIChE J.* **42,** 3351–3363 (1996).

40. Chuan-yu wu, Long-yuan Li, C. T. rebound behaviour of sphere for plastic impact. *Int. J. Impact Eng.* (2003).

41. Walton, O. R. & Braun, R. L. Viscosity, Granular-Temperature, and Stress Calculations for Shearing Assemblies of Inelastic, Frictional Disks. *J. Rheol.* **30,** 949–980 (1986).

42. Walton, O. R. Numerical Simulation of Inclined Chute Flows of Monodisperse, Inelastic, Frictional Spheres. *Mech. Mat.* **16,** 239–247 (1993).

43. Thornton, C. & Yin, K. K. Impact of elastic spheres with and without adhesion. *Powder Technol.* **65,** 153–166 (1991).

44. Williams, J. The segregation of particulate materials. A review. *Powder Technol.* **15,** 245–251 (1976).

45. Li, H. & McCarthy, J. J. Cohesive particle mixing and segregation under shearLi, H., & McCarthy, J. J. (2006). Cohesive particle mixing and segregation under shear. Powder Technology, 164(1), 58–64. http://doi.org/DOI 10.1016/j.powtec.2005.12.018. *Powder Technol.* **164,** 58–64 (2006).

46. Thomas, N. Reverse and intermediate segregation of large beads in dry granular media. *Phys. Rev. E* **62,** 961–974 (2000).

47. Khakhar, D. V. Rheology and mixing of granular materials. *Macromol. Mater. Eng.* **296,** 278–289 (2011).

48. Makse, H. A. Continuous Avalanche Segregation of Granular Mixtures in Thin Rotating Drums. *Phys. Rev. Lett.* **83,** 3186–3189 (1999).

49. McCarthy, J. J. Turning the corner in segregation. *Powder Technol.* **192,** 137–142 (2009).

50. Shi, D., Abatan, A. A., Vargas, W. L. & McCarthy, J. J. Eliminating segregation in free-surface flows of particles. *Phys. Rev. Lett.* **99,** 148001 (2007).

51. Bhattacharya, T. & McCarthy, J. Chute flow as a means of segregation characterization. *Powder Technol.* **256,** 126–139 (2014).

52. Vargas, W. L., Hajra, S. K., Shi, D. & McCarthy, J. J. Suppressing the segregation of granular mixtures in rotating tumblers. *AIChE J.* **54,** 3124–3132 (2008).

53. Khakhar, D. V & Ottino, J. M. Scaling of Granular Flow Processes: from Surface Flows to Design Rules. *AIChE J.* **48(10),** 2157–2166 (2002).

54. Chou, H. Ter & Lee, C. F. Cross-sectional and axial flow characteristics of dry granular material in rotating drums. *Granul. Matter* **11,** 13–32 (2009).

55. Savage, S. B. Disorder, diffusion and structure formation in granular flow. in *Disorder and Granuar Media* (eds. Bideau, D. & Hansen, A.) 255–285 (Elsevier Science, 1993).

56. Tripathi, A. & Khakhar, D. V. Rheology of binary granular mixtures in the dense flow regime. *Phys. Fluids* **23,** (2011).

57. Orpe, A. V & Khakhar, D. V. Rheology of surface granular flows. *J. Fluid Mech.* **571,** 1–32 (2007).

58. Nase, S. T., Vargas, W. L., Abatan, A. a. & McCarthy, J. J. J. Discrete characterization tools for cohesive granular material. *Powder Technol.* **116,** 214–223 (2001).

59. Thornton, C. Coefficient of restitution for collinear collisions of elasti-perfectly plastic spheres. *J. Appl. Mech.* **64,** 383–386 (1997).

60. Thornton, C. & Ning, Z. A theoretical model for the stick/bounce behavior of adhesive, elastic-plastic spheres. *Powder Technol.* **99,** 154–162 (1998).

61. Johnson, K. L. *Contact Mechanics*. (Cambridge University Press, 1987).

62. Ottino, J. M. & Lueptow, R. M. On Mixing and Demixing. **319,** 912–913 (2008).

63. Brown, R. L. The Fundamental Principles of Segregation. *Inst. Fuel* **October,** 15–19 (1939).

64. Ottino, J. M. & Khakhar, D. V. Mixing and segregation of granular materials. *Annu. Rev. Fluid Mech.* **32,** 55–91 (2000).

65. GDR Midi. On dense granular flows. *Eur. Phys. J. E* **14,** 314–365 (2004).

66. Pouliquen, O., Jop, P. & Forterre, Y. A constitutive law for dense granular flows. *Nature* **441,** 727–730 (2006).

67. Da Cruz, F., Emam, S., Prochnow, M., Roux, J. N. & Chevoir, F. Rheophysics of dense granular materials: Discrete simulation of plane shear flows. *Phys. Rev. E - Stat. Nonlinear, Soft Matter Phys.* **72,** 1–17 (2005).

68. Henann, D. L. & Kamrin, K. A predictive, size-dependent continuum model for dense granular flows. *Proc. Natl. Acad. Sci. U. S. A.* **110,** 6730–5 (2013).

69. Hurley, R. C. & Andrade, J. E. Friction in inertial granular flows: competition between dilation and grain-scale dissipation rates. *Granul. Matter* **17,** 287–295 (2015).

70. Guillard, F., Forterre, Y. & Pouliquen, O. Scaling laws for segregation forces in dense sheared granular flows. *J. Fluid Mech* **807,** (2017).

71. Jaeger, H., Nagel, S. & Behringer, R. The Physics of Granular Materials. *Phys. Today* **49,** 32–38 (1996).

72. Bi, D., Zhang, J., Chakraborty, B. & Behringer, R. P. Jamming by shear. *Nature* **480,** 355–358 (2011).

73. Peters, I. R., Majumdar, S. & Jaeger, H. M. Direct observation of dynamic shear jamming in dense suspensions. *Nature* **532,** 214–217 (2016).

74. Louge, M., Jenkins, J., Xu, H. & Arnarson, B. Granular Segregation in Collisional Shearing Flows. *Mech. a New …* (2002).

75. Fan, Y. & Hill, K. M. Shear-induced segregation of particles by material density. *Phys. Rev. E* **92,** 022211 (2015).

76. Liu, S. & McCarthy, J. J. Transport analogy for segregation and granular rheology. *Phys. Rev. E* **96,** 020901 (2017).

77. Khola, N. & Wassgren, C. Correlations for shear-induced percolation segregation in granular shear flows. *Powder Technol.* **288,** 441–452 (2016).

78. DeGiuli, E., McElwaine, J. N. & Wyart, M. Phase diagram for inertial granular flows. *Phys. Rev. E* **94,** 012904 (2016).

79. Azéma, E. & Radjaï, F. Internal Structure of Inertial Granular Flows. *Phys. Rev. Lett.* **112,** 078001 (2014).

80. de Bruyn, J. R. & Walsh, a M. Penetration of spheres into loose granular media. *Can. J. Phys.* **82,** 439–446 (2004).

81. Jop, P., Forterre, Y. Y., Pouliquen, O., Jop, P. & Forterre, Y. Y. A constitutive law for dense granular flows. *Nature* **441,** 727–730 (2006).

82. Khakhar, D. V, McCarthy, J. J., Ottino, J. M. & Shinbrot, T. Radial segregation of granular mixtures in rotating cylinders. *Phys. Fluids* **9,** 3600–3614 (1997).

83. Xiao, H., Lueptow, R. M., Umbanhowar, P. B. & Ottino, J. M. Modeling density segregation in flowing bidisperse granular materials.

84. Nelson, M. A., Miller, R. L., Streveler, R. A., Olds, B. M. & Geist, M. R. Using concept inventories for formative assessment of conceptual learning: A case study from engineering. in *Annual Conference of the American Educational Research Association*

85. Savage, S. B. & Lun, C. K. K. Particle size segregation in inclined chute flow of dry cohesionless granular solids. *J. Fluid Mech.* **189,** 311 (1988).

86. Cooke, M. H. & Bridgwater, J. Interparticle Percolation: a Statistical Mechanical Interpretation. *Ind. Eng. Chem. Fundam* **18,** (1979).

87. Gajjar, P. & Gray, J. ~M. ~N. ~T. Asymmetric flux models for particle-size segregation in granular avalanches. *J. Fluid Mech.* **757,** 297–329 (2014).

88. Gray, J. M. N. T. & Ancey, C. Particle-size and -density segregation in granular free-surface flows. *J. Fluid Mech* **779,** 622–668 (2017).

89. Fan, Y. & Hill, K. M. Theory for shear-induced segregation of dense granular mixtures. *New J. Phys.* **13,** 095009 (2011).

90. Gray, J. M. N. T., Gajjar, P. & Kokelaar, P. Particle-size segregation in dense granular avalanches. *Comptes Rendus Phys.* **16,** 73–85 (2015).

91. May, L. B. H., Golick, L. A., Phillips, K. C., Shearer, M. & Daniels, K. E. Shear-driven size segregation of granular materials: Modeling and experiment. *Phys. Rev. E* **81,** 051301 (2010).

92. van der Vaart, K. *et al.* Underlying Asymmetry within Particle Size Segregation. *Phys. Rev. Lett.* **114,** 238001 (2015).

93. Liu, S. & McCarthy, J. J. Validating granular segregation rate models. *AIChE J.* **63,** 3756–3763 (2017).

94. Tunuguntla, D. R., Bokhove, O. & Thornton, a. R. A mixture theory for size and density segregation in shallow granular free-surface flows. *J. Fluid Mech.* **749,** 99–112 (2014).

95. Campbell, C. S. RAPID GRANULAR FLOWS. *Annu. Rev. Fluid Meeh* **22,** 57–92 (1990).

96. HUNT, M. L., ZENIT, R., CAMPBELL, C. S. & BRENNEN, C. E. Revisiting the 1954 suspension experiments of R. A. Bagnold. *J. Fluid Mech.* **452,** 1–24 (2002).

97. Campbell, C. S. Stress-controlled elastic granular shear flows. *J. Fluid Mech.* **539,** 273–297 (2005).

98. S. B. SAVAGE AND C. K. K. LUN. Particle size segregation in inclined chute flow of dry cohesionless granular solids. *J. Fluid Mech* **189,** 311–335 (1988).

99. Liu, P. Y., Yang, R. Y. & Yu, A. B. Dynamics of wet particles in rotating drums: Effect of liquid surface tension. *Phys. Fluids* **23,** 013304 (2011).

100. Shi, D. & McCarthy, J. J. Numerical simulation of liquid transfer between particles. *Powder Technol.* **184,** 64–75 (2008).

101. Figueroa, I., Li, H. & McCarthy, J. J. Predicting the impact of adhesive forces on particle mixing and segregation. *Powder Technol.* **195,** 203–212 (2009).

102. Liu, L. X., Litster, J. D., Iveson, S. M. & Ennis, B. J. Coalescence of deformable granules in wet granulation processes. *AIChE J.* **46,** 529–539 (2000).

103. Rognon, P. G., Roux, J.-N., Wolf, D., Naaïm, M. & Chevoir, F. Rheophysics of cohesive granular materials. *Europhys. Lett.* **74,** 644–650 (2006).

104. Shi, D. Advanced Simulation of Particle Processing: The Roles of Cohesion, Mass and Heat Transfer in Gas-Solid Flows. (2008).

105. Campbell, C. Granular material flows -- An overview. *Powder Technol.* **162,** 208–229 (2006).

106. Koval, G., Roux, J.-N., Corfdir, A. & Chevoir, F. Annular shear of cohesionless granular materials: From the inertial to quasistatic regime. *Phys. Rev. E* **79,** 021306 (2009).

107. Zhao, Y., Xiao, H., Umbanhowar, P. B. & Lueptow, R. M. Simulation and modeling of segregating rods in quasi-2D bounded heap flow. *AIChE J.* (2017). doi:10.1002/aic.16035

108. Cleary, P. W. The effect of particle shape on simple shear flows. *Powder Technol.* **179,** 144–163 (2008).

109. Yamane, K., Nakagawa, M., Altobelli, S. A., Tanaka, T. & Tsuji, Y. Steady particulate flows in a horizontal rotating cylinder. *http://oasc12039.247realmedia.com/RealMedia/ads/click_lx.ads/www.aip.org/pt/adcenter/pdfcover_test/L-37/522021942/x01/AIP-PT/PoF_ArticleDL_051717/PTBG_orange_1640x440.jpg/434f71374e315a556e61414141774c75?x* (1998). doi:10.1063/1.869858

110. Mandal, S. & Khakhar, D. V. An experimental study of the flow of nonspherical grains in a rotating cylinder. *AIChE J.* **63,** 4307–4315 (2017).

111. Majid Rasouli, Olivier Dube, Francois Bertrand, and J. C. Investigating the dynamics of Cylindrical Particles in a rotating drum using multiple radioactive particle tracking. *AIChE J.* (2016). doi:10.1002/aic

112. Mellmann, J. The transverse motion of solids in rotating cylinders—forms of motion and transition behavior. *Powder Technol.* **118,** 251–270 (2001).

113. Henein, H., Brimacombe, J. & Watkinson, A. Experimental study of transverse bed motion in rotary kilns. *Metall. Mater. Trans. B* **14,** 191–205 (1983).

114. Félix, G. & Thomas, N. Evidence of two effects in the size segregation process in dry granular media. *Phys. Rev. E* **70,** 051307 (2004).

115. Guo, Y. *et al.* A numerical study of granular shear flows of rod-like particles using the discrete element method. *J. Fluid Mech.* **713,** 1–26 (2012).

116. Liu, S. & Mccarthy, J. J. A Rheology Perspective of Shear Induced Size Segregation. 1–13 (2018).